Technische Universität München
TUM School of Natural Sciences

Analysis of magnetic material properties in electrical steel using neutron grating interferometry

Tobias Neuwirth

Vollständiger Abdruck der von der
TUM School of Natural Sciences der Technischen Universität München
zur Erlangung des akademischen Grades eines

Doktors der Naturwissenschaften (Dr. rer. nat.)

genehmigten Dissertation.

Vorsitz:		Prof. Dr. Michael Knap
Prüfer*innen der Dissertation:	1.	Prof. Dr. Peter Böni
	2.	Prof. Dr. Julia Herzen

Die Dissertation wurde am 05.09.2023 bei der Technischen Universität München eingereicht
und durch die TUM School of Natural Sciences am 08.12.2023 angenommen.

Abstract

In the transportation sector, battery electric vehicles (BEVs) are an option to reduce the consumption of fossil fuels, which helps to slow down climate change. The battery capacity, as well as the energy efficiency and density of electric drives are key factors impacting the driving range and therefore utility of BEVs. In this work, we focus on the efficiency of electric drives. The typically used drive types in BEVs require careful guidance of the magnetic flux.

Conventionally, cutouts in the electrical steel comprising the magnetic core of the drive guide the magnetic flux. As part of an interdisciplinary project, we studied the replacement of cutouts with embossed areas. The embossing introduces residual stress, which locally reduces the magnetic permeability and guides the flux while maintaining mechanical strength. By optimizing the embossing parameters, the achievable rotational speed of the electric drive increases and the stray fields are reduced, subsequently increasing efficiency.

Neutron grating interferometry (nGI) is a unique technique able study the local magnetic properties by visualizing magnetic flux distribution in electrical steel. Knowledge about the flux distribution is required for optimizing the embossing parameters.

With nGI, we proved that residual stress generates magnetic barriers, able to guide the magnetic flux. The embossing parameters chosen significantly influence the resulting barrier. A sequence of small embossing points shows the best compromise between guidance of the magnetic flux and deformation of the electrical steel.

Further, we mapped the orientation and size of magnetic domains for the first time using nGI employing different models. In addition, we analyzed the local magnetic hysteresis dependent on residual stress. We found that the connection to standard hysteresis measurements is not trivial.

For the successful study of the effects of residual stress, signal variations close to the noise limit need to be resolved. Hence, part of this work focuses on improving nGI and understanding noise inherent in nGI measurements. As a result, we have developed an nGI-setup with a significant performance increase. We further analyzed the dynamic range of the scattering signal accessible by nGI depending on the available neutron flux and the performance of the nGI-setup.

Kurzfassung

Im Verkehrssektor sind elektrische Fahrzeuge ein Mittel um den Verbrauch fossiler Energie zu senken und dadurch den Klimawandel zu verlangsamen. Neben der Batteriekapazität, wird die Reichweite und dadurch die Alltagstauglichkeit von elektrischen Fahrzeugen durch die Effizienz und die Energiedichte der Elektromotoren maßgeblich bestimmt. Diese Arbeit beschäftigt sich dabei mit der Effizienz von Elektromotoren. Die üblicherweise in elektrischen Fahrzeugen genutzten Motortypen benötigen eine Lenkung des magnetischen Flusses.
Die Flusslenkung wird derzeit durch Ausschnitte in den Elektroblechen, welche den magnetischen Kern des Motors bilden, bewerkstelligt. Im Rahmen eines interdisziplinären Projekts wurde das Ersetzen der Ausschnitte durch geprägte Bereiche untersucht. Durch Prägen werden Eigenspannungen erzeugt, welche lokal die magnetische Permeabilität senken und den magnetischen Fluss lenken ohne die mechanische Festigkeit zu beeinträchtigen. Durch Optimierung der Prägeparameter kann die Rotationsgeschwindigkeit des Motors gesteigert und können Streufelder unterdrückt werden, was die Effizienz erhöht.
Neutronengitterinterferometrie (nGI) ist eine einzigartige Messtechnik um die lokalen magnetischen Eigenschaften zu untersuchen, indem die Verteilung des magnetischen Flusses im Elektroblech sichtbar gemacht wird. Die Verteilung des Flusses wird benötigt um die Prägeparameter zu optimieren.
Mit nGI wurde gezeigt, dass Eigenspannungen magnetische Barrieren zur Flusslenkung im Elektroblech erzeugen. Abhängig von der eingebrachten Prägung ändert sich die magnetische Flusslenkung. Besonders die Anordnung von mehreren kleinen Prägepunkten zeigt im Hinblick auf Flusslenkung und geringer Verformung die besten Ergebnisse. Zusätzlich konnte erstmalig ortsaufgelöst die Größe und Orientierung von magnetischen Domänen im Volumen eines Elektroblechs sichtbar gemacht und mit verschiedenen Modellen analysiert werden. Weiterhin wurde auch die lokale magnetische Hysterese im Elektroblech abhängig des eingebrachten Eigenspannungszustandes untersucht. Die Verknüpfung der lokalen Hysterese mit der globalen ist nicht trivial.
Zur Untersuchung dieser Effekte, müssen Signalvariationen nah am Signalrauschen gemessen werden. Daher beschäftigt sich ein Teil der Dissertation mit der Verbesserung des nGI-Aufbaus und dem Verständnis des Rauschens während der Messung. Im Zuge dessen wurde ein stark optimierter nGI-Aufbau gebaut. Zusätzlich wurde der dynamische Bereich des mit nGI gemessenen Streusignals in Abhängigkeit von Neutronenfluss und Leistungsfähigkeit des nGI-Aufbaus untersucht.

Contents

List of Abbreviations

BEV	battery electric vehicle
CCD	charge-coupled device
CMOS	complementary metal-oxide-semiconductor
cTL	conventional Talbot-Lau
DC	duty cycle
DFI	dark-field image
DPCI	differential phase contrast image
FOV	Field of View
FWHM	full width at half maximum
GOES	grain-oriented electrical steel
Micro	Micromagnetic
MLZ	Heinz Maier-Leibnitz Zentrum
nGI	neutron grating interferometry
NGOES	non-grain-oriented electrical steel
NVS	neutron velocity selector
OB	open beam
PMSM	permanent magnet synchronous machine
PSI	Paul Scherrer Institut
RD	rolling direction
ROMD	random oriented magnetic domain
SANS	small-angle neutron scattering
SDD	sample-to-detector-distance
SG	Single Grating
sTL	symmetric Talbot Lau
SynRM	synchronous reluctance machine
TI	transmission image
TLI	Talbot-Lau interferometer
USANS	ultra-small-angle neutron scattering

Abbreviations used in this thesis.

1 Investigation of non-grain-oriented electrical steel using neutrons

Climate change necessitates a reduction in the consumption of fossil energy. Hence, energy efficiency has become a major topic of research. In particular, transportation accounts for a large part of consumed fossil energy. Hence alternative means of transport, such as battery electric vehicles (BEVs), are being investigated. In addition to the battery, the energy efficiency and density of electric drives are important factors affecting the operating distance. Increasing the rotational speed of an electric drive causes its energy density to rise. Typical electric drive topologies used in battery electric vehicles are synchronous reluctance machines (SynRM) and permanent magnet synchronous machines (PMSM) [1]. For an optimal operation, these topologies require the guidance of the magnetic flux inside the rotating magnetic core, reduction of stray fluxes, or production of a targeted magnetic anisotropy [2]. A stack of non-grain-oriented electrical steel (NGOES) sheets with a sub-millimeter thickness typically comprises the magnetic core.

Conventionally, cutting out magnetic core material generates the required magnetic flux barriers. The significantly reduced relative magnetic permeability in air ($\mu_\mathrm{r} = 1$) compared to NGOES (μr $\approx$ 10000) [3] acts as the flux barrier, guiding the magnetic flux and suppressing stray flux. The remaining filigree structure of the rotor must carry the centrifugal forces and torques acting during the operation. Therefore, the magnetic optimization of the magentic core limits the maximum rotational speed of an electric drive. In SynRM [4] and PMSM [5], a compromise between the magnetic optimization and the achievable rotational speed due to acting forces has to be achieved. Further optimizations require an alternative to conventional magnetic core topologies.

Normally residual stress in the magnetic core is avoided due to the negative effect on the magnetic properties, primarily the magnetic permeability [6] [7], which causes additional energy loss. This effect is called the Villari effect or inverse magnetostriction. In contrast, as an alternative approach to cutouts in the magnetic core, we have investigated the targeted introduction of residual stress into the electrical steel to reduce the magnetic permeability locally. We locally deformed the electrical steel by embossing the material to introduce the residual stress. A specific residual stress state is created depending on the size and number of embossing points. The residual stress locally decreases the magnetic permeability enabling the guidance of the magnetic flux similar to cutouts. As a result of the added material cross-section, the mechanical strength of the rotor increases and enables the possibility of higher angular velocity.

However, qualifying the local change in magnetic properties in the bulk of the material is challenging. Standard techniques either probe global magnetic properties in the bulk or local surface properties of a sample [8].
Two examples of standardized global measurements of magnetic properties in electrical steel are an Epstein frame and a single-sheet-tester. Here the global bulk magnetic permeability dependent on the magnetic polarization, the magnetic hysteresis, and the power loss during remagnetization can be quantitatively evaluated. However, in the case of localized influences, only an averaged signal is recorded.
In contrast, most microscopic methods only allow tracking of the surface domain structure. A more detailed overview of possible methods is given in, e.g., [8]. In this thesis, we will discuss only some examples. One of the oldest evaluation methods is the Bitter method [9], where ferrofluid deposited on the sample surface arranges according to the underlying magnetic domains. Another technique is magneto-optical Kerr microscopy (MOKE). Here the polarization change in polarized light during interaction with the magnetic domains [10] is used to track the domain structure and the magnetization vector. The internal bulk domain structure can be inferred using the observed surface domains and the domain theory of magnetism. However, a prerequisite for this technique is a homogeneous, non-deformed sample.
Hence, an analysis of the surface domains only allows to gather little to no information about the bulk domain structure. Similarly, a pure global analysis of the magnetic parameters blurs the influence of embossing on the magnetic properties.
Neutron grating interferometry (nGI) is a powerful tool to evaluate the local magnetic properties of a sample in its bulk. nGI is an advanced neutron imaging method adding phase and scattering (dark field) contrast to the standard attenuation contrast used in neutron imaging. The phase contrast tracks the phase shift of the neutrons passing through the sample. However, the limited difference in the index of refraction for neutrons reduces the usefulness of this contrast mechanism.
The main benefit of nGI is its ability to detect the scattering of neutrons in the ultra-small-angle scattering regime (USANS) off structures on a micrometer-length scale caused by nuclear or magnetic scattering length density variations. In the context of this thesis, we track the scattering of neutrons on magnetic domains in the USANS regime and evaluate the size of the scattering centers. Other exemplary applications of nGI are the evaluation of vortex lattice domains in superconductors [11] or analysis of defects in additively manufactured components, e.g., [12, 13]. We will outline the theory underlying the nGI signal measured on NGOES and discuss and demonstrate which physical parameters can be accessed using nGI as an evaluation technique.
Construction of new electric drive topologies using residual stress to guide magnetic flux requires a good understanding of the connection between residual stress and guidance of the magnetic flux in NGOES. Here the knowledege about local change of

physical parameters due to residual stress is critical to be able to model and optimize new drive topologies towards higher efficiency and power density.

Outline of this thesis

The thesis is structured as follows: In Chap. 2 we will review the basic principles of the energy in a ferromagnet. We will focus primarily on the micromagnetic description, which we will later use to calculate the scattering cross section for neutrons. Further, we will briefly review nuclear and magnetic scattering under small angles and the resulting correlation functions.
Chap. 3 will discuss the theoretical and practical foundations of nGI. We will focus on the scattering contrast and the principles of quantitative and anisotropic measurements. Furthermore, we will discuss limitations inherent to nGI, which one has to consider during measurement and evaluation.
In Chap. 4 we discuss the details and characteristics of the experimental setups used in this thesis. The main focus here is the improved high visibility neutron grating interferometer developed as an integral part of this thesis for the ANTARES beamline at the Heinz Maier-Leibnitz Zentrum (MLZ). Further, we present the sample composition and preparation. The experimental results of this thesis and the implication of the evaluation are presented in Chap. 5. In Sec. 5.1, we discuss the information contained in the DFI signal and the origin of the change in the DFI signal due to deformation. Sec. 5.2 analyzes different embossing strategies concerning their ability to guide magnetic flux in electrical steel.
Sec. 5.3 discusses the connection between the scattering contrast and local magnetic properties in NGOES. For this purpose, we evaluate the change of the dark field signal dependent on the correlation length and recover the mean domain size. These results are then compared to embossed NGOES to show the influence of residual stress on the domain size. These results demonstrate the ability of nGI to recover information about the magnetic domains in the bulk of ferromagnetic samples. Sec. 5.4 considers the anisotropy of the magnetic scattering caused by a preferred orientation and shape of the magnetic domains. Those two sections together show exemplary measurements, which greatly impact future investigation of the magnetic properties in NGOES.
Sec. 5.5 analyzes the local hysteretic behavior of embossed NGOES compared to virgin NGOES. Here, we evaluate the remanence and coercivity of the material dependent on the residual stress state. We demonstrate the importance of spatially resolved measurements for partially embossed samples, as the recorded remanence and coercivity depend on both the embossing state at the probed area and the embossing state surrounding the probed area.

2 Theory

In this part of the thesis, we will discuss the necessary equations and concepts for understanding the acquired neutron grating interferometry data. Neutron grating interferometry identifies the magnetic domain structure that causes scattering off neutrons under ultra-small angles (USANS). In Sec. 2.1, the basic principles of micromagnetics used to describe the distribution of magnetic domains and the resulting model for neutron scattering are described. In section 2.2, we discuss the principles covering the interaction of neutrons with matter.

2.1. Ferromagnetism

In magnetically ordered materials, the elementary magnetic moments interact with each other. This interaction leads in ferromagnetic materials, for neighboring magnetic spins, to a parallel orientation of the magnetic moments and causes a spontaneous saturation magnetization M_s. Globally, ferromagnets are composed of magnetic domains, small volumes in which the magnetization direction is parallel. Due to the minimization of total energy in a material, the magnetization direction of different domains is not necessarily parallel. As a result, the global magnetization M of a ferromagnet is typically much smaller than M_s, as the magnetization directions of different domains compensate each other and reduce stray magnetic fields. From this short introduction to ferromagnets, it is clear that their magnetic properties must be analyzed on a wide range of length scales. These length scales range from describing elementary magnetic moments on the atomic scale to the average magnetization of a bulk magnetic sample (mm scale). As such, a general description of the global magnetic properties based on the elementary magnetic moments using modern computer systems is not feasible [8]. In this section, we consider primarily the length scales from 100 nm to 20 µm, as this is the range accessed by neutron grating interferometry, the primary experimental technique used in this thesis. According to [8], this length scale is in the transition regime between micromagnetics, which describes the internal structure of domain walls, and magnetic domain theory, governing the distribution of magnetic domains. In the following, we will discuss the basics of both theoretical principles to understand the acquired data. Here we summarize the descriptions presented in [8], [14], and [15], a more in-depth derivation may be accessed there.

2.1.1. Energy due to magnetic interactions in a ferromagnet

It is important to note that micromagnetics and domain theory are based on the same variational principle derived from thermodynamics, in [16, 17]. It describes the (reduced) magnetization vector $\mathbf{m}(\mathbf{r}) = \mathbf{M}(\mathbf{r})/M_\mathrm{s}$ of a ferromagnet depending on its magnetic material parameters, the geometry, and external influences, i.e., applied magnetic field or applied strain. $\mathbf{m}(\mathbf{r})$ is chosen such that the total magnetic energy reaches an absolute or local minimum under the condition $\mathbf{m}^2 = 1$. Following as a consequence of the minimum energy principle, the torque on the magnetization has to vanish. The torque is calculated from the variational principle. The total energy in a ferromagnet is given as [8]:

$$E_\mathrm{tot} = E_\mathrm{x} + E_\mathrm{an} + E_\mathrm{z} + E_\mathrm{st} + E_\mathrm{me} \ . \tag{2.1}$$

E_tot consists of five energy contributions: the exchange interaction energy E_x, the anisotropy energy E_an, the Zeeman energy E_z, the stray field energy E_st and the magnetoelastic energy E_me.
The energy E_x describes the preference for parallel alignment of neighboring elementary magnetic moments in a ferromagnet. Accordingly, variations in $\mathbf{M}$ cause an energy penalty, described by the following expression [16]:

$$E_\mathrm{x} = A \int_V (\nabla \mathbf{m})^2 \, \mathrm{d}V \ , \tag{2.2}$$

where A is the exchange stiffness constant and V is the sample volume. For a cubic or isotropic material, A is a scalar, while hexagonal or other lower symmetry crystals require A to be a vector. Typical values for A are in the order of $10\,\mathrm{pJ\,m^{-1}}$ [18]. Also, Eq. 2.2 can be rewritten to [16, 19]:

$$E_\mathrm{x} = A \int_V \left((\nabla m_1)^2 + (\nabla m_2)^2 + (\nabla m_3)^2 \right) \mathrm{d}V \ , \tag{2.3}$$

where m_i denotes the orthogonal components of $\mathbf{m}$. Eqs. 2.2 and 2.3 are derived from the isotropic Heisenberg interaction $s_1 \cdot s_2$ between neighboring magnetic spins s_i, considering only nearest neighbor interactions [8]. A full derivation may be found in, e.g., [20].
The magnetic anisotropy energy of a ferromagnet depends on the orientation mismatch between the direction of magnetization $\mathbf{M}$ and the crystal axes. The (magnetocrystalline) anisotropy energy E_an describes the underlying spin-orbit interactions. While

magneto dipolar interaction may also contribute to E_{an} [21, 22], its influence is generally small and vanishes for ideal cubic and hexagonal lattices [20]. For a cubic crystal $E_{\mathrm{an}}^{\mathrm{c}}$ may be expressed by [8]:

$$E_{\mathrm{an}}^{\mathrm{c}} = K_{\mathrm{c1}}\left(m_1^2 m_2^2 + m_1^2 m_3^2 + m_2^2 m_3^2\right) + K_{\mathrm{c2}} m_1^2 m_2^2 m_3^2 \ . \tag{2.4}$$

Here m_i denotes the components of the magnetization vector along the cubic axes. K_{c1} and K_{c2} are material constants. K_{c2} and other higher order terms can usually be neglected [8]. The value K_{c1} is in the range $\pm 10^4\,\mathrm{J\,m^{-3}}$, while its sign determines the easy axes for magnetization, either $\langle 100\rangle$ or $\langle 111\rangle$. The easy axes are the crystallographic directions favored by the $\mathbf{M}$ orientation.
The Zeeman energy E_{z} is the energy due to interaction with an external magnetic field $\mathbf{H}_{\mathrm{ext}}$. E_{z} is defined as:

$$E_{\mathrm{z}} = -\mu_0 \int_V \mathbf{M}\cdot\mathbf{H}_{\mathrm{ext}}\mathrm{d}V \ , \tag{2.5}$$

with $\mu_0 = 4\pi\cdot 10^{-7}\,\mathrm{N\,A^{-2}}$ being the vacuum permeability. $\mathbf{H}_{\mathrm{ext}}$ causes a torque on the magnetization direction and tries to align it along its direction.
The stray field energy is connected to the demagnetizing stray field $\mathbf{H}_{\mathrm{d}}$ generated by the magnetization $\mathbf{M}$:

$$E_{\mathrm{st}} = -\frac{1}{2}\int_V \mathbf{H}_{\mathrm{d}}\cdot\mathbf{M}\mathrm{d}V \tag{2.6}$$

The stray field $\mathbf{H}_{\mathrm{d}}$ can be derived from magnetostatics using potential theory [8]. Here we introduce the volume charge density λ_{V} and the surface charge density σ_{S}:

$$\lambda_{\mathrm{V}} = -\nabla\cdot\mathbf{m}, \quad \sigma_{\mathrm{s}} = \mathbf{m}\cdot\mathbf{n} \ , \tag{2.7}$$

with $\mathbf{n}$ as the outward directed surface normal. Using these quantities, we can determine the potential of the stray field $U_{\mathrm{d}}(\mathbf{r})$ by integration over $\mathbf{r}'$:

$$U_{\mathrm{d}}(\mathbf{r}) = \frac{M_{\mathrm{s}}}{4\pi\mu_0}\left[\int \frac{\lambda_{\mathrm{V}}(\mathbf{r}')}{|\mathbf{r}-\mathbf{r}'|}\mathrm{d}V' + \frac{\sigma_{\mathrm{S}}(\mathbf{r}')}{|\mathbf{r}-\mathbf{r}'|}\mathrm{d}S'\right] \ . \tag{2.8}$$

The stray field $\mathbf{H}_{\mathrm{d}}$ is then given by:

$$\mathbf{H}_{\mathrm{d}} = -\nabla U_{\mathrm{d}}(\mathbf{r}) \ . \tag{2.9}$$

The integrations $\int \mathrm{d}V'$ and $\int \mathrm{d}S'$ extend over the volume and surface of the sample, respectively. $\mathbf{H}_\mathrm{d}$ is caused by inhomogeneities in $\mathbf{M}$. E_st penalizes magnetic volume (λ_V) or surface (σ_S) charges.
The last contribution in Eq. 2.1 is the magnetoelastic energy E_me. This contribution results from the magnetostriction effect [23], where the magnetization of a stress-free sample causes a change in dimensions. From a purely phenomenological point of view E_me is given by [14]:

$$E_\mathrm{me} = \int_V e_\mathrm{me} \mathrm{d}V \ , \tag{2.10}$$

where e_me denotes the magnetoelastic energy density. The general calculation of e_me in deformable ferromagnets is a complex task, as all previously considered components of the total energy of a ferromagnet depend on the lattice distortions and hence contribute to the magnetoelastic energy [8]. The magnetocrystalline anisotropy causes the most important contribution. This contribution causes i) the sensitivity of magnetic materials to stress and ii) an additional volume energy term to magnetization configurations not consisting of solely anti-parallel domains. An in-depth analysis of calculation methods for the magnetoelastic contribution can be found in, e.g., [8] and [23]. In case of cubic crystals the magnetoelastic energy density e^c_me can be expressed as [18]:

$$e^\mathrm{c}_\mathrm{me} = -\frac{3}{2}\lambda_{100} \sum_{i=1}^{3} \sigma_\mathrm{ii} m_\mathrm{i}^2 - \frac{3}{2}\lambda_{111} \sum_{i \neq j} \sigma_\mathrm{ij} m_\mathrm{i} m_\mathrm{j} \ . \tag{2.11}$$

Here λ_{100} and λ_{111} are the saturation magnetostriction constants along the subscripted crystallographic axis, m_i denote the Cartesian components of the magnetization vectors, and σ is the stress tensor caused by defects or external stresses. The values for λ range from 10^{-3} to 10^{-6} [14].

2.1.2. Balance of torque

The total magnetic energy in a ferromagnet can be considered as a functional of its magnetization state,

$$E_\mathrm{tot} = E_\mathrm{tot}(\mathbf{M}(\mathbf{r})) \ . \tag{2.12}$$

For an equilibrium magnetization, a (local) minimum has to be reached, hence variations of E_{tot} have to vanish:

$$\delta E_{\text{tot}} = \delta(E_{\text{x}} + E_{\text{an}} + E_{\text{z}} + E_{\text{st}} + E_{\text{me}}) = 0 \tag{2.13}$$

Here the variational calculus leads to nonlinear partial integrodifferential equations in the bulk magnetization and complex boundary conditions for surface magnetization [18, 23]. As our interest is in the magnetic microstructure of bulk magnetic samples, we restrict the equations to the bulk equilibrium conditions. In static equilibrium, the torque on the magnetization vector $\mathbf{M}(\mathbf{r})$ due to an effective magnetic field $\mathbf{H}_{\text{eff}}(\mathbf{r})$ vanishes inside the material [18, 23].

$$\mathbf{M}(\mathbf{r}) \times \mathbf{H}_{\text{eff}}(\mathbf{r}) = 0 \tag{2.14}$$

The effective magnetic field $\mathbf{H}_{\text{eff}}(\mathbf{r})$ consists of the applied magnetic field $\mathbf{H}_0$ (connected to E_{z}), the stray field $\mathbf{H}_d(\mathbf{r})$ (connected to E_{st}), the magnetic anisotropy field $\mathbf{H}_p(\mathbf{r})$ (connected to both E_{an} and E_{me} and the exchange field $\mathbf{H}_{\text{ex}}$ (connected to E_{x}) [14]:

$$\mathbf{H}_{\text{eff}}(\mathbf{r}) = \mathbf{H}_0 + \mathbf{H}_d(\mathbf{r}) + \mathbf{H}_p(\mathbf{r}) + \mathbf{H}_{\text{ex}} \tag{2.15}$$

Here we assume that the external field is uniformly applied. Furthermore, as briefly discussed in Sec. 2.1.1, the magnetoelastic and magnetocrystalline energy contributions are deeply connected. Hence they are combined in the magnetic anisotropy field. The exchange field is defined as [19]:

$$\mathbf{H}_{\text{ex}} \frac{2A}{\mu_0 M_{\text{s}}^2} \nabla^2 \mathbf{M} = l_{\text{M}}^2 \mathbf{M} \ , \tag{2.16}$$

where l_{M} is the micromagnetic length scale for magnetostatic interaction and ∇^2 the Laplace operator of a vector field $\mathbf{f}$ given by $\nabla^2 \mathbf{f} = \{\nabla^2 f_x, \nabla^2 f_y, \nabla^2 f_z\}$. For the following derivations, we assume that the applied magnetic field $\mathbf{H}_0$ is parallel to $\mathbf{e}_x$ and the material is close to saturation. We can express the magnetization as follows:

$$\mathbf{M}(\mathbf{r}) = \{M_x(\mathbf{r}) \approx M_s, M_y(\mathbf{r}) \ll M_s, M_z(\mathbf{r}) \ll M_s, \} \tag{2.17}$$

We assume that the local magnetization in the material is a function of $\mathbf{r}$ [24, 25]:

$$M_s(\mathbf{r}) = M_s(1 + l_m(\mathbf{r})) \ . \tag{2.18}$$

Here, I_m is an inhomogeneity term with a small magnitude describing the local variation of M_s. The term is chosen so that the average I_m over the sample volume vanishes. For further derivations, we will work in the Fourier space. Hence we define the Fourier transform $\widetilde{F}(\mathbf{q})$ of a continuous function $F(\mathbf{r})$:

$$\widetilde{F}(\mathbf{q}) = \frac{1}{(2\pi)^{3/2}} \int_V F(\mathbf{r}) \exp(-i\mathbf{q}\mathbf{r}) \mathrm{d}V \ . \tag{2.19}$$

Here $\mathbf{q}$ denotes the wavevector. We can now write for the Fourier transformed magnetization $\widetilde{\mathbf{M}}(\mathbf{q})$:

$$\widetilde{\mathbf{M}}(\mathbf{q}) = \{M_s(\delta(\mathbf{q}) + \widetilde{I}_m(\mathbf{q})), \widetilde{M}_y(\mathbf{q}), \widetilde{M}_z(\mathbf{q})\} \tag{2.20}$$

In this thesis, we only consider first-order contributions of I_m. A derivation including second-order contributions can be found in Ref. [25]. We can rewrite the magnetic fields from the balance of torque equation into their Fourier transforms. For the exchange field the Fourier transform $\widetilde{\mathbf{H}}_{\mathrm{ex}}$ is:

$$\widetilde{\mathbf{H}}_{\mathrm{ex}}(\mathbf{q}) = -l_m^2 q^2 \{M_s \widetilde{I}_m, \widetilde{M}_y, \widetilde{M}_z\} \tag{2.21}$$

For the stray field the Fourier transform $\widetilde{\mathbf{H}}_d(\mathbf{q})$ is given by [14, 25]:

$$\widetilde{\mathbf{H}}_d(\mathbf{q}) = H_i \delta(\mathbf{q}) \mathbf{e}_x - \frac{\mathbf{q} \cdot (\mathbf{q} \cdot \widetilde{\mathbf{M}}(\mathbf{q}))}{q^2} \tag{2.22}$$

Here we assume a sample near saturation magnetization with an ellipsoidal shape and $\mathbf{H}_0$ directed along a principle axis of the ellipsoid. Under this assumption, we can write the internal magnetic field $H_i = H_0 - N_d M_s$, where N_d denotes the demagnetization factor. In the first order approximation of I_m, the x-component of the magnetic anisotropy field $\mathbf{H}_p(\mathbf{r})$ causes no torque on the magnetization vector [25]. Hence the Fourier transform of $\mathbf{H}_p(\mathbf{r})$ can be written as:

$$\widetilde{\mathbf{H}}_p(\mathbf{q}) = \{0, \widetilde{H}_{p,y}(\mathbf{q}), \widetilde{H}_{p,z}(\mathbf{q})\} \tag{2.23}$$

$\mathbf{H}_p(\mathbf{r})$ contains information about crystallite size, inhomogeneity of the lattice strain, and crystallographic texture [26]. The source of the magnetic anisotropy (magnetocrystalline or magnetoelastic) is not differentiated. As a result of the condition $|\mathbf{M}| = M_S$, $\mathbf{H}_p(\mathbf{r})$ has only two independent components. Using the balance of torque

equation (Eq. 2.14) and Eqs. 2.21, 2.22 and 2.23 we can solve for the magnetization components $\widetilde{M}_y$ and $\widetilde{M}_z$ [15, 27]:

$$\widetilde{M}_y = \frac{p\left(\widetilde{H}_{p,y}\left[1 + p\frac{q_z^2}{q^2}\right] - M_s\widetilde{I}_m\frac{q_y q_x}{q^2} - \widetilde{H}_{p,z}\frac{q_z q_y}{q^2}\right)}{1 + p\frac{q_z^2+q_y^2}{q^2}} \tag{2.24}$$

and

$$\widetilde{M}_z = \frac{p\left(\widetilde{H}_{p,z}\left[1 + p\frac{q_y^2}{q^2}\right] - M_s\widetilde{I}_m\frac{q_z q_y}{q^2} - \widetilde{H}_{p,y}\frac{q_z q_y}{q^2}\right)}{1 + p\frac{q_z^2+q_y^2}{q^2}} \ . \tag{2.25}$$

Here we introduced the dimensionless function p:

$$p(q,H_\mathrm{i}) = \frac{M_S}{H_\mathrm{eff}(q,H_\mathrm{i})} \ , \tag{2.26}$$

which depends on the effective magnetic field H_eff:

$$H_\mathrm{eff} = (1 + l_\mathrm{H}^2 q^2)H_\mathrm{i} \ . \tag{2.27}$$

Please note that this H_eff is not equal to the one used in Eq. 2.14. The value l_H denotes the micromagnetic exchange length of the magnetic field, describing the size of inhomogeneously magnetized areas around lattice defects.

2.2. Neutron scattering

In the following section, the theoretical description of neutron scattering under (ultra)-small-angles ((U)SANS) is discussed. We focus on the concepts and equations necessary to understand the results presented in this thesis and omit a complete derivation from the first principles for brevity. A basic introduction to neutron scattering may be found in, e.g., Sivia [28], while an in-depth derivation is provided by, e.g., Squires [29].
The standard introduction to nuclear neutron scattering is to consider the interaction between single scattering centers and neutrons. As neutrons interact via the strong force, such a scattering center is an atomic nucleus. The bound coherent scattering length b_c describes the scattering probability. The specific isotope and the spin of the neutron define this parameter. Considering the standard case of scattering thermal or

cold neutrons [1] off the atomic crystal lattice, the scattering can be simplified to be isotropic and point-like. In this case, the neutron wavelength λ_N, which is typically in the Ångstrom range, is much larger than the interaction range of the nuclei ($\approx 10^{-4}$ Å). In most scattering experiments, λ_N is in the same order of magnitude as the lattice spacing. Like electromagnetic waves, this leads to the well-known interference effects used in diffraction experiments. As the neutron has a magnetic moment μ_n, it also interacts with the magnetization field **M(r)** generated by the nucleus and the electron shell. The interaction range of the magnetization field is long compared to nuclear interaction. Hence the magnetic interaction cannot be assumed to be point-like and isotropic.
The NGOES samples probed in this thesis typically have a grain diameter around 80 µm [30], with a diameter of the magnetic domains around 3 µm. These length scales show scattering in the (U)SANS regime, which will be the focus of the two following sections. First, we will discuss the case for nuclear scattering under small angles, where we will use the well-understood example of monodisperse spherical particles. Afterward, we will discuss scattering caused by spin-misalignment.

2.2.1. Nuclear neutron scattering under small angles

For the length scales in the micrometer range ($\approx$ size of the magnetic domains) considered in this thesis, the nuclear and magnetic properties relevant for scattering are described by a continuous scattering length density per unit volume $\rho(r)$ as the atomic positions are not relevant anymore. Typically such a description is valid for nano- and microparticles and, in some cases, for superconducting vortex matter and magnetic domains.
As such, we can write the differential scattering cross-section as follows:

$$\frac{d\sigma\,(\boldsymbol{q})}{d\Omega} = \int_V \left[\int_V \rho(\boldsymbol{R})^* \rho(\boldsymbol{R}+\boldsymbol{r}) d\boldsymbol{R} \right] \exp\left(-\mathrm{i}\boldsymbol{q}\cdot\boldsymbol{r}\right) d\boldsymbol{r} \ . \tag{2.28}$$

The * denotes the complex conjugate, as the definition includes the option of ρ being a complex number. This definition of the scattering cross-section assumes the scatterer to be in a vacuum, i.e., surrounded by a scattering length density of zero. In most cases, this assumption is incorrect, and a material with a non-zero scattering length density surrounds the scatterer. Typical cases for such systems are colloids. In such

1 It should be noted that the transition between thermal and cold neutrons is gradual. There is no strictly defined cut-off wavelength [29].

cases the contrast of the scattering length density $\Delta\rho(\boldsymbol{r})$ is used to describe the scattering at a given position $\boldsymbol{r}$:

$$\Delta\rho(\boldsymbol{r}) = \rho(\boldsymbol{r}) - \overline{\rho} \tag{2.29}$$

Here $\overline{\rho}$ is the mean value of $\rho(\mathbf{r})$ in the interaction volume of the scattered neutron. Using this definition in Eq. 2.28, we can define the differential scattering cross-section for the scattering length density contrast:

$$\frac{d\sigma(\boldsymbol{q})}{d\Omega} = \int_V \left[\int_V \Delta\rho(\boldsymbol{R})^* \Delta\rho(\boldsymbol{R}+\boldsymbol{r}) d\boldsymbol{R} \right] \exp(-i\boldsymbol{q}\cdot\boldsymbol{r})\, d\boldsymbol{r} \tag{2.30}$$

$$= \int_V \gamma(\boldsymbol{r}) \exp(-i\boldsymbol{q}\cdot\boldsymbol{r})\, d\boldsymbol{r}\ . \tag{2.31}$$

The inner integral denotes the autocorrelation function ($\gamma(\boldsymbol{r})$). We can describe the autocorrelation function geometrically as the overlap of a scatterer with a copy of itself shifted by the vector $\boldsymbol{r}$. Fig. 2.1 a) provides a visual example of the autocorrelation function of an individual spherical particle. Due to its definition, the maximum of the autocorrelation function is at $r = 0$, and its value decreases to zero when r is larger than the particle diameter. In the (U)SANS regime, we can neglect the momentum

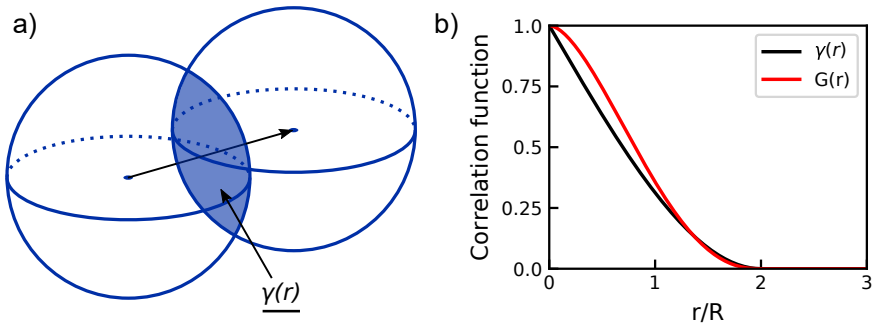

Figure 2.1.: a) Spherical particles as an example of the correlation function γ. The overlap of the particle with itself, displaced by a vector $\boldsymbol{r}$, defines $\gamma(\boldsymbol{r})$. b) Result of $\gamma(\boldsymbol{r})$ and $G(\boldsymbol{r})$, corresponding to the sketch in a).

transfer in the direction of the neutron beam ($z-$axis) q_z. Hence, we can restrict the scattering to $q_z = 0$, which does not allow to gather structural information parallel to the beam direction. To account for this, a second correlation function G is defined:

$$G(x,y) = \int \gamma(x,y,z)dz = \int \frac{d\sigma(\boldsymbol{q})}{d\Omega}(q_x,q_y,0) \exp(i(q_x x + q_y y))\, dq_x dq_y \tag{2.32}$$

We only acquire the scattering intensity in an experiment, not the complex scattering amplitude. This lack of information prevents the unique identification of $\rho(\boldsymbol{r})$ but allows the determination of the autocorrelation function. As will be discussed in Sec. 3.2, neutron grating interferometry only detects scattering perpendicular to the grating lines, resulting in a slit-smearing of the differential scattering cross-section $\left(\frac{d\sigma(\boldsymbol{q})}{d\Omega}(q_x)\right)_{\text{slit}}$. Hence, the one-dimensional correlation function measured by nGI can be described as follows:

$$G(x) = G(x,y=0) = \int \frac{d\sigma(\boldsymbol{q})}{d\Omega}(q_x,q_y,0)dq_y \exp\left(i\left(q_x x\right)\right) dq_x \tag{2.33}$$

$$= \int \left(\frac{d\sigma(\boldsymbol{q})}{d\Omega}(q_x)\right)_{\text{slit}} \exp\left(i\left(q_x x\right)\right) dq_x \ . \tag{2.34}$$

We visualize the different correlation functions in Fig. 2.1 b) using the case of an isolated sphere with a homogeneous scattering length density. For a sphere, the correlation function can be solved analytically [31]:

$$G(x) = 2\pi R^4 \Re\left(\left[1-\left(\frac{x}{2R}\right)^2\right]^{\frac{1}{2}}\left[1+\frac{1}{2}\left(\frac{x}{2R}\right)^2\right]\right.$$
$$\left. + 2\left(\frac{x}{2R}\right)^2\left(1-\frac{x}{4R}\right)^2 \ln\left[\frac{\frac{x}{2R}}{1+\left(1-\left(\frac{x}{2R}\right)^2\right)^{\frac{1}{2}}}\right]\right) \tag{2.35}$$

Restricting $G(x)$ to the real part in the above equations ensures that for $x > 2R$, $G(x)$ equals zero as the function becomes imaginary. The typical procedure for evaluating scattering data generated by an ensemble of discrete scattering centers is to divide the scattering cross-section between the form factor F and the structure factor S. Here, the form factor describes the scattering caused by an isolated scattering center. The structure factor, in contrast, contains information about the interference of neutrons scattered by the distribution of scattering centers in the whole ensemble. An example of such a system is a colloid. Depending on the volume fraction of the particles in the solution, the structure factor becomes more or less important. In the case of an isolated sphere, the structure factor is equal to unity and does not influence the scattering.

2.2.2. Magnetic spin-misalignment scattering under small angles

In electrical steel sheets, the typical grain size is in the 10 µm range, corresponding to a typical size of the magnetic domains in the low micrometer range. Such a structure size results in the case of cold neutrons in scattering angles in the range of 0.001°. This regime of scattering angles is called ultra-small-angle neutron scattering (USANS). The following will present the theory used to describe magnetic scattering in electrical steel, starting from an unpolarized neutron beam. Variations in both the orientation or magnitude of the magnetization $\mathbf{M}$ cause magnetic (U)SANS. Typical SANS instruments measure the macroscopic differential scattering cross-section $\frac{\mathrm{d}\Sigma}{\mathrm{d}\Omega}$. This cross-section is next to the nuclear contribution, a function of the magnetization Fourier coefficients $\widetilde{\mathbf{M}}(\mathbf{q})$, which in turn depend on the magnetic interactions (i.e., exchange, magnetic anisotropy, and magnetoelastic interaction) and external magnetic field. Micromagnetic theory allows us to calculate the spin structure on a length scale accessible to (U)SANS. Hence we can use it to calculate the magnetic cross-sections. Assuming an unpolarized neutron beam without spin resolution, the differential scattering cross-section can be written as [14]:

$$\frac{\mathrm{d}\Sigma}{\mathrm{d}\Omega}(\mathbf{q}) = \frac{8\pi^3}{V} b_H^2 \left(\frac{|\widetilde{N}|^2}{b_H^2} + |\widetilde{M}_z|^2 + |\widetilde{M}_x|^2 \sin^2\theta + |\widetilde{M}_y|^z \cos^2\theta \right. \\ \left. -(\widetilde{M}_x \widetilde{M}_y^* + \widetilde{M}_y \widetilde{M}_x^*) \sin\theta\cos\theta \right) \ . \quad (2.36)$$

Here $\mathbf{q}$ is the scattering vector, V is the scattering volume, and b_H is a constant relating the atomic magnetic moment to the Bohr magneton. $\widetilde{N}(\mathbf{q})$ and $\widetilde{\mathbf{M}}(\mathbf{q})$ are the Fourier coefficients of the nuclear scattering length density and the magnetization $\widetilde{\mathbf{M}}(\mathbf{r})$, respectively. θ denotes the angle between $\mathbf{H_0}$ and $\mathbf{q}$, where $\mathbf{q}$ can be written as $\mathbf{q} \cong q\{\sin\theta, \cos\theta, 0\}$. Also, * denotes the complex conjugate of the respective quantity. Here we assume that the flight path of the neutron is along the z-axis with the magnetic field along the x-axis.
Considering a strong enough magnetic field, i.e., a saturation of the magnetization, the magnetization is $\mathbf{M}(\mathbf{r}) = \{M_s(r), 0, 0\}$. In this case, $\frac{\mathrm{d}\Sigma}{\mathrm{d}\Omega}(\mathbf{q})$ is only influenced by the nuclear scattering and scattering due to the saturation magnetization contrast and reduces to the residual scattering cross-section:

$$\frac{\mathrm{d}\Sigma_\mathrm{res}}{\mathrm{d}\Omega}(\mathbf{q}) = \frac{8\pi^3}{V} \left(|\widetilde{N}| + b_H^2 |M_s|^2 \sin^2\theta \right) \ . \quad (2.37)$$

Accordingly, we can write $\frac{d\Sigma}{d\Omega}(\mathbf{q})$ for non-saturating magnetic fields as [15, 32]:

$$\frac{d\Sigma}{d\Omega}(\mathbf{q}) = \frac{d\Sigma_{res}}{d\Omega}(\mathbf{q}) + \frac{d\Sigma_M}{d\Omega}(\mathbf{q}) \ , \tag{2.38}$$

where $\frac{d\Sigma_M}{d\Omega}(\mathbf{q})$ denotes the spin-misalignment SANS cross-section.

$$\frac{d\Sigma_M}{d\Omega}(\mathbf{q}) = \frac{8\pi^3}{V} b_H^2 \left(|\widetilde{M}_z|^2 + \left(|\widetilde{M}_x|^2 - |\widetilde{M}_s|^2 \right) \sin^2\theta + |\widetilde{M}_y|^z \cos^2\theta \right. \\ \left. -(\widetilde{M}_x \widetilde{M}_y^* + \widetilde{M}_y \widetilde{M}_x^*) \sin\theta\cos\theta \right) \tag{2.39}$$

Close to saturation $\widetilde{M}_x \approx \widetilde{M}_s$, hence $\frac{d\Sigma_M}{d\Omega}(\mathbf{q})$ reduces to:

$$\frac{d\Sigma_M}{d\Omega}(\mathbf{q}) = \frac{8\pi^3}{V} b_H^2 \left(|\widetilde{M}_z|^2 + |\widetilde{M}_y|^z \cos^2\theta - (\widetilde{M}_x \widetilde{M}_y^* + \widetilde{M}_y \widetilde{M}_x^*) \sin\theta\cos\theta \right) \ . \tag{2.40}$$

The above equation contains the scattering due to transverse spin components, which is related to the Fourier amplitudes $\widetilde{M}_y(\mathbf{q})$ and $\widetilde{M}_z(\mathbf{q})$. Additionally, the cross term $(\widetilde{M}_x - \widetilde{M}_y)$ results in a dependence of $\frac{d\Sigma_M}{d\Omega}(\mathbf{q})$ on spatial variations of the longitudinal Fourier component. We note that $\frac{d\Sigma_M}{d\Omega}(\mathbf{q})$ may show strong angular anisotropy not only dependent on the functions $\cos^2\theta$ and $\sin\theta\cos\theta$ but also the Fourier components may be anisotropic [14, 15].

Micromagnetic approach in magnetic spin-misalignment small angle scattering

As noted before, micromagnetic theory can be used to compute the spin structure on the length scale probed by (U)SANS. Hence we can express $\frac{d\Sigma_M}{d\Omega}$ for unpolarized spin-misalignment using micromagnetic calculations, hence connecting information about the exchange stiffness constant and the magnetic anisotropy with neutron scattering. Finally, we can calculate the (slit-smeared) magnetic correlation function $G_M(x,y)$ from the magnetic scattering cross-section, which can later be used to analyze the data gathered using neutron grating interferometry.
Using micromagnetic calculations and a spin-misalignment approach, $\frac{d\Sigma_M}{d\Omega}(\mathbf{q})$ can be written as [33]:

$$\frac{d\Sigma_M}{d\Omega}(\mathbf{q}) = S_H(\mathbf{q}) R_H(\mathbf{q},H_i) + S_M(\mathbf{q}) R_M(\mathbf{q},H_i) \ . \tag{2.41}$$

Here, we have the anisotropy scattering function $S_H(\mathbf{q})$ and the scattering function of the longitudinal magnetization $S_M(\mathbf{q})$. Both are given in cm/sr. Corresponding to these two functions are the dimensionless micromagnetic response functions $R_H(\mathbf{q}, H_i)$ and $R_M(\mathbf{q}, H_i)$. $S_H(\mathbf{q})$ is defined as:

$$S_H(\mathbf{q}) = \frac{8\pi^3}{V} b_H^2 |\widetilde{H}_p|^2 \tag{2.42}$$

and depends on the Fourier coefficient $\widetilde{H}_p(\mathbf{q})$ of the magnetic anisotropy field. $S_M(\mathbf{q})$ contains information about the jump of magnetization at internal interfaces and is defined as:

$$S_M(\mathbf{q}) = \frac{8\pi^3}{V} b_H^2 |\widetilde{M}_z|^2 \ . \tag{2.43}$$

The dimensionless micromagnetic response functions are defined as:

$$R_H(\mathbf{q},\theta,H_i) = \frac{p^2}{2}\left(1 + \frac{\cos^2\theta}{(1 + p\sin^2\theta))^2}\right) \tag{2.44}$$

and

$$R_M(\mathbf{q},\theta,H_i) = \frac{p^2 \sin^2\theta \cos^4\theta^2}{(1 + p\sin^2\theta)} + \frac{2p\sin^2\theta\cos^2\theta}{1 + p\sin^2\theta} \ . \tag{2.45}$$

p is the same dimensionless function $p(q,H_i)$ dependent on the effective magnetic field $H_{\text{eff}}(q,H_i)$ as introduced in Eq. 2.26. For better readability we reproduce the function here:

$$p(q,H_i) = \frac{M_s}{H_{\text{eff}}(q,H_i)} \ , \tag{2.46}$$

with

$$H_{\text{eff}}(q,H_i) = H_i(1 + l_H^2 q^2) \ . \tag{2.47}$$

$H_{\text{eff}}(q,H_i)$ in turn depends on the internal field H_i

$$H_i = H_{\text{app}} - N_d M \text{ and} \tag{2.48}$$

the exchange length

$$l_H(H_i) = \sqrt{\frac{2A}{\mu_0 M_s H_i}} \tag{2.49}$$

R_H and R_M depend on the angle θ due to the magnetodipolar interaction. The ratio $H_p/\Delta M$, q, and H_i define the various anisotropies, which may be seen on a two-dimensional SANS detector [33]. Performing an azimuthal average average of Eq. 2.41, the response functions simplify to:

$$R_H(\mathbf{q},\theta,H_i) = \frac{p^2}{4}\left(2 + \frac{1}{\sqrt{1+p}}\right) \tag{2.50}$$

and

$$R_M(\mathbf{q},\theta,H_i) = \frac{\sqrt{1+p}-1}{2}\ . \tag{2.51}$$

To define a model for S_H and S_M, we assume that our samples are statistically isotropic, nearly saturated, and exhibit small spatial fluctuations of the saturation magnetization and the magnetic anisotropy function. Such a system reduces its dependence to the magnitude of the scattering vector $q = |\mathbf{q}|$. We simplify the system further by considering only a monodisperse system and assume that $\widetilde{H}_p^2(q)$ and $\widetilde{M}_z^2(q)$ are defined by the same single-particle form factor $P(q)$ and structure factor $S(q)$ [34]:

$$\widetilde{H}_p^2(q) = \frac{H_p^2}{(8\pi)^3} V_p^2 P(q) S(q) \tag{2.52}$$

and

$$\widetilde{M}_z^2(q) = \frac{(\Delta M)^2}{(8\pi)^3} V_p^2 P(q) S(q) \tag{2.53}$$

Here V_p is the particle volume, and we choose to use for the sphere form factor $P(q)$:

$$P(q) = 9\frac{j_1^2(qR)}{(qR)^2}\ , \tag{2.54}$$

where j_1 is the first-order spherical Bessel function. We note that the characteristic structure sizes of $\widetilde{H}_p^2(q)$ and $\widetilde{M}_z^2(q)$ are not necessarily identical. Respectively, $\widetilde{H}_p^2(q)$

is related to the volume of the uniform magnetic anisotropy field and $\widetilde{M}_z^2(q)$ to the volume of uniform saturation magnetization.
Assuming $\widetilde{H}_p^2(q)$ and $\widetilde{M}_z^2(q)$ have the same size and shape. This relation simplifies their relation to a constant prefactor. Effectively, they then depend on the ratio $H_p/\Delta M$, where H_p is the mean anisotropy field and ΔM the change in magnetization at internal interfaces. $H_p/\Delta M$ then defines the angular anisotropy, the asymptotic power-law dependence of $d\Sigma_M/d\Omega$ and the characteristic decay length of fluctuations of the spin-misalignment [32].

Micromagnetic correlation function

In analogy to the nuclear correlation function ($G(x,y)$) defined in Eq. 2.32 for the nuclear cross-section, we can define the magnetic correlation function $G_M(x,y)$ of the spin-misalignment cross-section $\frac{\mathrm{d}\Sigma_\mathrm{M}}{\mathrm{d}\Omega}(\mathbf{q})$, i.e., [15]:

$$G_M(x,y) = \frac{1}{8\pi^3}\int \frac{\mathrm{d}\Sigma_\mathrm{M}}{\mathrm{d}\Omega}((q_x,q_y,0))\exp(i(q_x x + q_y y))dq_x dq_y \tag{2.55}$$

We note that this description of the correlation function is not an autocorrelation function as in $G(x,y)$. While the magnetic correlation function may be defined as an autocorrelation function of the spin-misalignment as shown in Refs. [15, 35–37], this result does not correspond to an experimentally accessible quantity, such as $\frac{\mathrm{d}\Sigma_\mathrm{M}}{\mathrm{d}\Omega}(\mathbf{q})$. Like the nuclear correlation function in Eq. 2.34, the magnetic correlation function G_M is also slit-smeared during nGI measurements. Hence, G_M can be simplified for one-dimensional data to [15]:

$$G_M(x) = \int \left(\frac{d\Sigma_\mathrm{M}}{d\Omega}(q_x)\right)\frac{\sin(q_x x)}{q_x x}q_x^2 dq_x \tag{2.56}$$

Together with the micromagnetic scattering functions shown in this section, we will use this equation in Sec. 5.3 to analyze the size of the magnetic domains of NGOES.

3 Experimental Techniques

3.1. Neutron imaging

Neutron imaging is a non-destructive method providing information about the internal structure of a sample [38]. The material contrast of neutrons is determined by the specific atomic core structure of the material as they interact with the nucleus but not the electron hull. Neutrons interact strongly with several light elements such as hydrogen, lithium, or boron, while heavier elements such as aluminum, iron, and lead show comparably less interaction [39]. Neutron imaging has a large variety of applications in condensed matter physics [40–43], materials science [44–47], engineering [48–50], medicine [51] and cultural heritage [52–54]. Due to the often complementary contrast of neutrons and X-rays, neutron imaging is also used alongside X-ray imaging to obtain additional information [55, 56] about a sample.
Fundamentally, neutron imaging functions similarly to a pinhole camera. The neutron source, which may be a moderator or the exit of a neutron guide, is aligned with a pinhole-type collimator, sample and a spatially resolved detector. Fig. 3.1 illustrates this principle. The distance between the collimator and the sample collimates the neutrons. A spatially resolved neutron detector detects the neutrons passing through the sample. The inner structure of a sample determines the attenuation of the neutron beam, generating an intensity contrast. Detectors used in neutron imaging typically

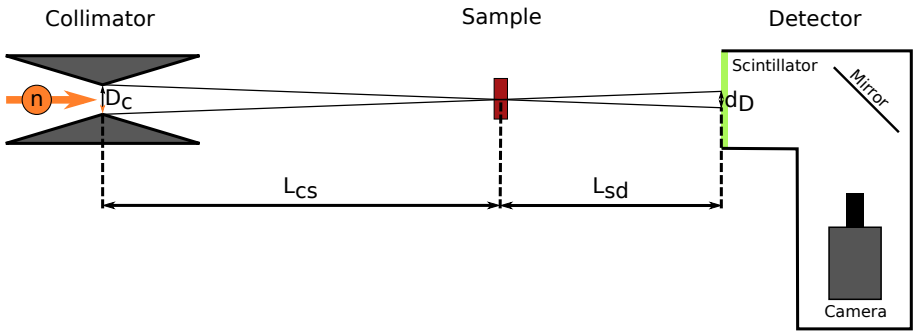

Figure 3.1.: Sketch of a neutron imaging beamline. The distance between the collimator and the sample L_{cs} collimates the neutrons. A spatially resolved neutron detector detects the neutrons passing through the sample. The collimator diameter D_c, the distance between sample and detector L_{sd} and L_{cs} defines the smearing of the sample on the detector d_D according to Eq. 3.1. The detector typically consists of a scintillation screen, transforming the neutron image into a visible light image, an optical system comprising at least one mirror and a lens, and a camera.

comprise a scintillation screen, an optical system, including at least one mirror, a lens, and a scientific CMOS or CCD camera. The scintillation screen converts neutrons into visible light generating an optical image from the transmitted neutron intensity. This image is then recorded using the optical system and the camera.
Next to the achievable contrast due to attenuation, spatial resolution is the most crucial characteristic in imaging. In a neutron imaging beamline, there are two distinct contributions to the spatial resolutions to consider: the geometric resolution of the beamline and the resolution of the detector. The smearing of a single point in the sample on the detector by the beam divergence constrains the geometric resolution. The smearing is defined by the collimator diameter D_c, the distance between the collimator and sample L_{cs}, and the sample-to-detector-distance (SDD) L_{sd}. The maximum diameter d_D of smearing can be calculated using the following equation:

$$d_D = \frac{D_c}{L_{cs}} L_{sd} \ . \tag{3.1}$$

Fig. 3.1 shows a graphical representation of this equation. Accordingly, reducing L_{sd} or increasing the 'L/D'-ratio L_{cs}/D_c[1], improves the geometrical resolution. Increasing L_{cs}/D_c also decreases the neutron flux at the sample position. Hence a compromise between resolution and neutron flux has to be chosen.
The camera, the optical system and the scintillation screen influence the detector resolution. Currently a resolution in the low µm range can be achieved [57–61].

3.2. Neutron grating interferometry

Neutron grating interferometry (nGI) is a relatively recent addition to neutron imaging [62]. It enables the spatially resolved, simultaneous analysis of the transmission- (TI), the differential phase contrast- (DPCI) and the scattering/dark field image (DFI) of a sample [63, 64]. Particularly the DFI has received great interest as a method to spatially resolve ultra-small-angle-scattering of neutrons (USANS) caused by a variation of the nuclear and magnetic scattering length densities in the micrometer regime. The working principle of nGI is the generation of an interference pattern using gratings and subsequently analyzing the alteration of the pattern caused by a sample. nGI-setups can be classified according to the method of generating and analyzing the interference pattern. The most common type is the Talbot-Lau type interferometer based on the

1 The subscripts in L_{cs}/D_c were introduced to differentiate the geometrical resolution from a corresponding ratio used to describe neutron grating interferometry (Sec. 3.2).

Talbot-Lau interference effect. Such interferometers consist of two absorption gratings and one phase shifting grating [13, 62, 65–67]. A rarer type of interferometer is the far-field interferometer consisting of two [68] or three [69] phase-shifting gratings. Below we give a detailed explanation of Talbot-Lau interferometry.
Typical applications are the analysis of defects in additively manufactured samples [12, 13], investigation of magnetic domains in bulk ferromagnets [64, 65, 70], visualization of magnetic fields [71] and analysis of the vortex lattice domains in superconductors [11, 72–75]. Recently, nGI operation also shifted from purely qualitative analysis of the presence of microstructures in a sample towards a quantitative tool, allowing to analyze the orientation and size of microstructures spatially resolved[67, 76–79].

3.2.1. Principles of Talbot-Lau neutron grating interferometry

The Talbot-Lau interference effect is the basic principle of a Talbot-Lau interferometry setup (TLI-setup), where a phase grating G_1 introduces a phase modulation into a sufficiently coherent (spatial and temporal) neutron beam. Downstream of the grating, the phase modulation transforms into a pure phase or intensity modulation in regular intervals. A mixture of phase and intensity modulation is observed between these intervals. The distances where a pure phase or intensity modulation is observed are called the fractional Talbot distances d. The following equation defines the distances [80]:

$$d = n \cdot M \frac{p_1^2}{2\lambda\eta^2}. \tag{3.2}$$

Here n denotes the order of the fractional Talbot distance, where odd (even) n results in a pure intensity (phase) modulation respectively. p_1 is the period of the phase grating G_1 and λ the incoming wavelength. Here $\eta = 1$ and $\eta = 2$ accounts for a $\pi/2$- and a π-shifting phase grating, respectively. A π-shifting phase grating doubles the frequency of the interference pattern with respect to the frequency of the phase grating. M is the magnification effect of a conical neutron beam resulting from the pinhole geometry. In an ideal case, only the phase grating is necessary to generate and analyze the interference pattern. In this case, we define the ideal case as a highly monochromatic neutron beam with perfect spatial coherence. Furthermore, we assume a detector capable of directly resolving the interference pattern. Placing such a detector at an odd fractional Talbot distance allows us to analyze the generated interference pattern. Introducing a sample into the neutron beam changes the pattern depending on the effect of the sample. Attenuation in the sample reduces both the mean intensity as well as the amplitude of the interference pattern. Refraction introduces a phase

shift while scattering reduces the amplitude without changing the mean intensity. However, a sufficiently spatially coherent beam would require an infinitesimally small D_c in a real interferometer, reducing the neutron flux below practical limits. While current detector technology can resolve structures in the low µm range, the field of view is limited to a few mm. In contrast, standard neutron velocity selectors can easily achieve the required temporal coherence. We use two additional absorption gratings (G_0 and G_2) to overcome the aforementioned limitations. G_0 increases the incident intensity with the required spatial coherence while G_2 allows to analyze the interference pattern. Fig. 3.2 illustrates the main components of a TLI-setup inside an imaging beamline. The source grating G_0 ensures spatial coherence of the neutron beam in one

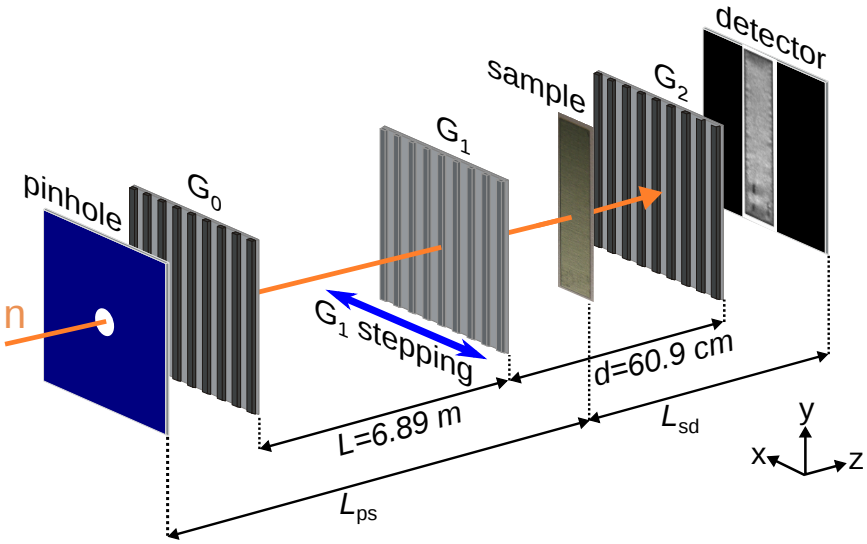

Figure 3.2.: Illustration of a TLI-setup in an imaging beamline consisting of the source grating G_0, the phase grating G_1 and the analyzer grating G_2. The sample is typically placed between G_1 and G_2. The collimator and detector are part of the imaging beamline. The figure is already published in [65].

direction by imprinting a line pattern on the neutron beam, creating an array of line sources. The width of every line source is chosen to be small enough that neutrons from each line source are coherent while incoherent compared to the rest of the line array. The TLI-setup parameters define the period of the line source (see Eq. 3.3). As noted before, an interferometer could also achieve spatial coherence by reducing the collimator of the imaging beamline, but as a result, the neutron intensity decreases below practical values.

Analyzing the scattering in the USANS regime requires an interference pattern with a periodicity in the low micrometer range. This periodicity is below the typical spatial resolution of an imaging detector with a medium to large field of view (≈

80 mm × 80 mm). The analyzer grating G_2 allows to analyze the interference pattern generated by G_1. The periodicity of G_2 matches the periodicity of the interference pattern. G_2 blocks parts of the interference pattern, e.g., the minima, and allows others to pass, e.g., the maxima. Step-wise translation of one of the gratings perpendicular to the grating lines shifts the whole interference pattern. We analyze the resulting intensity modulation in every detector pixel, recovering the generated interference pattern. Ideally the pahse grating G_1 is moved as the absorption gratings G_0 and G_2, may produce, at high L_{cs}/D_c ratios, additional oscillations distorting the measured signal [81]. This type of scan is called stepping or nGI-scan. An exemplary scan is presented in Fig. 3.3 b) and c).

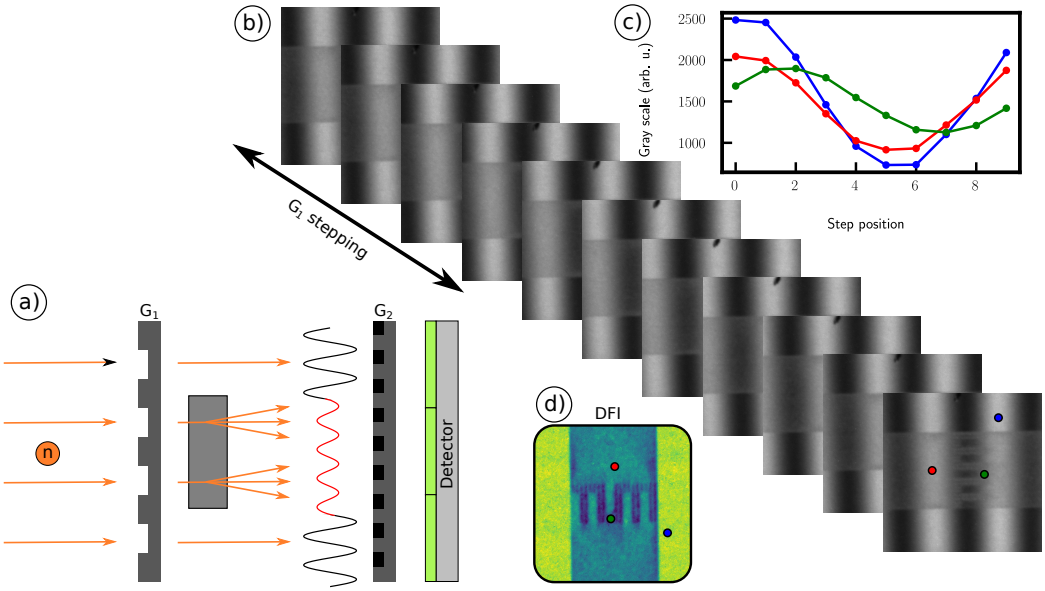

Figure 3.3.: a) Sketch of DFI generation due to USANS caused by a sample. At the position of G_2, an intensity modulation (black sine) is generated by the phase grating G_1. In the sample (gray rectangle), neutrons (orange) are scattered and reduce the intensity modulation (red sine). Moving one of the gratings shifts the intensity pattern, causing an intensity modulation in every detector pixel. b) Example of an nGI-scan using an embossed electrical steel sheet. Shown are the ten raw images (grayscale) of a scan. In d), the evaluated DFI is shown in color. Please note the evaluated DFI has been rotated clockwise by 90°. In c), the intensity oscillation in a reference (blue), a non-embossed (red) and an embossed area (green) in the electrical steel sheet are shown.

For an optimal performance of the nGI, the inter-grating distances, periods of the gratings and the neutron wavelength have to adhere to specific relations. The

interference pattern created by every line source generated by G_0 has to be projected constructively onto the periodic profile of G_2 according to the intercept theorem [82]:

$$\frac{d}{L} = \frac{p_2}{p_0} \ . \tag{3.3}$$

L and d denote the distance between G_0 and G_1 and G_1 and G_2, respectively. p_0 and p_2 are the periodicities of G_0 and G_2, respectively. Furthermore, the periodicity of G_2 needs to match the periodicity of the magnified (M) interference pattern created by G_1 [80]:

$$p_2 = \frac{L+d}{L}\frac{p_1}{\eta} = M\frac{p_1}{\eta} \ . \tag{3.4}$$

Together Eq. 3.2, 3.3 and 3.4 govern the relation of grating periods, inter grating distances and wavelength of a TLI-setup. Deviating from these three relations should be avoided as it reduces the contrast of the interference pattern (visibility) or the appearance of Moirè fringes. The fractional Talbot-order n in Eq. 3.2 can be chosen according to the desired correlation length ξ_{GI} range of the setup and the allowed G_1-G_2 distance.
The correlation length ξ_{GI} is defined as [76]:

$$\xi_{GI} = \frac{\lambda L_{sg}^{eff}}{p_2} \ , \tag{3.5}$$

where L_{sg}^{eff} is the effective sample-to-grating (G_2) distance. L_{sg}^{eff} depends on the placement of the sample with respect to G_1 and is calculated by [80]:

$$L_{sg}^{eff} = \begin{cases} (L+d-L_{sg})\frac{d}{L} & \text{for } L_{sg} > d \\ L_{sg} & \text{for } L_{sg} < d \end{cases} \ , \tag{3.6}$$

dependent on the sample to grating (G_2) distance L_{sg}. Accordingly, placement of the sample between G_1 and G_2 allows to tune the correlation length ξ_{GI} linearly by adjusting L_{sg}. In contrast, a placement between G_0 and G_1 significantly reduces the effect of L_{sg} on ξ_{GI}. Additionally, a variation of the correlation length by changing λ is possible. We will discuss the correlation length in more detail in Sec. 3.2.2.
Depending on the grating position x_{GI} perpendicular to the neutron beam and the

grating lines, the intensity oscillation in every pixel (k,l) of the detector is described by [83]:

$$I\left(x_{\mathrm{GI}},k,l\right) = a_0\left(k,l\right) + a_1\left(k,l\right)\cos\left(\frac{2\pi x_{\mathrm{GI}}}{p_{\mathrm{i}}} - \varphi\left(k,l\right)\right) \ , \tag{3.7}$$

here $a_0(k,l)$ is the mean value, $a_1(k,l)$ the amplitude and $\varphi(k,l)$ the phase of the oscillation. Using fitting algorithms [84, 85], $a_0(k,l)$, $a_1(k,l)$ and $\varphi(k,l)$ are determined. From these parameters, we can calculate TI, DPCI and DFI :

$$TI(k,l) = \frac{a_0^{\mathrm{s}}(k,l)}{a_0^{\mathrm{r}}(k,l)} \tag{3.8}$$

$$DPCI(k,l) = \varphi^{\mathrm{s}}(k,l) - \varphi^{\mathrm{r}}(k,l) \tag{3.9}$$

$$DFI(k,l) = \frac{a_1^{\mathrm{s}}(k,l)/a_0^{\mathrm{s}}(k,l)}{a_1^{\mathrm{r}}(k,l)/a_0^{\mathrm{r}}(k,l)} = \frac{V^{\mathrm{s}}}{V^{\mathrm{r}}} \ . \tag{3.10}$$

Here x^{s} and x^{r} denote an nGI-scan with and without a sample, respectively. The two measurements are required as nGI measures the change in $I\left(x_{\mathrm{GI}},k,l\right)$ due to the influence of a sample. One important quantity to describe the performance of an nGI-setup (TLI or other) is the visibility V which is the ratio between $a_1(k,l)$ and $a_0(k,l)$, i.e., the ratio of the extrema of the intensity oscillation to its average.
The transmission image (TI) records the attenuation of neutrons in a sample and corresponds to the transmission measured by standard radiography. The differential phase contrast image (DPCI) denotes the phase shift of the interference pattern due to the sample. In the context of this thesis, neither the TI nor the DPCI has an application in the analysis of the magnetic properties of electrical steel. Hence, in the following, we will only explain the contrast modalities and limitations of the DFI in detail.

3.2.2. Dark field contrast

The dark-field image (DFI) describes locally resolved the ultra-small-angle-scattering within a material. Discontinuities in both the magnetic or material microstructure may cause this scattering. In Fig. 3.3 a), the influence of scattering on the intensity oscillation is sketched, and d) presents the resulting DFI. We follow an approach given in Ref. [76] to quantify the DFI. The scattering causes a momentum transfer q to the neutron resulting in a small deflection of the neutron. Due to the single dimensionality of nGI, only a momentum transfer q_{x} perpendicular to the grating lines

may be observed. Corresponding to the momentum transfer q_x the neutron is deflected under the angle ϑ:

$$\vartheta \approx \frac{q_x \lambda}{2\pi} \ , \tag{3.11}$$

when considering the small angle approximation ($\sin\vartheta \approx \tan\vartheta \approx \vartheta$). Hence, q_x corresponds to a shift of the interference pattern along the x-axis, which in turn translates into a phase shift $\Delta\varphi$:

$$\Delta\varphi = \frac{2\pi\vartheta}{p_2} L_{sg}^{eff} \ . \tag{3.12}$$

By combining equations 3.11 and 3.12 $\Delta\varphi$ is connected to q_x:

$$\Delta\varphi = \frac{\lambda L_{sg}^{eff}}{p_2} q_x = \xi_{GI} q_x \ . \tag{3.13}$$

The (auto)correlation length ξ_{GI} combines the instrument-specific parameters neutron wavelength λ, period of the analyzer grating p_2 and effective sample to analyzer distance L_{sg}^{eff}. ξ_{GI} describes the length scale the nGI setup is sensitive to. The DFI has been derived from theory under consideration of multiple scattering and neutrons passing through without interaction as [76, 86]:

$$DFI = \exp\left[\Sigma t \left(\frac{G(\xi_{GI})}{G(0)} - 1\right)\right] \ . \tag{3.14}$$

Σ denotes the dark field extinction coefficient, t is the sample thickness and $G(\xi_{GI})$ is the correlation function as defined in equation 2.34 ($x = \xi_{GI}$). Due to the single dimensionality of the considered grating systems, $G(\xi_{GI})$ can only be evaluated perpendicular to the grating lines.

3.2.3. Analysis of the correlation function

From Sec. 3.2.2, we know that the DFI signal is defined by the correlation function G probed at a specific correlation length ξ_{GI}. Hence, scanning a range ofξ_{GI} allows us to gather information about the trend of G, which contains information about the microstructure of a sample. A change of ξ_{GI} requires either a change in λ or in L_s^{eff}. This approach has previously been used in, e.g., Refs. [67, 77, 79] to determine the diameter and concentration of colloids in suspension. The range of accessible ξ_{GI} is

restricted by geometric limits (L_s^{eff}) and the wavelength dependence of the visibility V, which are defined by the specific nGI-setup and the neutron spectrum.
In case one adjusts ξ_{GI} by detuning from the design wavelength, V decreases as the Talbot-distance d changes (Eq. 3.2), while the geometric considerations of Eq. 3.3 and 3.4 are wavelength independent. A further problem of correlation length adjustment by wavelength variation is the limited range of accessible wavelengths. For the ANTARES beamline wavelengths from 1.6 Å to 6.0 Å [87] are accessible, effectively resulting in a correlation length range accessible by solely changing the neutron wavelength of $\xi_{\text{GI}}^{\text{min}} \leq \xi \leq 3.75\xi_{\text{GI}}^{\text{min}}$ (see Eq. 3.5), i.e., less than one order of magnitude. Here $\xi_{\text{GI}}^{\text{min}}$ is the minimum correlation length achieved at a constant L_s^{eff} and $\lambda = 1.6$ Å. The quadratic wavelength dependence of Σ is another effect that causes an additional change in the DFI signal during scanning of the correlation length [88].
In contrast, a variation of L_s^{eff} allows access to a larger range of correlation lengths. Provided the geometry of the nGI-setup has been chosen correctly, multiple orders of magnitude in ξ are accessible [13, 65]. Simultaneously, the nGI-setup may operate at its design wavelength. A major drawback of adjusting ξ_{GI} by L_s^{eff} is the decreased spatial resolution due to an increased distance between sample and detector when accessing larger correlation lengths.
As noted in Sec. 2.2, G denotes the overlap of a particle with a copy of itself displaced by a vector r. As a result, regardless of the exact particle shape, at displacements larger than the particle dimensions, G decays to zero. Hence, measuring G by probing it a various ξ_{GI} allows us to gather information about the size and shape of the microstructure in a sample.

Limitations

It is essential to comprehend the limitations inherent in nGI, which are particularly prevalent during quantitative analysis, to understand the results presented in this thesis. The most consequential restriction here is the minimum detectable DFI signal (DFI_{min}). As the DFI signal is the ratio between the sample V^s and reference visibility V^r, its value varies between zero and unity. For $DFI = 0$ to occur, V^s has to be zero. The visibility is the ratio between the amplitude a_1 and the mean a_0 of the intensity oscillation generated by the nGI-setup. Hence, for V^s to be zero, a_1 needs to be zero. However, an a_1 of zero implies zero noise; otherwise, the intensity changes randomly over an nGI-scan. Effectively, this causes the evaluation algorithms to always result in non-zero values for V^s and the DFI to remain at a non-zero minimum value, regardless of actual visibility degradation due to scattering. The shot noise defines the minimum value of V^s. Due to the random nature of noise, the recovered oscillation phase is also arbitrary. Therefore the DPCI can be used to detect such conditions, as it shows

random noise in areas with minimum DFI signal.
Assuming shot noise caused by the scintillation screen, i.e., neutron detection, is the dominant noise contribution, a single Poisson distribution can model the strength of the random variation. For a number of counts N, the standard deviation is given by $\sqrt{N}$. Hence increasing the counting time decreases, relative to the signal, the influence of the noise. We note that depending on the specific detector system, other instances of noise, e.g., dark current (thermal) and read noise, may also play a significant role in determining the noise registered during a measurement. Regardless of the noise source, noise in an nGI-scan will cause slight variations in recorded intensity even without an intensity oscillation caused by the nGI-setup. In the following, we will analyze the effect of Poisson noise on the intensity oscillation. The effect we consider relates to but differs from pure statistical uncertainty in the measured DFI. A discussion about statistical uncertainties in the DFI value can be found in [89].

Poisson noise

Modeling the Poisson noise in a typical detector for neutron imaging is complex. Naively one may apply Poisson noise to the gray values measured by the digital camera. This approach has significant problems, as it omits the gain factor of the camera, i.e., one detected photon resulting in multiple gray values due to electronic amplification. Furthermore, even at a gain equal to unity, i.e., one detected photon equals a gray value, this naive approach only considers the Poisson noise inherent in detecting photons. For the complete picture, the effect of the optical system, the quantum efficiency of the camera and the Poisson noise of the neutron detection in the scintillator also need to be taken into account[1].
On average, a neutron absorbed in the scintillator is converted into multiple photons (light yield). In the case of ZnS:Cu/^{6}LiF scintillators, one of the standard scintillators used, one neutron is converted on average into $\approx$ 100000 photons [92] from which the camera detects a small percentage. This ratio is the neutron to photon conversion factor (npc). This factor encompasses the light yield and the probability that the camera detects the converted light. This detection probability depends on the quality of the optical system (lens and mirror), the quantum efficiency of the camera and the angular dependence of the emitted light. Hence, this conversion factor is highly dependent on the specific detector setup, i.e., camera, optics and used scintillating material.

1 In our calculations, we are omitting the influence of read noise and dark current (thermal) noise in the camera. For typical nGI measurements and detectors at ANTARES, this approach is valid, as these two noise contributions are negligible compared to Poisson noise [65, 90, 91].

We must also consider that the detection probability of neutrons in a scintillating material depends on its thickness along the beam direction and the incoming neutron wavelength.
Consequently, the scintillator absorbs a fraction of an arbitrary incoming neutrons flux. As discussed, these detected neutrons (N) will have a Poisson distribution (Pois(N)). The camera, in turn, detects several photons P, given by $npc \times \text{Pois}(N)$, also with a Poisson distribution. Afterwards, this value is multiplied by the camera gain g to get the gray value. Hence we can write for the acquired gray values G:

$$G = g \times P = g \times \text{Pois}(npc \times \text{Pois}(N)) \tag{3.15}$$

Using this equation, the knowledge about the detected neutron flux, and the used detector system, we simulated the influence of Poisson noise on the intensity oscillation. A similar approach modelling the Poisson noise has been discussed in [93].
For our simulation, we first generate the ideal oscillation of the neutron beam for one pixel when performing a stepping scan of the nGI phase, which results in discrete data points following a sinusoidal curve, according to Eq. 3.7. The mean value (a_0), amplitude(a_1) and phase (φ) of this curve can be freely defined. We further allow to vary the number of data points generated per phase step, which corresponds to the number of images per phase step (IpS) during a measurement. Afterward, we apply Poisson noise to every data point according to the neutron count, thereby displacing the neutron count from the ideal sinusoidal curve. In the next step, we multiply the resulting neutron count by the conversion factor (npc), resulting in the number of photons detected by the camera. We further apply Poisson noise to this value. Assuming that the gain (g) equals unity, the number of photons detected with added Poisson noise equals the gray values the camera displays.
We fit the resulting noisy sinusoidal curve using Levenberg-Marquardt non-linear least squares fitting to determine the parameters of the intensity oscillation. In Fig. 3.4, this process is sketched. To achieve the mean influence of noise on the DFI signal, we repeat the algorithm mentioned above n times and average the results to gather the average influence of Poisson noise. n has been set to 2500 for the simulations, following the statistical analysis discussed in [89].
As shown in Fig. 3.5, we simulated an intensity oscillation with known visibility and added Poisson noise to the discrete values according to Eq. 3.15. Multiple images per phase step (IpS) can be generated to simulate a typical measurement accurately. In table 3.1, the parameters for the simulations are shown. In Fig. 3.5 a) the detected neutrons are varied from $N = 15$ to $N = 1920$ (purple to yellow), in b) the IpS are varied from 3 to 384 and in c) the conversion factor npc is varied from 0.625 to 80.

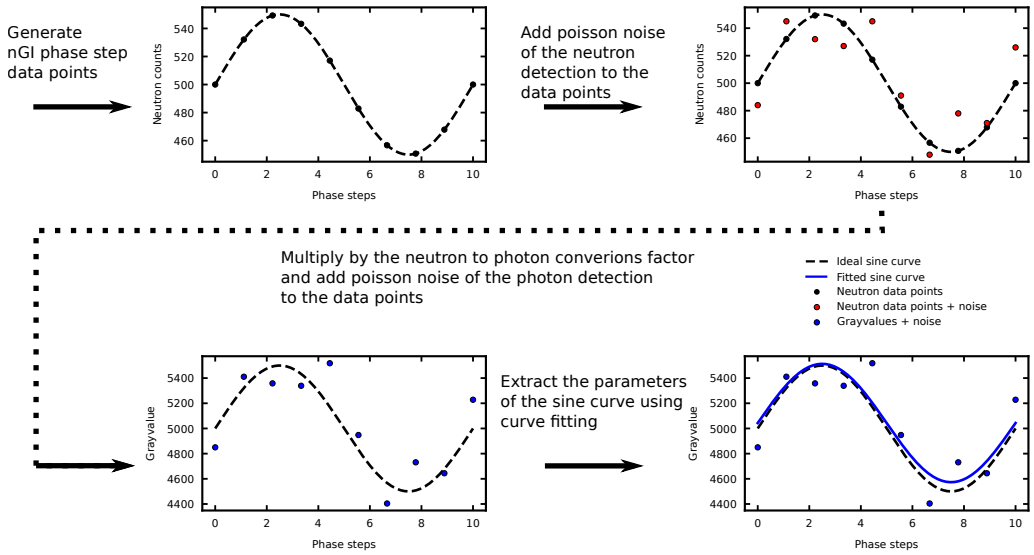

Figure 3.4.: Sketch of the process used to evaluate the influence of noise on the DFI signal.

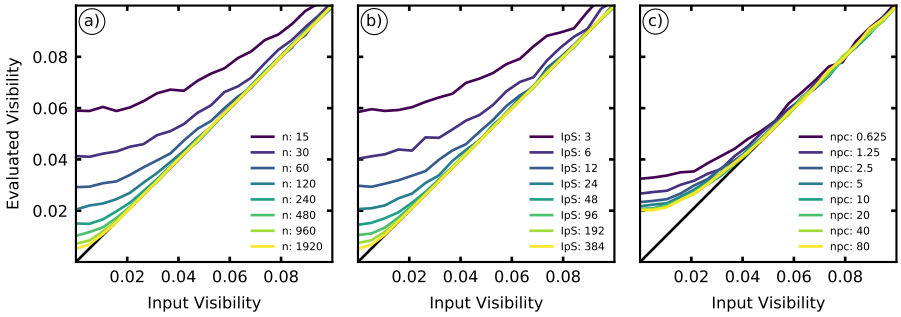

Figure 3.5.: Deviation of evaluated visibility due to Poisson noise with input visibility and measurement time changes. In a) the neutron count is increased from $N = 15$ to $N = 1920$, correspondingly the minimum evaluated visibility decreases from 0.06 to 0.005. Similarly, in b) the minimum evaluated visibility decreases from 0.06 to 0.005 for an increase in measurements per phase step from 3 n to 384 n, while keeping the neutron counts constant. In both cases, the neutrons detected per intensity oscillation rises by the same amount. Hence the decrease in minimum visibility is also similar. In c) the *npc* conversion factor increases from 0.625 to 80. The minimum visibility level of 0.02 is reached with $npc \geqq 5$, indicating that the Poisson noise of the neutron detection dominates here.

The black line indicates the the ideal behaviour of the evaluation, i.e., input visibility equals the evaluated visibility. The evaluated visibility in a) and b) decreases when decreasing the input visibility before leveling off at a minimum visibility. The minimum

Figure	Neutrons	npc	phase steps	IpS
a)	$N = 15$ to $N = 1920$	10	10	3
b)	120	10	10	3 - 384
c)	120	0.625 - 80	10	3

Table 3.1.: Parameters for the simulation series presented in Fig. 3.5. The neutron count in a), values per phase step in b) and *np*-factor in c) increase exponentially.

visibility depends on the total amount of neutrons detected. Hence, the minimum visibility in a) and b) decreases similarly when the total amount of detected neutrons is increased by detecting more neutrons per image or more IpS. In c), the evaluated visibility also follows the ideal behavior before deviating and leveling off. An increase in the conversion factor shows a decrease in recoverable visibility for *npc* values from 0.625 to 5. For $npc > 5$, the minimum recoverable visibility is constant, resulting from the constant neutron count rate, further indicating that in cases where the photon count rate is significantly higher than the neutron count rate, the Poisson noise of the neutron count rate dominates. Conversely, a high *npc* factor reduces the possible neutron dynamic range due to the finite dynamic range of cameras. A photon count rate significantly below the neutron count rate has not been examined, as this case is atypical for detectors used for neutron imaging.

The incident neutron flux at the scintillation screen needs to be known to use these calculations. For the nGI-setup installed at ANTARES, we can estimate the detected neutron flux. From [94] and [95] the differential neutron flux at 4 Å can be estimated as $\approx 2.5 \times 10^7\,\mathrm{cm^{-2}\,s^{-1}\,Å^{-1}}$ for an $L/D = 250$. Using the bandwidth $\frac{\Delta\lambda}{\lambda} = 10\,\%$ of the NVS at ANTARES we get a neutron flux of $1 \times 10^7\,\mathrm{cm^{-2}\,s^{-1}}$ incoming into the neutron grating interferometer. We provide a detailed derivation of these values in A. Since the nGI-setup has two absorbing gratings which absorb, based on their duty cycles (see Sec. 4.2), 70 % and 50 %, respectively, the neutron flux is reduced to $1.5 \times 10^6\,\mathrm{cm^{-2}\,s^{-1}}$. The standard nGI-setup detector system at ANTARES consists of an Andor Neo 5.5 sCmos camera, a ZEISS Milvus 2.0/100M ZF.2, two mirrors and a RC tritec ZnS:Cu/^{6}LiF scintillator with 100 µm thickness. The effective pixel size of this setup with a FoV of 84.5 mm × 71.3 mm is 33 µm, hence the neutron flux per pixel is $16.9\,\mathrm{s^{-1}}$. The used scintillation screen has, at 4 Å, a detection probability of $\approx 23\,\%$. Hence the detector system has a neutron detection rate of $\approx 3.9\,\mathrm{s^{-1}}$ per pixel. Experiments with the nGI-setup show that at $g = 1$ the detector counts, on average, 116 gray values per second. Hence our conversion factor *npc* between absorbed neutrons to detected photons is ≈ 29.7. We can then use Eq. 3.15 to simulate the noise during an nGI-scan and compare it to measurement results.

In Fig. 3.6, we compare the trend of a) the simulated visibility (lines) and b) the

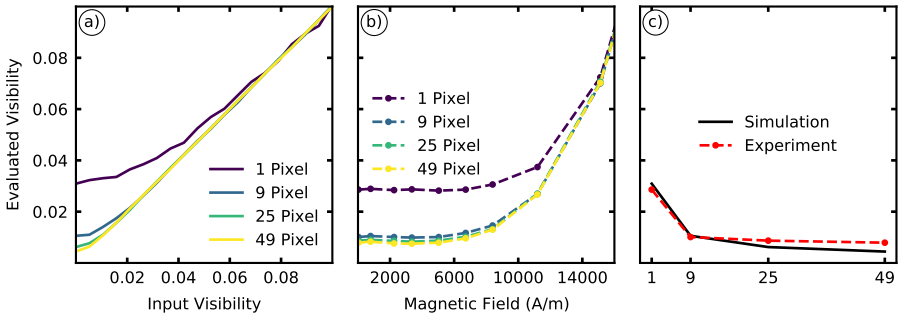

Figure 3.6.: Comparison of a) the trend of the visibility predicted by simulation with b) the measured visibility trend in an NGOES sample dependent on the number of pixels binned together. Please note that the values given on the x-axis of a) and b) are not the same. For the simulation in panel a) we show the evaluated visibility vs. the input visibility. The input visibility is not available for the measurement data in b). Therefore, the evaluated visibility vs. the applied magnetic field is plotted. In c), the change of the minimum visibility dependent on the amount of binned pixels is plotted.

measured visibility (circular markers and dashed lines) for different amounts of neutrons per evaluated pixel. An electrical steel sheet with a thickness of 350 µm was used as a scattering sample. Applying a magnetic field allows to adjust the amount of scattering and the visibility value determined. To adjust the number of neutrons measured per evaluated pixel, 1 to 49 pixels have been binned before evaluating the data. Effectively, this causes an increase in neutron statistics. Please note that the x-axis of the two plots is not directly comparable. While a) shows the input visibility of the simulation, b) shows the applied magnetic field in the sample.
For the measurement and, subsequently, the simulation of the visibility curve, we set the mean detected gray value count to 1160 per image, three images per phase step and 10 phase steps. For both the simulation and measurement, the minimum visibility decreases when the amount of binned pixels increases. Also, as expected, the jump in minimum visibility is the largest from 1 binned pixel to 9 binned pixels. Here, the most significant relative rise in detected neutrons is occurring, i.e., neutron statistics. As expected from the simulation, the evaluated visibility deviates above the minimum evaluated visibility, i.e., in the case of the 1 Pixel measurement, the minimum visibility is $V = 0.029$. At the same time, the visibility deviates at $V \approx 0.04$. In c), the minimum visibility recovered from the measurement (red markers) is compared to the

minimum simulated visibility (black line). The simulation predicts a slightly lower minimum visibility than the measurement, which may be caused by the exclusion of some noise contributions in our model.
The minimum detected visibility, in turn, affects together with V^r of the setup the minimum DFI, i.e., the maximum amount of scattering observed. In Fig. 3.7, we demonstrate the effect of the simulated minimum DFI cutoff on the evaluated correlation function $G(\xi)$. As a model function, the DFI signal caused by an isolated sphere is used (see, e.g., Eq. 5.1 and 5.2). As parameters the diameter D was set to 10 µm, the variance σ to 0 µm, the sample thickness t to 1 mm and the dark field extinction coefficient Σ was varied between $10\,\mathrm{cm}^{-1} \leq \Sigma \leq 80\,\mathrm{cm}^{-1}$. Here we sample the dependence of the DFI value (circular markers) on the correlation length ξ_{GI} every µm for varying scattering strengths. The scattering strength increases from top to bottom. In a), an ideal case is shown, where the DFI signal, regardless of value, can be recovered. In b) a minimum DFI signal of 0.05 has been simulated.

Considering that one can only probe discrete points of the correlation function, a

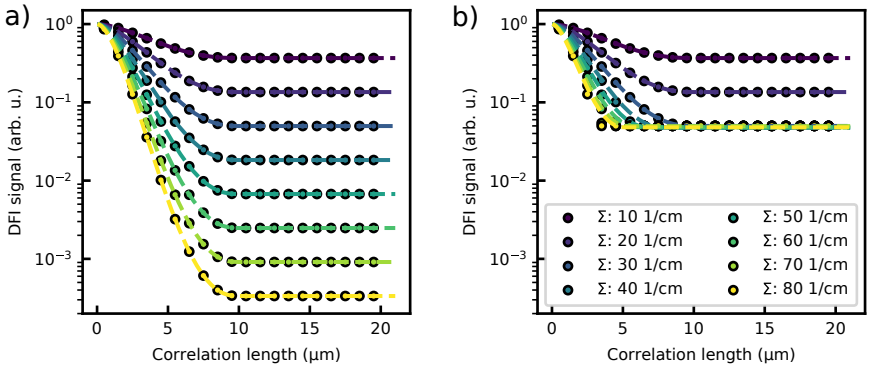

Figure 3.7.: Comparison of the change in the DFI signal due to variation of the linear extinction coefficient Σ. In a), the ideal case is presented, while b) shows the effect of noise-induced minimum DFI cutoff.

fit of these discrete points will lead to a distortion of the recovered parameters with respect to the input parameters. The sampled points were fitted using Eq. 5.1 and 5.2 showing the effect of discrete sampling and minimum DFI on the recovered parameters. The dashed lines denote the fitted functions. In Fig. 3.8, we compare the trend of a) the evaluated diameter D and b) the evaluated linear extinction coefficient Σ with (blue) or without (red) noise with respect to the input Σ.

As expected, the evaluation of the simulated data without any noise (red) causes a) the evaluated diameter and b) the evaluated Σ to follow the respective input values perfectly. In contrast, the evaluation of simulated data with noise (blue) shows a significant deviation from the input values. First, Σ and D follow the input values, as

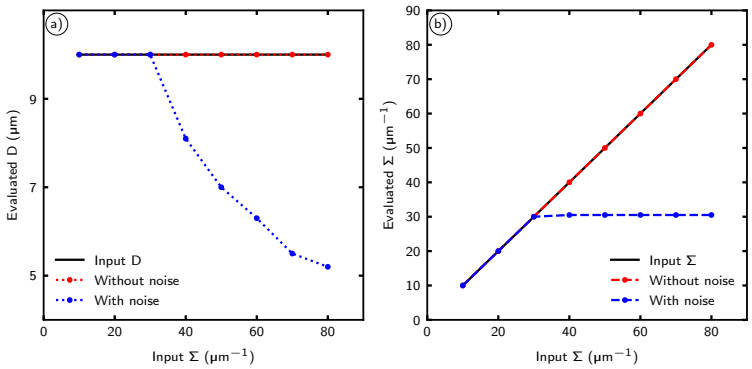

Figure 3.8.: Trend of a) diameter D and b) Σ evaluated from the simulated DFI signal shown in Fig. 3.7. The black line denotes the input value, red the data without noise and blue the data with added noise.

the DFI values are above the cutoff. When the cutoff of the DFI signal is reached, Σ levels off at a value of 30.5 cm^{-1}, which corresponds to a DFI value of 0.05. In contrast, D continues to decrease with increasing input Σ. Accordingly, the evaluated diameter values in regions of minimum DFI signal are smaller than their true values. The degree of deviation depends on the difference between the measured minimum DFI and the true noiseless minimum DFI.

Consequences for experiments

Using our simulation of the minimum visibility, we can predict the minimum visibility dependent on the neutron count for a measurement. In Fig. 3.9 a) we show the trend of the minimum visibility dependent on the neutron count. Marked by the red area below the curve is the range of neutron counts shown in Fig. 3.6 b).

We can expand this view towards a dynamic range of the DFI signal by assuming a certain reference visibility V^r of the nGI setup. Using the methodology shown before, we can define a minimum $\mathrm{DFI}^{\mathrm{min}} = V^{min}/V^r$, detected by the nGI-setup dependent on the detected neutrons. For the maximum DFI, we define that a detectable DFI needs to differ at least by the standard deviation from a DFI signal of unity. Hence, we define the maximum $\mathrm{DFI}^{\mathrm{max}}$ as:

$$DFI^{\mathrm{max}} = 1 - \sigma_{\mathrm{DFI}} = 1 - \sqrt{2 * \sigma_{V^r}^2} \ . \tag{3.16}$$

Here σ_{DFI} is the standard deviation of the DFI at unity, i.e., no USANS detected, which is calculated by error propagation of the standard deviation of the reference visibility σ_{V^r}. The standard deviation of the visibility is collected again by simulating

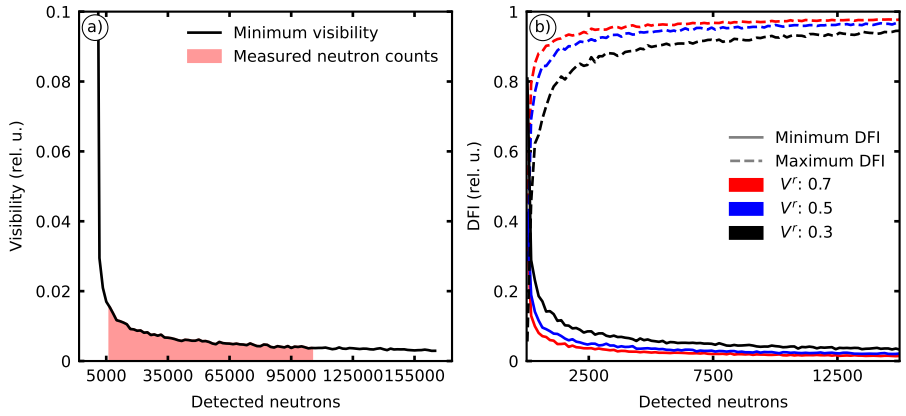

Figure 3.9.: a) Simulated minimum visibility vs. the number of neutrons counted. The red area marks the range of neutron counts shown in Fig. 3.6 b). b) Simulated dynamic range of the DFI dependent on the number of detected neutrons for the reference visibilities $V^r = 0.7$ (red), 0.5 (blue) and 0.3 (black). The dashed and solid lines denote the maximum and minimum DFI, respectively.

the variation in visibility due to Poisson noise in the data.
In Fig. 3.9 b), we present the resulting dynamic range of the DFI dependent on the neutron count for the reference visibilities $V^r = 0.7$ (red), 0.5 (blue) and 0.3 (black). The dashed and solid lines denote the maximum and minimum DFI, respectively. As expected, the dynamic range of the DFI increases with increasing neutron count and reference visibility. In the previous section, we have shown the influence of noise on the minimum visibility and DFI detectable by an nGI-setup dependent on the neutron statistics. These results help predict if strongly scattering samples' features can be differentiated. Keeping the visibility of an nGI-setup as high as possible, i.e., measurements at the design wavelength, is, from an instrumentation point of view, ideal. For quantitative results, changing the sample position rather than the wavelength (see Eq. 3.5) preserves the minimum DFI value during a scan of the correlation length. Similarly, in the case of weakly scattering samples, the correlation length and measurement time should be chosen such that the change in the DFI signal is larger than the standard deviation of the DFI signal at unity.

3.2.4. Analysis of anisotropic scattering

Due to the one-dimensional nature of the gratings, only scattering perpendicular to the grating lines is detected. Rotating the sample with respect to the orientation of the gratings allows analysis of the scattering anisotropy. The DFI signal oscillates depending on the angle ω of the sample in relation to the grating orientation. By analyzing the

shape of the oscillation, we obtain detailed information about the orientation of the microstructure. Different evaluation methods have been published, depending on the scattering strength and number of dominant scattering directions. For this thesis, we will use an approach similar to Revol et al. [96]. Eq. 3.14 links the DFI signal to the correlation function $G(\xi)$. Subsequently, it is connected via Fourier transformation to the slit-smeared differential cross-section presented in Eq. 2.34. It follows that a sample rotation by an angle ω results in slit-smearing along a new direction defined by ω. Assuming the angular dependence of a DFI signal can be modeled by a bi-gaussian scattering distribution, with a semi-major-axis width σ_M and a semi-minor-axis width σ_m, Revol et al. [96] suggest to write $DFI(\omega)$ as:

$$DFI(\omega) = \exp - \left[A + B \sin^2(\omega - \phi)\right] \tag{3.17}$$

Here A and B describe the respective isotropic and anisotropic contributions to the DFI signal. We describe A as:

$$A = \Sigma_{\text{iso}} t \tag{3.18}$$

and B as:

$$B = \Sigma_{\text{an}} t \ . \tag{3.19}$$

Σ_{iso} and Σ_{an} are the isotropic and anisotropic extinction coefficient, respectively. We note that the isotropic and anisotropic extinction coefficients are not the same as the dark field extinction coefficient shown in Eq. 3.14. Hence, we can write for the dependence of the DFI signal on ω:

$$DFI(\omega) = \exp\left(-t\left[\Sigma_{\text{iso}} + \Sigma_{\text{an}} \sin^2(\omega - \phi)\right]\right) \tag{3.20}$$

Angular dependence of the visibility

Depending on the sample size and required sample environment, a rotation of the sample may not be possible. In this case, the nGI-setup may be rotated for an anisotropy scan. However, a rotation of the nGI-setup causes a change in visibility. The influence of gravity on the neutrons, the change of the orientation of the nGI-setup and the wavelength spread of the incident neutron beam cause this effect. There are two possible contributions to the visibility decrease. One option is the drop between G_1 and G_2, which acts as a pseudo scattering of the neutron beam. Consider several

neutrons originating from one slit of G_0 passing through G_1 along the same vector. Due to gravity, the neutrons will drop a certain distance (d_g) until they reach G_2. In the case of a perfectly monochromatic neutron beam, the drop for all neutrons is the same. However, for a polychromatic neutron beam, d_g increases for slower neutrons, e.g., longer neutron wavelengths.

As an example we calculate the drop between G_1 and G_2. In case of a bandwidth of $\frac{\Delta\lambda}{\lambda} = 10\,\%$, a central wavelength of 3 Å and a distance of 60.9 cm between G_1 and G_2, d_g varies between $0.85\,\mu m \leq d_g \leq 1.27\,\mu m$. The nGI-setup can detect this spread as it is in a similar range as deviations caused by USANS. nGI does not detect this spread as long as the orientation of the grating lines is vertical. However, after a rotation of the gratings this spread degrades the visibility. In Fig. 3.10, the spread between G_1 and G_2 caused by the neutron wavelength bandwidth and the effect of grating orientation is sketched.

The second contribution is the drop of neutrons between G_0 and G_1, which can be

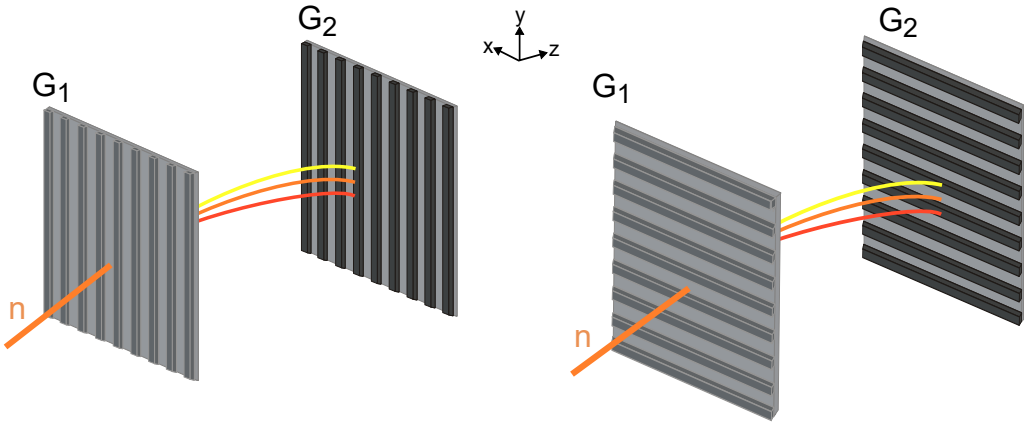

Figure 3.10.: Illustration of the difference between vertical and horizontal grating orientation in a polychromatic neutron beam due to the effect of gravity.

seen as an increase of the G_0 duty cycle. Calculating the drop between G_0 and G_1 for a bandwidth of $\frac{\Delta\lambda}{\lambda} = 10\,\%$ around a central wavelength of 3 Å and a distance of 6.89 m between G_0 and G_1 results in a d_g between 193 µm and 288 µm, which is in the same range as the magnified slit width of G_0 (342 µm) at the position of G_1. Due to the apparent increase of slit width in G_0, the visibility decreases [97]. Again this effect is only detected when grating lines are not vertical.

To illustrate the influence of the grating orientation and $\frac{\Delta\lambda}{\lambda}$ on the visibility we performed four nGI-scans at $\lambda = 3$ Å with gratings in vertical (black) and horizontal (red) orientation at $\frac{\Delta\lambda}{\lambda} = 10\,\%$ and 20 %. We present the results in Fig. 3.11. Here it is visible that for vertical orientation, the visibility drops slightly from 0.28 to 0.27 when increasing the wavelength spread. The decreased temporal coherence due to

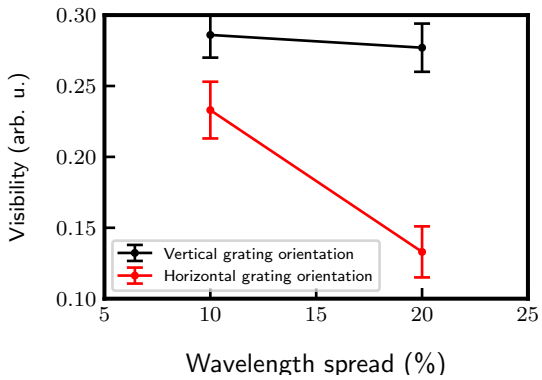

Figure 3.11.: Change in visibility when changing the wavelength spread at vertical (black) or horizontal (red) grating orientation. Due to decreased temporal coherence, the visibility drops at a higher wavelength (velocity) spread. In the case of the horizontal grating orientation, the visibility drop is more pronounced as the nGI registers the gravity-induced spread of neutrons due to a pseudo-scattering event. In vertical grating orientation, the nGI is insensitive to a gravity-induced deviation.

the increased wavelength spread causes this drop. In contrast in horizontal grating orientation the visibility at $\frac{\Delta\lambda}{\lambda} = 10\,\%$ is 0.24 and decreases to 0.14 when increasing $\frac{\Delta\lambda}{\lambda}$ to 20 %. For horizontal grating lines, the increased drop in visibility for higher neutron wavelength bandwidth demonstrates the influence of gravity on the interferometer. Consequently, rotation of the sample, not the grating, is ideal for anisotropy scans. If this is not possible due to the sample environment, one needs to account for the change in DFI dynamic range described in Sec. 3.2.3.

4 Experimental details

The following chapter will discuss the experimental components used in the neutron measurements presented in this thesis. The focus will be on the recently built neutron grating interferometer implemented at the ANTARES imaging beamline at the Heinz Maier-Leibnitz Zentrum (MLZ). We discuss the simulations used to define the setup parameters and analyze the quality of the manufactured gratings and the resulting deviations from the simulated performance. We characterize the visibility and correlation length of the setup and compare them to the previous setup. We further present the magnetic yoke used to apply magnetic fields to the samples. In addition, we give a brief overview of the symmetric nGI-setup of the BOA beamline at the Paul-Scherrer-Institut (PSI), where we performed parts of our experiments. Elements of the chapter are published in [65, 98].

4.1. The ANTARES beamline

ANTARES is an imaging beamline located at beam port 4a of the Research Neutron Source Heinz Maier-Leibnitz (FRM II) [87]. The neutron spectrum is a thermal and cold mixture with a peak at $\lambda = 1.30\,\text{Å}$. In Fig.4.1, a top-down drawing of the beamline is shown. A variation of the collimator size between 2 mm and 35.6 mm allows to adjust the geometrical resolution and, consequently, the neutron flux of the beamline. The beamline comprises three chambers. The first chamber (a) houses the various beam-shaping devices necessary for experiments. Important for this work are the neutron velocity selector (NVS) and the source grating G_0 of the neutron grating interferometry setup. The NVS is normally operated in two modes by tilting around the x-axis (See Fig. 4.1 for the used coordinate system.). The short wavelength mode with a wavelength range from 1.6 Å to 3.0 Å and a $\frac{\Delta\lambda}{\lambda} = 20\,\%$ and the long wavelength mode with a range from 3.0 Å to 6.0 Å and a $\frac{\Delta\lambda}{\lambda} = 10\,\%$. G_0 is placed directly behind the NVS. We will discuss the grating in detail in Sec. 4.2. The rest of the chamber has helium-filled flight tubes, which reduce the loss of neutrons during transit through the beamline.
The following two chambers are measurement chambers with sample stages and neutron imaging detectors. All measurements have been performed in the first measurement chamber (b). Hence only the equipment in the first measurement chamber is depicted. A beam limiter made from boron nitride reduces the cross-section of the neutron beam to the sample size, reducing the background during the measurements. The sample is placed in a magnetic yoke, mounted on a sample manipulator allowing

positioning of the sample. G_1 and G_2 are placed upstream and downstream of the sample, respectively. Again, we cover the details in Sec. 4.2. For our experiments, the neutron detector is composed of a ZnS:Cu/^{6}LiF scintillation screen, a ZEISS Milvus 2.0/100M ZF.2, two BTE front surface mirrors and a CMOS camera (Andor Neo5.5 5Mpix).

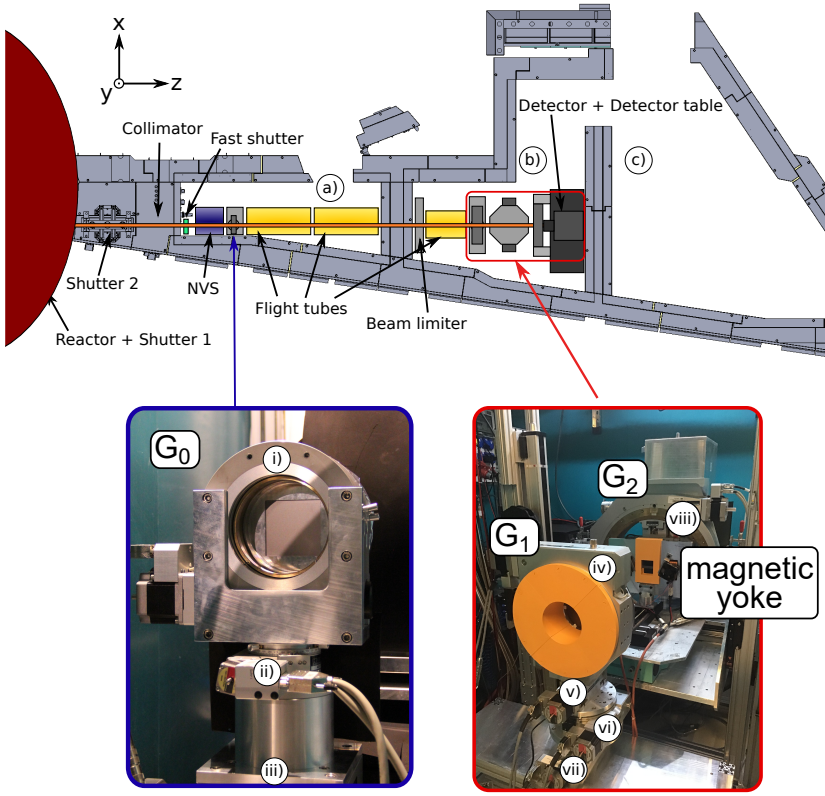

Figure 4.1.: Overview of the ANTARES beamline with the rough placement of the beam shaping devices, the grating interferometer, and the magnetic yoke used for the measurements on the electrical steel sheets. The orange line indicates the neutron path. The images show the grating interferometer setup with G_0 (blue frame) and G_1 and G_2 (red frame). Roman numerals mark their respective alignment axes. G_0: i) rotation around z-axis, ii) tilt around y-axis, iii) translation along z-axis. G_1: iv) rotation around z-axis, v) tilt around x-axis, vi) tilt around y-axis, vii) translation along z-axis. G_2: viii) rotation around z-axis

4.2. The high visibility neutron grating interferometer at ANTARES

The high visibility neutron grating interferometer at ANTARES is a Talbot-Lau interferometer operating in the third Talbot order with a maximum visibility of 0.74 over a large field of view. The following sections will discuss the considerations and parameters used to design this interferometer. Information about the interferometer and the manufacturing process of the gratings described next has been published in [65] and [98], respectively.

4.2.1. Design and simulation

In Fig. 3.2, a sketch of the nGI-setup is shown. The total length of the setup S remains similar to the previous setup (7.5 m) used at ANTARES [67], but the distance d between G_1 and G_2 has been increased from ≈ 2 cm to ≈ 61 cm. As a result of the changed geometry, the period of G_2 has been increased, allowing for a new manufacturing technique [98]. Here the absorption gratings (G_0 and G_2) etched into a silicon wafer are filled with Gd-powder. Similarly, the phase grating G_1 is also etched into a silicon wafer. The nGI-setup has been designed and optimized by implementing a wave-optical simulation based on a Fresnel-propagator [99]. The formation of fringe contrast created by the three gratings G_0, G_1 and G_2 is quantified using numerical convolution calculations [100, 101].
In Fig. 4.2 a) we present the simulated visibility V vs. the wavelength λ and the groove depth h_1 of the silicon phase grating G_1. For the simulation, we set the duty cycles (fraction of transparent area) of the gratings G_0 and G_2 to 0.3 and 0.5, respectively. At $\lambda = 4$ Å and $h_1^{\text{nom}} = 38$ µm and 114 µm pronounced maxima in V appear. The above h_1 values correspond to a π and 3π phase shift, respectively. In the following we denote the two G_1 gratings fulfilling these criteria as $G_{1,\pi}$ and $G_{1,3\pi}$. As the neutron phase shift is proportional to λ, $G_{1,3\pi}$ also offers particularly high visibility at $\lambda = 1.3$ Å and $\lambda = 6.7$ Å, where it acts as a π and 5π phase-shifting grating, respectively. At wavelengths resulting in even fractional Talbot distances, the visibility is zero regardless of h_1, as expected from theory [102, 103].

In Fig. 4.2 b), we show the visibility vs. wavelength of $G_{1,\pi}$ (blue line) and $G_{1,3\pi}$ (orange line) together with the neutron spectrum of ANTARES (green line). Here the benefit of $G_{1,3\pi}$ in the sub-2 Å range is illustrated. The visibility peak coincides with the intensity peak of the beamline. While $G_{1,3\pi}$ also performs better at wavelengths above 6 Å, the neutron intensity in this regime is minimal. In contrast, $G_{1,\pi}$ exhibits a broader primary peak at $\lambda = 4$ Å, which is useful for measurements with a broader

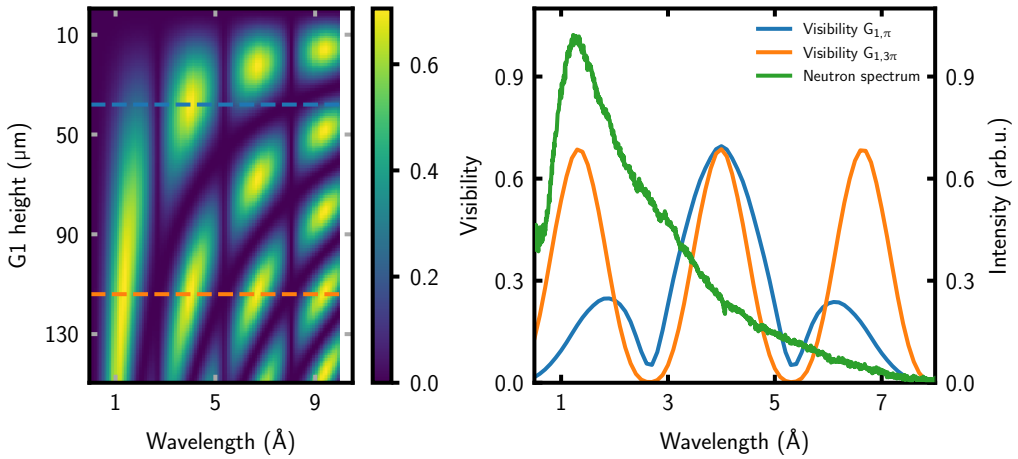

Figure 4.2.: (a) Simulation of the visibility of the new setup depending on the groove depth h_1 of the phase grating G_1 and the wavelength. (b) Spectral visibilities of π-phase-shifting (blue line) and 3π-phase-shifting (orange line) setups and the ANTARES neutron spectrum (green line). A 3π-grating allows using the setup also in the sub-2 Å regime, where the spectrum at ANTARES is most intense. The figure is already published in [65].

wavelength band. As a result of the simulation, we opted to implement the nGI-setup with the option of exchanging the phase gratings $G_{1,\pi}$ and $G_{1,3\pi}$. Due to the challenges of manufacturing the gratings, their actual parameters deviate slightly from the design parameters (See Sec. 4.2.2). The groove depth h_i and the duty cycle (DC_i) strongly influence the spectral visibility [99–101]. Therefore, the parameters used for comparison of the simulation with experimental results presented in Table 4.1 are the effective design parameters.

A decrease of the duty cycle of G_0 (DC_0) increases the coherence length of the neutrons and hence the visibility but decreases the available neutron flux. To tune the ratio between flux and visibility, we produced four G_0 gratings with $DC_0 = 0.18$, 0.28, 0.38, and 0.48.

4.2.2. Technical realization

All gratings were manufactured using silicon wafers as a substrate. Deep reactive ion etching (DRIE) was used etch the necessary rectangular groove profile. In the case of G_0 and G_2, we choose a newly developed fabrication technique of filling the grooves with Gd powder, resulting in a larger effective Gd thickness compared to the previous gratings manufactured by sideways sputtering [67]. Due to the optimized quality of the gratings, both G_0 and G_2 have an excellent binary absorption profile over the active

Parameter		Value
	Design wavelength λ	4.0 Å
	n (Fractional Talbot order)	3
	d	60.9 cm
	L	6.89 m
G_0	p_0	150 µm
	DC_0	0.18 | 0.28 | 0.38 | 0.48
	GW_0	123 µm | 108 µm | 93 µm | 78 µm
	h_0	$\approx$ 180 µm
G_1	p_1	24.4 µm
	DC_1	π) 0.51 | 3π) 0.45
	GW_1	12.44 µm | 10.98 µm
	h_1	π) 41 µm | 3π) 123 µm
G_2	p_2	13.3 µm
	DC_2	0.45
	GW_2	7.32 µm
	h_2	$\approx$ 85 µm

Table 4.1.: Effective design parameters of the new nGI-setup as realized at ANTARES. d and L designate the distance between gratings G_1 and G_2 and between G_0 and G_1, respectively. p_i, DC_i, GW_i, and h_i ($i = 0, 1, 2$) indicate the period, duty cycle, groove width, and groove depth of the gratings.

area of the gratings.

The wavelength dependent transmission for a) G_0 and b) G_2 is shown in Fig. 4.3. The transmission of a) the new G_0 gratings with $DC_0 = 0.18$ (orange), 0.28 (blue), 0.38 (green) and 0.48 (purple) is almost constant across the whole wavelength range, indicating a Gd thickness > 25 µm and a close to binary groove profile. The previous G_0 grating (gray) shows a slight increase in transmission towards short wavelengths, which fits with a Gd height of 18 µm. Evaluating the transmission of the new G_2 gratings (blue and orange) (b) yielded an effective Gd thickness of 16 µm. Additionally, the transmission curve of the new G_2 gratings indicates a close to binary (rectangular) absorption profile as the transmission first follows the well-known $\frac{1}{v}$ dependence and then levels off at long wavelengths ($\lambda > 4$ Å), which indicates a constant Gd thickness in the grooves. In contrast, the transmission of the previous G_2 (gray) continues to decrease even at $\lambda = 6$ Å, due to its more pyramidal Gd shape [67].

A detailed overview of the technical data, fabrication, and transmission experiment is presented in [98]. Due to the slightly conical shape of the neutron beam, the source grating G_0 has a reduced active area of 65 mm $\times$ 65 mm compared to the circular

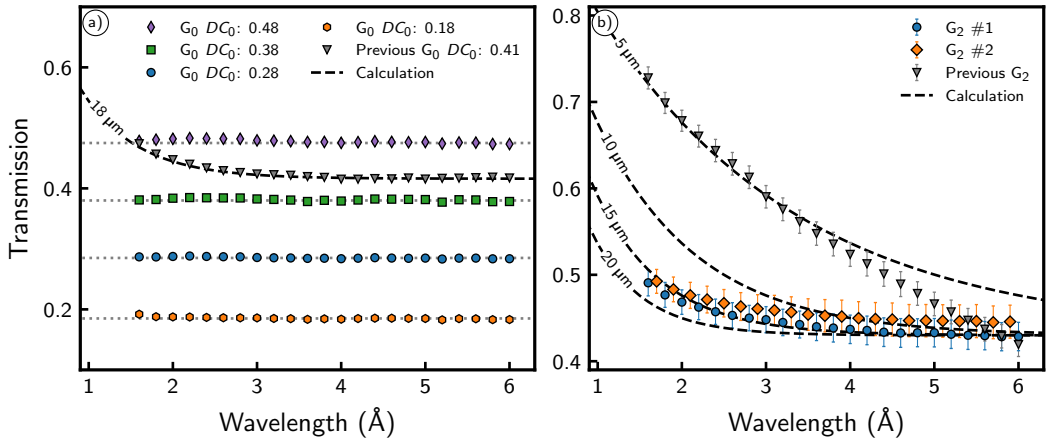

Figure 4.3.: a) Average measured transmission of G_0 gratings with $DC_0 = 0.18$ (orange), 0.28 (blue), 0.38 (green), and 0.48 (purple) compared to the previous G_0 grating (gray). The dashed line indicates the calcualted transmission of a G_0 with $DC_0 = 0.41$ and 18 µm of Gd as the absorber. b) Average measured transmission of the G_2 gratings #1 (blue) and #2 (orange) compared to the previous G_1 grating (gray). The dotted lines indicate the simulated transmission of a binary absorbing grating with $DC_2 = 0.43$. The Gd heights are denoted in the figure. The absorption characteristics of the new gratings are very close to binary gratings. In contrast, the previous gratings deviate strongly. The data presented in this figure has been published in [98].

active area of 110 mm diameter of the phase grating G_1 and the analyzer grating G_2. For interferometer alignment, the gratings have been placed in precision positioning stages depicted in Fig. 4.1. For G_0 one can i) rotate around the beam axis (z-axis), ii) adjust the effective period by tilting around the y-axis, and iii) adjust the total interferometer length S by translation along the z-axis. The positioning system of G_1 allows to iv) rotate around the beam axis, adjust the tilt along the v) x- and vi) y-axis, vii) adjust the Talbot distance d and perform the stepping scan necessary (axis not visible in Fig. 4.1). G_2 can be viii) rotated around the beam axis.
The increased distance d, compared to the previous setup, allows placing bulky sample environments such as magnets and cryostats. Alternatively, the sample can be moved between G_1 and G_2, allowing to change the correlation length without wavelength adjustment.

4.2.3. Visibility and sensitivity

While both the neutron flux and the visibility of an nGI-setup define the achievable data quality, the spectral performance of an nGI-setup can be described purely by its visibility. Regardless of neutron flux, only the quality of the gratings, the alignment,

and the G_0 duty cycle influence the visibility of the nGI-setup.
Hence, we use the visibility of an nGI-setup as its primary figure of merit. We measured the spectral visibility of the setup using the four source gratings G_0 with their different DC_0 and the phase gratings $G_{1,\pi}$ and $G_{1,3\pi}$. For the quantification of the wavelength dependence of the visibility across the accessible neutron spectrum (1.6 Å to 6 Å), we measured the spectral visibility using $G_{1,\pi}$ for all four DC_0 as well as for $G_{1,3\pi}$ and $DC_0 = 0.28$. In Table, 4.2, the details of the experiments, i.e., acquisition times, wavelength ranges, and achieved peak visibilities of the different scans, are presented. The spectral visibility (gray background) of the previous setup [67] has also been acquired for comparison. In Fig. 4.4 a) the visibility V of the new setup is shown

						Measurement	**Simulation**
DC_0	**G_1**	**Wavelength range**	**h_1 (µm)**	**Total exposure (s)**	**$\widehat{\lambda}$(Å)**	**Peak visibility**	**Peak visibility**
0.4	π	3.0 Å - 5.75 Å	43	1280	3.9	0.21	–
0.18	π	3.5 Å - 4.5 Å	41	240	4.0	0.74	0.80
0.28	π	1.6 Å - 6.0 Å	41	480	4.0	0.69	0.74
0.38	π	3.5 Å - 4.5 Å	41	240	4.0	0.63	0.66
0.48	π	3.5 Å - 4.5 Å	41	240	4.0	0.54	0.57
0.28	3π	1.6 Å - 6.0 Å	123	480	3.75	0.60	0.61

Table 4.2.: Comparison of the simulated with the measured peak visibility of the nGI-setup. For the simulations (see Sec. 4.2.1), the effective parameters listed in Table 4.1 have been used. The measured visibility of the new setup is significantly larger than the visibility of the previous setup (gray-colored background) and approaches the theoretical optimum.

for $1.6\,\text{Å} \leq \lambda \leq 6.0\,\text{Å}$ using a fixed $DC_0 = 0.28$ with the π-phase grating $G_{1,\pi}$ (blue circles) and the 3π-phase grating $G_{1,3\pi}$ (red pentagons). V was obtained by averaging the data over the central 75 % of the FoV, indicated by the dashed frame in Fig. 4.5. Compared to the previous setup (gray triangles), the new setup exhibits a significant increase in V. Due to the operation in the third, Talbot order the new setup, using $G_{1,\pi}$, which also shows two secondary peaks with good visibility. As a result of the deviation of the $G_{1,\pi}$ groove depth $h_1 = 41\,\mu\text{m}$ from the nominal design value $h_1^{\text{nom}} = 38\,\mu\text{m}$, the spectral visibility curve (See Fig. 4.2 a)) is shifted and the peak visibility at $\lambda = 1.8\,\text{Å}$ is increased to $V = 0.35$ while the peak visibility at $\lambda = 5.7\,\text{Å}$ is decreased to $V = 0.14$.

In the case of $G_{1,3\pi}$ (red markers), the visibility has its primary peak at $\lambda = 3.75\,\text{Å}$ with a value of 0.60. The secondary peaks are not in the wavelength regime accessible at ANTARES. At the wavelength extrema $\lambda = 1.6\,\text{Å}$ and 6.0 Å, V reaches 0.56 and 0.42, respectively. The peak position deviates from the simulated value $\lambda = 4.0\,\text{Å}$ (see Fig. 4.2 b)). The cause for this difference is the deviation of the effective groove

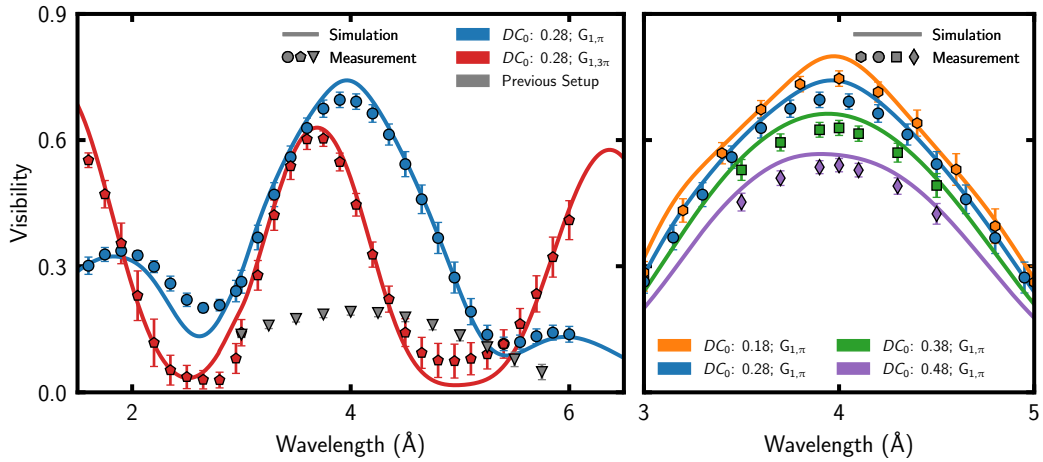

Figure 4.4.: (a) Simulated (solid lines) and measured (circle and pentagon markers) wavelength scans of the $\pi/3\pi$ phase grating configurations. We simulated the nGI-setup using the actual grating parameters from Table 4.2 and considered the polychromaticity of the beam. The performance of the previous setup is shown for comparison (triangular markers in gray). (b) Measured visibilities (hexagon, circle, square, and diamond markers) for different G_0 gratings with $DC_0 = 0.18$ (orange), 0.28 (blue), 0.38 (green) and 0.48 (purple) for $\lambda \approx 4\,\text{Å}$ using $G_{1,\pi}$ compared with their respective simulations (solid lines). Data already published in [65].

depth $h_1 = 123\,\mu\text{m}$ from the nominal groove depth $h_1^{\text{nom}} = 114\,\mu\text{m}$. Using the effective design parameters presented in Table 4.1, the simulation (solid lines in Fig. 4.4 a)) shows good agreement with the data. For the simulation, we included the wavelength distribution generated by the NVS and assumed a perfectly rectangular etched groove profile. Due to the high aspect ratio (≈ 10) of $G_{1,3\pi}$ we expect a slightly trapezoidal profile of the etched grooves, resulting in a varying DC.

In Fig. 4.4 b) the change in spectral visibility at $\lambda \approx 4\,\text{Å}$ dependent on λ is shown for different DC_0. The π-phase grating $G_{1,\pi}$ has been used as the phase grating. As expected from theory, maximum visibility of $V = 0.74$ is reached for the minimum $DC_0 = 0.18$ (orange markers) at $\lambda = 4\,\text{Å}$ and decreases towards higher DC_0. Fig. 4.5 depicts the corresponding visibility map. The standard deviation inside the framed area is 0.021 showing the homogeneity of V over the FoV. The edges of the FoV show a slight decrease of V. The reduction is caused by inhomogeneities in the analyzer grating G_2 [98] as well as a reduction of the neutron beam area with an aperture to reduce background. For the performance simulation (lines), we again considered the wavelength distribution of the NVS. Table 4.2 gives the simulated and measured peak visibilities for all measurements. They show good agreement.

Comparing the previous setup ($DC_0 = 0.4$) with the new setup ($DC_0 = 0.38$, $G_{1,\pi}$)

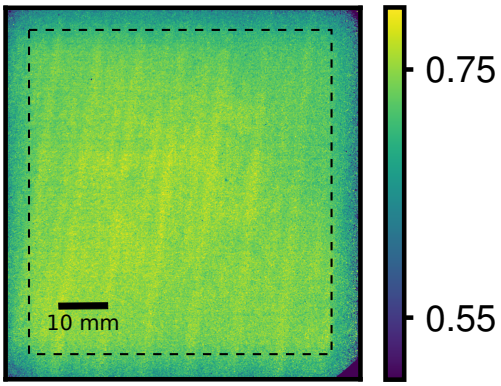

Figure 4.5.: Visibility map of the grating interferometer as determined at a wavelength $\lambda = 4\,\text{Å}$ using grating G_0 with a duty cycle $DC_0 = 0.18$. The average visibility over 75 % of the field of view is $V \simeq 0.74$. The dashed frame designates the area. The visibility degrades slightly towards the boundary of the FoV because an aperture limits the beam size to reduce the background. The figure has already been published in [65].

shows a significantly increased peak visibility for the new setup $V = 0.63$ compared to the old setup $V = 0.21$. The increased peak visibility underlines the outstanding performance of the new absorber gratings and the whole setup.

A second important metric for an nGI-setup is the accessible correlation length range. Similar to the q-range of a SANS experiment, the correlation length ξ range defines the analyzable structure sizes. Placing the sample in the space ($d = 60.9\,\text{cm}$) between G_1 and G_2 allows for a wide variation of the correlation length ξ_{GI} (i.e., Eq. 3.5) As noted previously, this enables the quantitative analysis of the material or magnetic microstructure within a sample [67, 76, 79]. Changing the position L_{sd} of the sample to adjust ξ has the advantage that the nGI-setup operates constantly at peak visibility and provides good signal-to-noise-ratio (SNR). A trade-off in this mode is that the sample-to-detector-distance (SDD) and spatial resolution changes. Using λ to change ξ reverses the advantages and disadvantages. A further consideration is the minimum and maximum DFI signal accessible due to Poisson noise (see Sec. 3.2.3). A change in wavelength also changes the scattering strength, which may result in exceeding the dynamic range of the DFI.

In Fig. 4.6 the accessible correlation length ranges of the new setup operating at $\lambda = 1.6\,\text{Å}$ (orange), $4.0\,\text{Å}$ (red) and $6.0\,\text{Å}$ (dark red) are compared with the previous setup (black) and three interferometry setups (conventional Talbot-Lau (cTL) (gray), symmetric Talbot Lau (sTL) (green) and Single Grating (SG) (blue)) used at the PSI [13]. For the new setup a minimum and maximum $L_{sd} = 2\,\text{cm}$ and $55\,\text{cm}$ was used. We calculated the correlation length range of the previous setup by assuming an accessible wavelength range of $1.6\,\text{Å}$ to $6.0\,\text{Å}$, a Talbot distance $d = 19.9\,\text{mm}$ and

$p_2 = 4\,\mu m$. The correlation length data for the PSI setup has been gathered from [13]. For all setups a minimum $L_{sd} = 2\,cm$ has been used.

The comparison shows an increase in the accessible correlation length range when

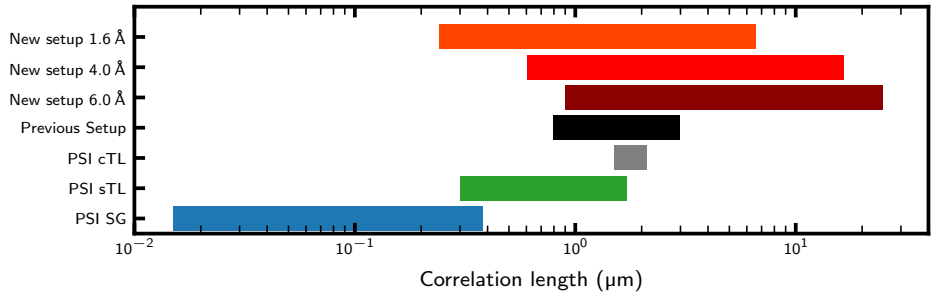

Figure 4.6.: Comparison of the correlation length ranges achieved by the new nGI-setup at $\lambda = 1.6\,Å$ (orange), $4.0\,Å$ (red) and $6.0\,Å$ (dark red) with the previous setup (black) and exemplary with three setups (cTL (gray), sTL (green) and SG (blue)) used at the PSI [13].

developing new nGI-setups. Our previous setup [67] and the PSI cTL [62],[63] are comparatively old setups featuring a highly asymmetric geometry and low accessible correlation length ranges. The more recent setups show increased correlation length ranges spanning one to two orders of magnitude, which allows for more quantitative analysis. Of note is the tailoring of newer setups to different correlation length regimes. While our new setup has been optimized towards high correlation lengths to analyze the distribution of magnetic domains in electrical steel sheets, the PSI SG setup has instead been optimized towards the nanometer regime, acting more as a spatially resolved SANS instrument.

4.2.4. Magnetic yoke

We investigate the change of the distribution of magnetic domains in non-grain oriented electrical steel (NGOES) sheets by combining the nGI-setup with a magnetic yoke. The yoke has been designed to operate in conjunction with the nGI-setup (shown in Fig. 4.7 a)) It has a central cutout of $50\,mm \times 65\,mm$. The magnetic core of the yoke (iii) is sketched in Fig. 4.7 b). The distance between the two magnetic poles of the yoke is 50 mm, and the poles have a width of 60 mm. Sixteen electrical steel sheets comprise the magnetic core, each with a thickness of 0.5 mm. The stack of electrical steel sheets divides into three substacks. The two outer substacks consist of 7 sheets, while the inner stack comprises the two central sheets. The central sheets are recessed, with a distance of 110 mm between the recessed sheets. For the measurements, the

two outer substacks clamp the sample. A sketch of the construction of the magnetic core close to the magnetic poles is shown in Fig. 4.7 c).

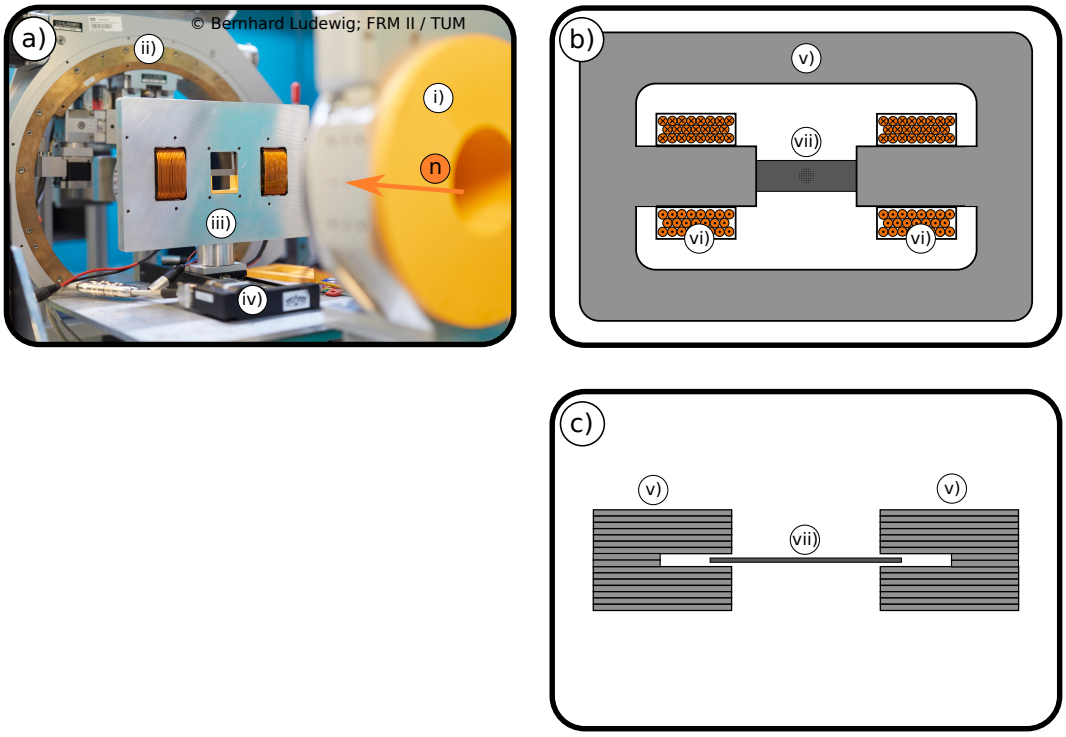

Figure 4.7.: a) nGI-setup combined with the magnetic yoke at the ANTARES beamline. i) G_1 stage, ii) G_2 stage, iii) magnetic yoke, and iv) translation stage of the magnetic yoke along the beam direction. (©Bernhard Ludewig; FRM II / TUM) b) schematic of the magnetic core of the magnetic yoke. v) magnetic core, vi) magnetic coils, and vii) specimen. c) Sketch of the stack of electrical steel sheets comprising the magnetic core at the magnetic poles with an unclamped sample.

4.3. The symmetric neutron grating interferometer at PSI

Parts of the measurements included in this thesis were conducted at the BOA beamline [104] of the Swiss Spallation Neutron Source (SINQ) at the Paul-Scherrer-Institute using a symmetric Talbot-Lau setup (sTL) [13]. The parameters of this setup are given in Table 4.3. BOA is situated at the end of a polarized cold neutron guide, delivering a spectrum with a peak wavelength of $\lambda = 3.8\,\text{Å}$. For the measurements, we used an L/D of 900. In contrast to the measurements performed at the ANTARES beamline, we used the full polychromatic beam at BOA. As a result, the correlation length is not well defined in these measurements. Hence only a qualitative comparison of the results is possible. The setup delivered a polychromatic visibility of $V = 0.3$.

	Parameter	Value
	Design wavelength λ	$\approx 3.8\,\text{Å}$
	n (Fractional Talbot order)	1
	d	44.64 cm
	L	44.64 cm
G_0	p_0	26 µm
	DC_0	0.26
	h_0	16 µm
G_1	p_1	25 µm
	DC_1	0.5
	h_1	43.28 µm
G_2	p_2	26 µm
	DC_2	0.37
	h_2	$\approx 16\,\mu\text{m}$

Table 4.3.: Effective design parameters of the symmetric nGI-setup as realized at BOA. d and L designate the distance between gratings G_1 and G_2 and between G_0 and G_1, respectively. p_i, DC_i, and h_i ($i = 0, 1, 2$) indicate the period, duty cycle, and groove depth of the gratings, respectively. Due to a different manufacturing process, the groove depth of G_0 and G_2 denote the nominal Gd height.

Due to the sample environment, the usable FoV of the setup was 60 mm × 60 mm. The gratings of the setup had some damages, drastically reducing the signal quality in certain areas (see Fig. 5.16). For magnetizing the sample, the same magnetic yoke as described in Sec. 4.2.4 was used. An image of the sTL-setup, including the magnetic yoke at BOA, is shown in Fig. 4.8.

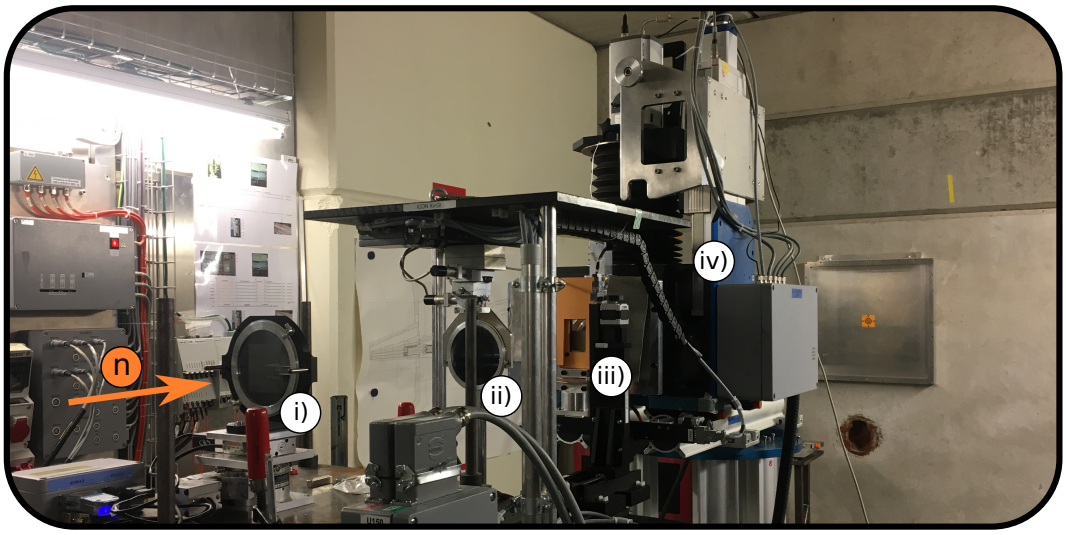

Figure 4.8.: sTL-setup combined with the magnetic yoke at the BOA beamline. i) G_0 grating, ii) G_1 grating, iii) magnetic yoke, and iv) detector system. Note that the magnetic yoke and the detector system hide G_2.

4.4. Sample preparation and characterization

The samples used in this thesis are manufactured from M330-35A grade NGOES and prepared by the Chair of Metal Forming and Casting of the Technical University of Munich. A detailed characterization of this material has been published in [30, 105], from which we will reproduce the values. Table. 4.4 gives the chemical composition.

The average grain size is 71 µm along the rolling direction, 78 µm vertical to the

Element	Fe	C	Si	Mn	P	S	Cr	Al
(wt%)	97.00	0.02	2.42	0.16	0.02	0.01	0.03	0.34

Table 4.4.: Chemical composition of the electrical steel sheets.

rolling direction and 66 µm through the sheet thickness. The thickness of the electrical steel sheet is 350 µm. This thesis will consider two sample shapes, S1 and S2. S1 has a geometry ($L \times W \times T$) of 60 mm × 10 mm × 350 µm and S2 a geometry of 60 mm × 40 mm × 350 µm. The length $L = 60$ mm of the samples is imposed by the magnetic yoke described in Sec. 4.2.4. We choose the width W according to the planned embossing. The thickness $T = 350$ µm has been chosen to minimize the saturation of the DFI signal due to scattering. During the thesis, we used two distinct embossing strategies. In Fig. 4.9, we sketch both strategies.

The first embossing strategy shown in b) closely resembles the blanking process

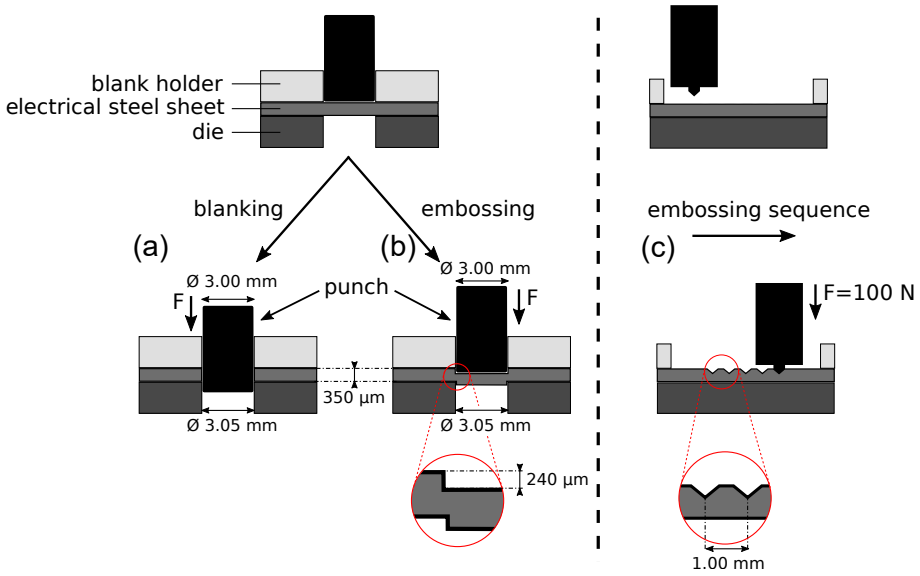

Figure 4.9.: Side view of a sketch of the manufacturing process of both a) a blanked (Sample E) and b) an embossed (Sample C) electrical steel sheet.

(shown in a)) used to generate a cutout in the material. The sample is placed between a die with a 3.05 mm diameter cutout and a blank holder. The punch is then pressed nominally 200 µm deep into the material, generating a single relatively large embossing. For a reproducible placement of the embossing, we initially cut the samples into a geometry of 90 mm × 15 mm × 350 µm. This enabled to simultaneously emboss the sample and blank locating holes, used to later align the samples during the erosion towards the final geometry. We chose the erosion process, which promised to deteriorate the magnetic properties the least [30].
A Schuler stamping press CSP 100 with ServoDirect Technology was used for the embossing and blanking process. Due to inaccuracies in the final depth of the punch, the exact geometry of the embossing has been recovered using a Keyence VK-X100 Series Shape Measurement Laser Microscope. This embossing strategy has been used for sample A-D. The final embossing depth, as well as the used punch type, are reproduced in Table 4.5.

In Fig. 4.9 c), we display the second embossing strategy, which differs by switching to a sequential embossing, introducing multiple small embossing points in the sample. This process reduces the overall deformation of the electrical steel sheets and allows the creation of arbitrary embossing patterns consisting of individual embossing points. For the embossing, a small four-sided pyramidal tip with a quadratic base (base length = 1 mm) and a tip angle of 136.5° is used. Here the final geometry of the samples was eroded before the embossing process. The electrical steel sheets were placed between a flat die and a blank holder. We pressed the punch according to the embossing pattern

Sample name	Sample dimensions	Embossing pattern	Embossing depth [µm]
Reference R1	60 mm × 10 mm × 350 µm	none	none
A	60 mm × 10 mm × 350 µm	sphere with diameter $D_s = 2$ mm	≈ 238
B	60 mm × 10 mm × 350 µm	rounded tip with cone angle 110°, $D_t = 3$ mm	≈ 306
C	60 mm × 10 mm × 350 µm	cylindrical tip, $D_f = 3$ mm	≈ 240
D	60 mm × 10 mm × 350 µm	cylindrical tip, $D_c = 3$ mm	cutout

Table 4.5.: Geometry of the samples and parameters of the punches used for embossing the samples. In Fig. 5.3, the shape of the punches used is shown. The embossing depth has been measured for each sample as explained in Sec. 4.4.

into the sample with force $F = 100$ N using a ZwickRoell ProLine universal testing machine for the samples considered in this thesis. In Table 4.6, the samples embossed by this strategy (E-H) and their respective embossing patterns and embossing point spacing are reproduced.

Sample name	Sample dimensions	Embossing pattern	Pattern spacing (mm)
E	60 mm × 10 mm × 350 µm	circle	0.5
Reference R2	60 mm × 40 mm × 350 µm	none	none
F	60 mm × 40 mm × 350 µm	rectangle	1
G	60 mm × 40 mm × 350 µm	staggered rectangle	1
H	10 mm × 40 mm × 350 µm	two rectangles	1

Table 4.6.: Geometry of the samples and parameters of the embossing pattern generated by the sequential embossing strategy. The shape of the embossing patterns of sample E can be seen in Fig. 5.4 c), while the embossing patterns of samples F-H are shown in Fig. 5.16 b)-d), respectively.

5 Magnetic properties of electrical steel with residual stress

5.1. Information contained in the DFI signal

While neutron grating interferometry-based analysis of electrical steel has become more widespread in recent years [78, 106–110], embossed non-grain-oriented electrical steel (NGOES) has been analyzed primarily as part of the same DFG project as this thesis [65, 70, 111–114]. In the following section, we will give an overview of the quantities nGI measures when analyzing embossed NGOES and their importance for data analysis in the following sections. The theory section notes that nGI measures scattering off material and magnetic inhomogeneities in the micrometer range. Due to the embossing process, the grain structure of NGOES and the distribution of its magnetic domains changes. Furthermore, discontinuities in the material volume may occur depending on the embossing process, which may also cause scattering. In the following two sections, we will explore the influence of nuclear scattering in NGOES as well as the deformation of NGOES on the DFI signal.

5.1.1. Scattering off the nuclear microstructure

The grain structure of NGOES itself provides a microstructure off which USANS may occur. In the case of the used material, the mean grain diameter is $\approx 70\,\mu m$. This structure size is significantly larger than the maximum correlation length $\xi = 24.8\,\mu m$ accessible with our nGI setup and other setups. Hence, primarily magnetic scattering causes the signal detected by nGI. In Fig. 5.1, this assertion is substantiated by measuring the DFI signal of an NGOES at different applied magnetic fields H_{app} and correlation lengths ξ. Regardless of ξ the DFI signal rises with increasing H_{app}, reaching unity for $H_{app} > 100\,kA\,m^{-1}$. The signal trend towards unity shows that no detectable USANS is present when the samples are close to magnetic saturation. In case of significant material scattering, even close to magnetic saturation, the DFI should be below unity. Subsequently, we attribute any scattering signal detected to magnetic scattering.

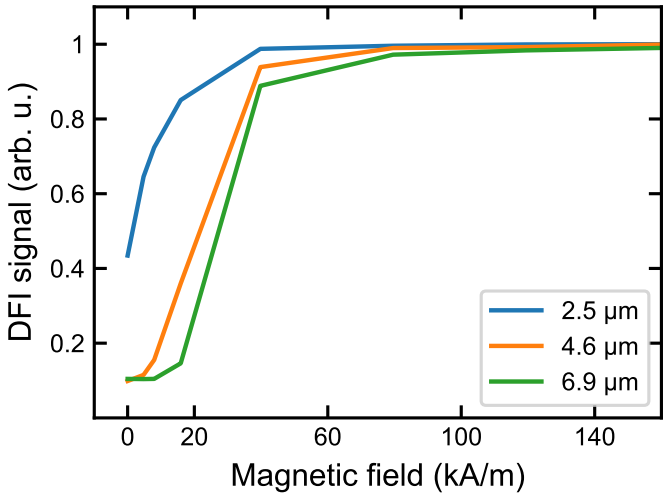

Figure 5.1.: DFI signal of an NGOES sheet dependent on the applied magnetic field (H_{app}) at correlation lengths ranging from 2.5 µm to 6.9 µm. At high H_{app}, the DFI signal trends towards unity, indicating no detectable scattering.

5.1.2. Scattering due to material deformation

In the previous section, we have shown that the grain structure of non-embossed NGOES does not contribute to the DFI signal. However, embossing deforms the sample. This deformation may be a source for USANS due to scattering on the created edges. We embossed two samples (Emb1 and Emb2) and annealed one (Emb2) to investigate a possible deformation effect on the magnetic properties and the DFI signal. Similarly, as a reference, we measured two virgin samples (R3 and R4), one of which was annealed (R4). Table 5.1 shows the material states of the four samples.

Fig. 4.9 b) shows a sketch of the embossing process of the samples. As shown,

Sample	R3	R4	Emb1	Emb2
Embossed	No	No	Yes	Yes
Annealed	No	Yes	No	Yes

Table 5.1.: Material states of the reference (R3 and R4) and embossed (Emb1 and Emb2) samples used to investigate deformation as a cause of scattering.

we performed the embossing using a flat punch with a diameter of 3 mm, and the embossing depth was set to 50 µm. We annealed the sample to remove residual stress by keeping the samples at a temperature of $\approx 800\,^{\circ}\mathrm{C}$ for an hour and a slow cooling toward room temperature.

In Fig. 5.2 the DFI signal of sample a) Emb1, b) Emb2, c) R3 and d) R4 at an

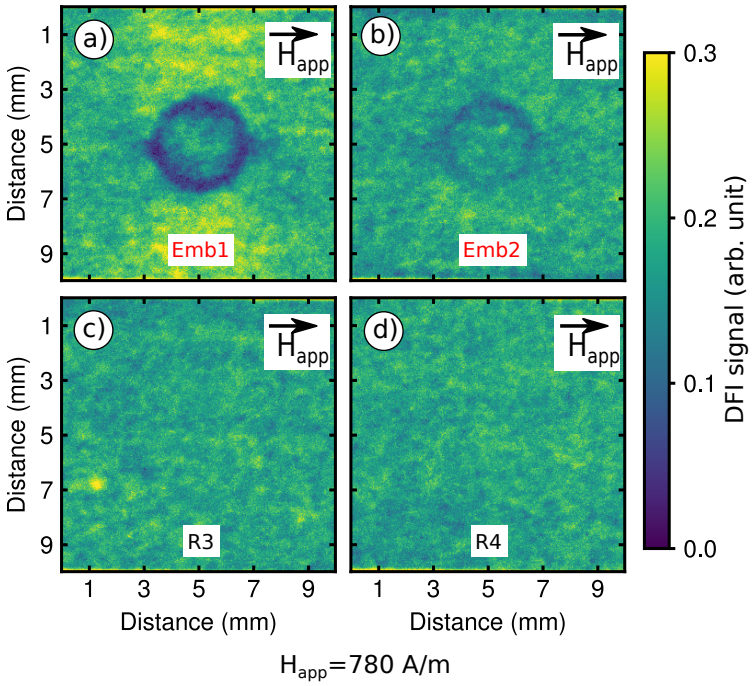

Figure 5.2.: DFI signal of sample a) Emb1, b) Emb2, c) R3 and d) R4 at an applied magnetic field $H_{app} = 780\,\mathrm{A\,m^{-1}}$. a) shows the guidance of the magnetic flux due to residual stress, which vanishes in b) due to the annealing. In the two reference samples, the annealing does not influence the DFI signal, indicating an insignificant influence of annealing on the measured signal.

applied magnetic field $H_{app} = 780\,\mathrm{A\,m^{-1}}$ are shown. Emb1 shows, as expected, both a decrease in the DFI signal in the embossed area and an increase in the DFI signal above and below the embossing, indicating the guidance of the magnetic flux by the embossing. In contrast, Emb2 shows no increase above or below the embossing, while the embossed area shows a significantly reduced decrease in the DFI signal. Both R3 and R4 show a similar homogeneous DFI signal, indicating that the primary effect causing the decrease of the DFI signal and, correspondingly, the magnetic guidance of the magnetic flux is residual stress, as the deformation of the sample is not affected by annealing. The slight decrease of the DFI signal in the embossed area of Emb2 is most likely the remaining residual stress after annealing and the resulting change in the magnetic properties.

While embossing also influences grain sizes and introduces defects in the atomic lattice [115], we have already shown that our measurements do not detect scattering caused by the grains of the material. Similarly, nGI is not sensitive to scattering off the atomic lattice, hence changes in the lattice do not directly influence the scattering signal.

As both reference samples show the same signal, we can assume that the annealing process has not changed the grain structure and the distribution of magnetic domains.

5.2. Embossing electrical steel - Guiding the magnetic flux

In the previous section, we have established that primarily residual stress causes the change in the DFI signal, which locally changes the magnetic permeability. This change in local permeability allows us to guide the magnetic flux away from areas influenced by residual stress, similar to cutouts in the ES. In the following, we will analyze different embossing strategies concerning their ability to guide magnetic flux and the deformation of the ES. We looked at the embossed samples A to E and the reference R1 for this. Parts of the results presented in this section have been published in [65] and [114].

5.2.1. Experimental procedure

For the evaluation of the guidance of the magnetic flux provided by residual stress in NGOES, we applied a H_{app} from 16 A m^{-1} to 11 200 A m^{-1} and measured the resulting DFI signal. We chose the rolling direction of the samples, the direction of H_{app}, and the sensitivity direction of the nGI-setup to be horizontal. Using different correlation lengths, we performed the measurements in two distinct campaigns at the ANTARES beamline. Samples A to D as well as R1 were measured at a correlation length $\xi_1 = 1.865\,\mu m$, which corresponds to a sample to G_2 distance of 62 mm for wavelength $\lambda = 4\,Å$. Sample E and R1 were measured at $\xi_2 = 0.84\,\mu m$ also with $\lambda = 4\,Å$, but at a sample to G_2 distance of 28 mm. Similarly, due to a change in the magnetic coils of the magnetic yoke, the applied magnetic fields H_{app} vary slightly between the measurement campaigns. The other parameters were the same for both measurement campaigns. We performed an nGI-scan with ten equidistant phase steps for each magnetic field. At each phase step, three images with an exposure time $t = 10\,s$ were taken, resulting in a total exposure time of 300 s. We used one of the standard nGI-setup detector systems at ANTARES, described in Sec. 3.2.3 with a field of view of 71 mm $\times$ 76 mm and an effective pixel size of 33 µm $\times$ 33 µm. After processing the raw data and generating the DFI maps for all samples, the DFI maps of the embossed samples were divided pixel by pixel with the DFI map of the reference sample R1. Hence, a signal value $S = 1$ denotes no change in scattering.

5.2.2. Results

In Fig. 5.3 a) the normalized DFI maps of the embossed samples A, B, and C in a magnetic field $H_{\text{app}} = 3330\,\text{A}\,\text{m}^{-1}$ are shown. The three different punch types generate different patterns, but all three types reduce S below unity, indicating increased scattering. Fig. 4.9 b) shows the embossing process used for the three samples. Fig 5.3 b) shows the trend of the radially averaged signal $S_{ave}(r)$ of sample A-C from the center of the embossing, acquired at $H_{\text{app}} = 780\,\text{A}\,\text{m}^{-1}$ (solid lines) and $H_{\text{app}} = 11\,200\,\text{A}\,\text{m}^{-1}$ (dashed lines). For the measurements at $H_{app} = 780\,\text{A}\,\text{m}^{-1}$, sample A shows an approximately linear increase of $S_{\text{ave}} = 0.13$ at $r = 0\,\text{mm}$ to unity at $r = 3\,\text{mm}$. At $H_{\text{app}} = 780\,\text{A}\,\text{m}^{-1}$, S_{ave} of sample B has a value of 0.26 at $r = 0\,\text{mm}$. However, the signal increases faster towards unity, reaching $S_{\text{ave}} = 1$ at $r = 2\,\text{mm}$. The trend of S_{ave} is not linear as in sample A but shows a dip at $r = 1.5\,\text{mm}$. In contrast to samples A and B the minimum S_{ave} of sample C is not at $r = 0\,\text{mm}$ but at $r = 1.45\,\text{mm}$ with a value $S_{\text{ave}} = 0.26$. At radii $r > 1.45\,\text{mm}$ S_{ave} increases towards unity at $r = 2.2\,\text{mm}$. For $r < 1.45\,\text{mm}$, we measure a slight increase of S_{ave}, indicating that magnetic flux has passed the residual stress barrier induced by embossing.
Increasing H_{app} to $11\,200\,\text{A}\,\text{m}^{-1}$ significantly increases S_{ave} in the samples. In sample A S_{ave} increases to 0.68 at $r = 0\,\text{mm}$, while the radius it reaches unity is constant at $r = 3\,\text{mm}$. The dip in sample B at $H_{\text{app}} = 780\,\text{A}\,\text{m}^{-1}$ vanishes at increased H_{app}, but for r in the range 0.75 mm to 1.5 mm S_{ave} is constant. Similar to sample A S_{ave} reaches unity at the same radius ($r = 3\,\text{mm}$) as with $H_{\text{app}} = 780\,\text{A}\,\text{m}^{-1}$. Sample C also shows an increase of S_{ave}, but less pronounced than in the other two samples.

In Fig. 5.4 a), the normalized DFI maps of the embossed samples C-E are shown. We blanked sample D as displayed in Fig. 4.9 a), while sample E was sequentially embossed as shown in Fig. 4.9 c). In b), the embossing patterns and the expected magnetic flux are shown. FB denotes the embossed/blanked areas, and FC represents increased magnetic flux areas. We observe an increase in signal above unity in the FC area for all samples. In the blanked sample D, the signal increases to 2.3 while the signal in samples C and E rises to 1.2 and 1.1, respectively. The white area masks the signal in the FB area of sample D, as the normalization of R1 to sample D does not make sense in the blanked area. For sample C, the signal in FB decreases to a mean of 0.6 in the center of the embossing, while in sample E, the signal in FB decreases to 0.5.
Fig. 5.4 c) shows the trend of the radially averaged signal $S_{ave}(r)$ of sample C-E from the center of the embossing, acquired at $H_{\text{app}} = 813\,\text{A}\,\text{m}^{-1}$ (solid lines) and $H_{\text{app}} = 11\,200\,\text{A}\,\text{m}^{-1}$ (dashed lines). Similar to the results shown in Fig. S_{ave} of sample C is not at $r = 0\,\text{mm}$ but at $r = 1.45\,\text{mm}$ with a value $S_{\text{ave}} = 0.48$. At radii $r > 1.45\,\text{mm}$ S_{ave} increases towards unity at $r = 2.2\,\text{mm}$. For $r < 1.45\,\text{mm}$ S_{ave}

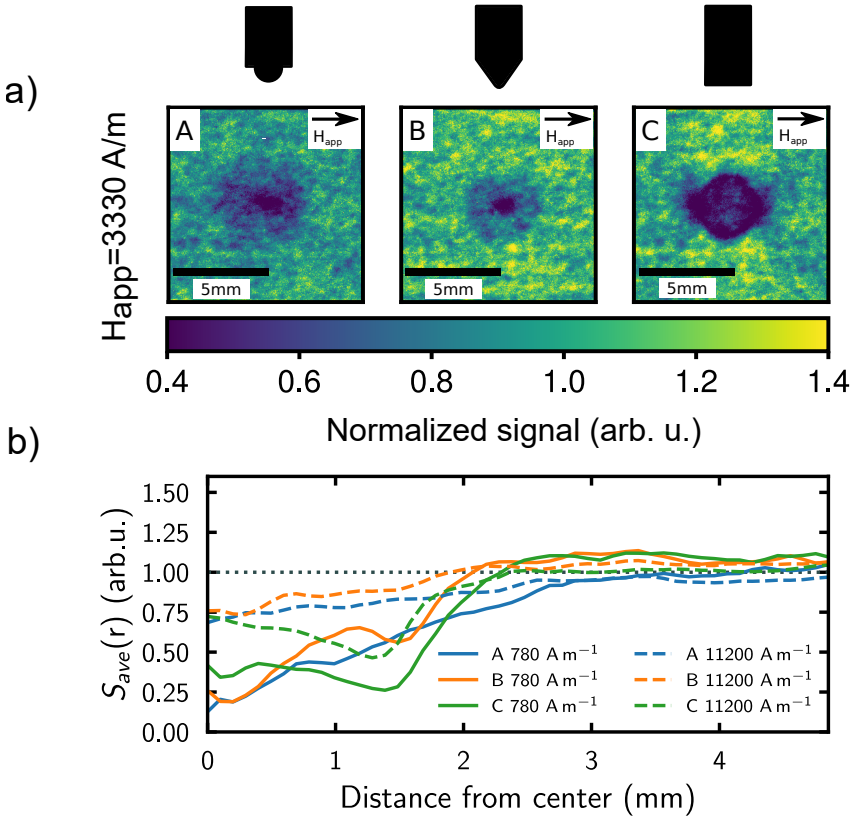

Figure 5.3.: Analysis of the influence of embossing on the scattering contrast. (a) Normalized DFI-signal of samples A, B, and C in an applied magnetic field $H_{app} = 3330\,\mathrm{A\,m^{-1}}$. The data is normalized using the reference sample also exposed to H_{app}. A signal smaller than $S = 1$ indicates more scattering in the embossed sample than in the non-embossed reference. (b) Normalized signal $S_{ave}(r)$ as obtained by radially averaging the images of samples A (blue), B (orange), and C (green) with $H_{app} = 780\,\mathrm{A\,m^{-1}}$ (solid line) and $11\,200\,\mathrm{A\,m^{-1}}$ (dashed line). The figure has been published similarly in [65].

increases to 0.7, indicating that magnetic flux has passed the residual stress barrier induced by embossing. The blanked sample shows the minimum signal $S_{ave} = 0.8$ at $r = 1.6\,\mathrm{mm}$, while sharply increasing for smaller radii. Here, the signal above unity is an artifact of the normalization process and does not indicate a magnetic flux. For $r > 1.6\,\mathrm{mm}$ the signal increases slowly towards $S_{ave} = 1.1$. Sample E shows nearly constant $S_{ave} = 0.5$ for radii $r < 1.75\,\mathrm{mm}$. At larger radii, the signal increases towards unity.

Increasing H_{app} to $11\,200\,\mathrm{A\,m^{-1}}$ increases S_{ave} for samples C and E in the embossed area significantly. In contrast to $H_{app} = 813\,\mathrm{A\,m^{-1}}$ sample C shows a lower S_{ave} than sample E for radii $r < 1.75\,\mathrm{mm}$, with a minimum of 0.75. Sample E has a minimum

S_{ave} of 0.85, indicating low guidance of the magnetic flux. In contrast, the minimum of sample D is similar to the minimum at $H_{app} = 813\,\mathrm{A\,m^{-1}}$.

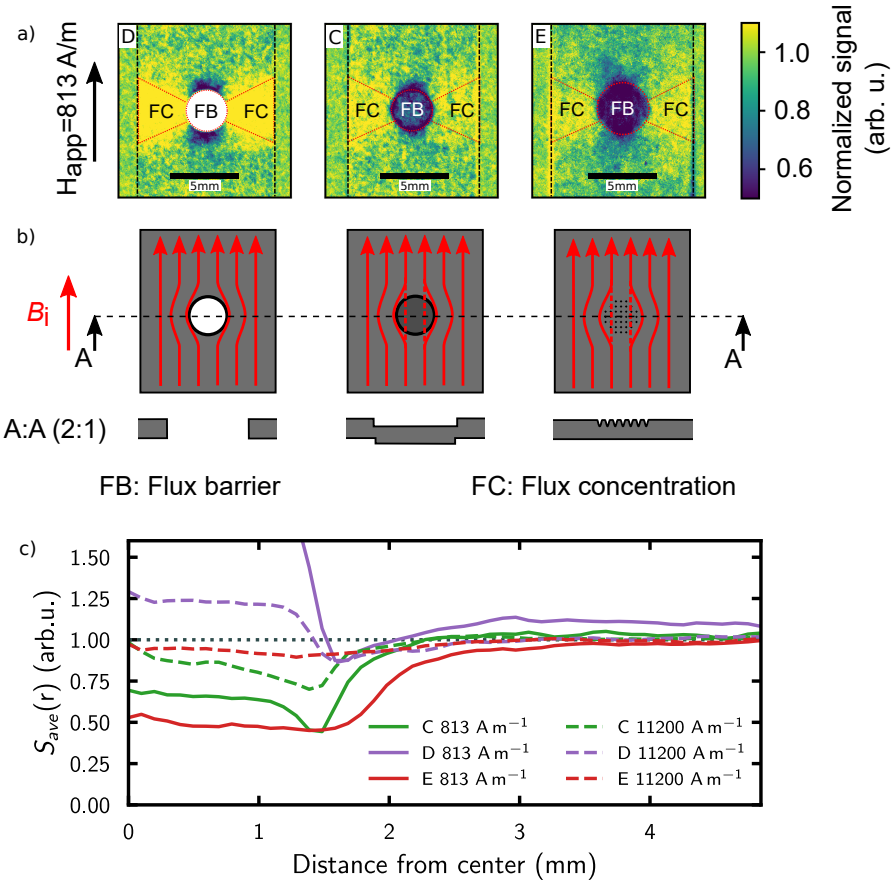

Figure 5.4.: Comparison of the guidance of the magnetic flux using different embossing strategies. (a) Normalized DFI-signal of samples C, D, and E in an applied magnetic field $H_{app} = 780\,\mathrm{A\,m^{-1}}$. The data is normalized using the reference sample also exposed to H_{app}. A signal smaller than $S = 1$ indicates more scattering in the embossed sample than in the non-embossed reference, hence less magnetic flux. (b) Sketches of the expected magnetic flux inside samples C-E. c) Normalized signal $S_{ave}(r)$ obtained by radially averaging the images of samples C (green), D (purple), and E (red) with $H_{app} = 813\,\mathrm{A\,m^{-1}}$ (solid line) and $11\,200\,\mathrm{A\,m^{-1}}$ (dashed line). Parts of the data presented in this figure have been published in [114].

5.2.3. Discussion

We attribute the differences in signal observed in Fig. 5.3 to the differences in punch shape and the embossing process. Sample A is deformed more gradually due to the

shape of the spherical punch. In contrast, the conical punch of sample B causes stronger deformation, which leads to a secondary residual stress area in the range 0.75 mm to 1.5 mm due to the blank holder and die. The signal caused by the flat embossing in sample C is not perfectly circular. The interplay between the circular embossing, resulting residual stress, and the unidirectional magnetization direction causes elongation along the applied magnetic field direction. The range of influence of residual stress on the signal is largely independent of the applied magnetic field. This independence makes sense as the magnetic field does not influence the range of residual stress. Samples A to C show an increase of the normalized signal S at $H_{\mathrm{app}} = 11\,200\,\mathrm{A\,m^{-1}}$, indicating that the effect of the residual stress, reduction of permeability, is less significant at higher magnetization states. We previously observed similar effects using global magnetic measurements [30, 111], limiting residual stress as a flux barrier for high H_{app}. However, such high H_{app} is normally not used in electric drives due to the low permeability of electrical steel at these applied magnetic fields [111].

The signals in Fig. 5.4 show that embossing (Sample C and E) also enables the guidance of magnetic flux in electrical steel. However, the effect of embossing is smaller than for blanking, as can be seen by the higher signal S in the FC area of sample D. This fits our expectations. While the embossing reduces the maximum magnetic permeability μ significantly compared to $\mu_{\mathrm{r}} \approx 6000$ in our stress-free electrical steel samples [70, 113], the permeability will remain significantly above $\mu_{\mathrm{r}} \approx 1$ as encountered in air.

While the effect of the sequential embossing (E) is a small H_{app} roughly equal to the single embossing (C), the deformation of the sample is also significantly reduced. However, at higher H_{app}, the guidance of the magnetic flux of the single embossing is larger than the sequential embossing. The construction of the magnetic core of an electric drive comprised of stacked electrical steel sheets requires minimum deformation of the electrical steel. Gaps between the stacked electrical steel sheets decrease the power density of the electric drive [116]. We note that there is a difference in normalized signal in the embossing area between sample C in Fig. 5.3 and Fig. 5.4 (0.4 to 0.6). The different accessed correlation lengths cause this difference. As the change in scattering signal due to embossing is not trivial, a change in correlation length will influence the ratio between the DFI in the embossed sample and the DFI in the reference sample.

5.2.4. Conclusion

In the previous section, we demonstrated the possibility of using residual stress to guide magnetic flux in electrical steel. The results on the macroscopically embossed samples (A-C) show that to restrict the range of the residual stress, a sharp deformation edge

caused by the flat embossing in sample C is preferred compared to a more gradual deformation in A and B. However, a strategy of multiple small embossing points, as in sample D, is chosen for practical applications. Here guidance of the magnetic flux similar to flat embossing can be achieved while minimizing deformation. A further consideration is the possibility of freely defining the pattern and force of the embossing points, enabling the creation of flux barriers that are primarily effective along one direction while minimally impeding the magnetic flux in the perpendicular orientation.

5.3. Connection of dark field contrast and the size of magnetic domains in electrical steel

Local changes in the material properties due to residual stress cause a change in the distribution of magnetic domains [117]. Due to the residual stress, the movement of magnetic domain walls is pinned [115], and the preferred magnetic domain size tends to decrease compared to a stress-free material [118]. Applying an external magnetic field causes the growth of magnetic domains aligned favorably to the magnetic field. nGI tracks this variation in the size of magnetic domains caused by stress and applied magnetic field.

5.3.1. Models to describe the interaction of neutrons with magnetic domains

For ferromagnetic single crystals and also grain-oriented electrical steel (GOES), the description and measurement of the distribution of magnetic domains using nGI is comparatively simple [118, 119], as the magentic domains are large compared to the spatial resolution. In addition, the measurement of local surface domains allows us to conclude the distribution of internal domains due to the homogeneous nature of the considered material. In contrast, the surface domains visible in polycrystalline materials do not simply correspond to the internal domains, as the internal grain boundaries are typically unknown. As a result, describing the distribution of internal domains in polycrystalline materials using surface measurements is, in many cases, impossible. Most techniques able to measure magnetic properties in the bulk of a polycrystalline sample can only assess global magnetic properties [3, 8].
Here neutron depolarization imaging and nGI allow us to map these properties [11, 119]. While neutron depolarization imaging is used frequently to measure the size of magnetic domains in ferromagnetic samples [120, 121] and GOES [122], the high internal magnetic fields of NGOES in combination with the small domain size lead to a complete depolarization of the neutron beam, preventing neutron depolarization from

being used. In contrast, as shown in the previous section, nGI can recover information about the magnetic properties using scattering from the distribution of magnetic domains. In the following, we consider two possible ways to analyze the data provided by nGI.

Randomly oriented magnetic domains

As noted in Sec. 2.1, the description of the distribtuion of magnetic domains inside a polycrystalline ferromagnet is not trivial. For the following evaluation, we assume that the magnetization directions of all domains show random distribution in case no external magnetic field is present. Furthermore, we assume that the domain size can be described approximately by assuming spherical magnetic domains with a normally distributed diameter. Effectively, we consider the magnetic domains a sort of foam. Ordinarily, the scattering of such a foam is characterized by the form factor F and the structure factor S, as the scattering length density varies periodically. Due to the random orientation of the magnetization direction, the scattering length density also varies randomly; hence for the analysis, we treat every magnetic domain as an isolated sphere ($S = 1$). This simplification allows us to recover information about the average size of the magnetic domain D_{ROMD}, their variance in size σ_{ROMD} as well as the DFI extinction coefficient Σ_{ROMD} of magnetized electrical steel.

Spin misalignment scattering

Another option to describe the scattering is to use a spin misalignment scattering model based on a micromagnetic approach, as shown in Sec. 2.2 and in, e.g., [15]. Here the scattering off of spin misalignment due to perturbations in the material is considered. We consider our domain structure as areas of uniform magnetization with an average diameter D_{Micro} with b_{Micro} describing the dominating factor for perturbations in the spin microstructure [15]. Σ_{Micro} again denotes the DFI extinction coefficient.

5.3.2. Experimental Setup

We performed scans of the correlation length using the nGI at the ANTARES imaging beamline to analyze the magnetic microstructure using the NGOES samples R1 and C. Sec. 4.4 details the sample parameters and embossing process. Fig. 5.5 shows an image of sample C and the corresponding DFI at $785\,\mathrm{A\,m^{-1}}$. Here we indicate the areas, embossed, embossed edge, flux concentration, and flux reduction, used for further analysis. We placed the samples in a magnetic yoke (See Sec. 4.2.4) for the measurement, with the rolling direction (RD) of the sample parallel to the applied

magnetic field H_{app}. Both RD and H_{app} were perpendicular to the grating lines.
We scanned the correlation length ξ by varying the distance between the sample and G_2. For sample R2, ξ was varied in 10 non-equidistant steps between 0.84 µm and 13 µm and for sample C between 0.84 µm and 9.71 µm in six steps. At every scanned correlation length H_{app} was varied from 27 A m^{-1} to 26 880 A m^{-1}.
To keep the DFI extinction coefficient Σ constant at all correlation lengths, the wavelength was fixed at 4 Å. As a result, the spatial resolution changes from $\approx$ 100 µm at the smallest correlation length to $\approx$ 1000 µm at the largest correlation length. For every H_{app}, we performed an nGI scan with ten steps over one grating period. We took three images at every step, each with an exposure time of 20 s. Hence, the total exposure time amounted to 600 s for every DFI. The detector had an effective pixel size of 33 µm $\times$ 33 µm with a 100 µm thick scintillation screen.
Due to an error in the detector system, we acquired no data for sample C at correlation length $\xi = 0.84$ µm and $H_{app} > 2251$ A m^{-1}.

5.3.3. Randomly oriented magnetic domain approach

Evaluation procedure

For the evaluation of the H_{app} dependent size of magnetic domains using a randomly oriented magnetic domain (ROMD) model, we consider a 10 mm $\times$ 10 mm area centered around the embossing of sample C and use the same area in sample R1 as a reference. To increase the dynamic range of the DFI signal (see Sec. 3.2.3), a 5×5 pixel binning was used for every raw image. Then we performed the standard DFI evaluation scheme of fitting the oscillation in every binned pixel as presented in Sec. 3.2.3. To model the change in the DFI signal for every pixel during the scan of the correlation length (ξ), we use the following equation:

$$DFI(\xi, D_{ROMD}, \sigma_{ROMD}, \Sigma_{ROMD}) = \exp\left[\Sigma_{ROMD}\, t \left(\frac{G(\xi, D_{ROMD}, \sigma_{ROMD})}{G(0, D_{ROMD}, \sigma_{ROMD})} - 1\right)\right] \quad . \quad (5.1)$$

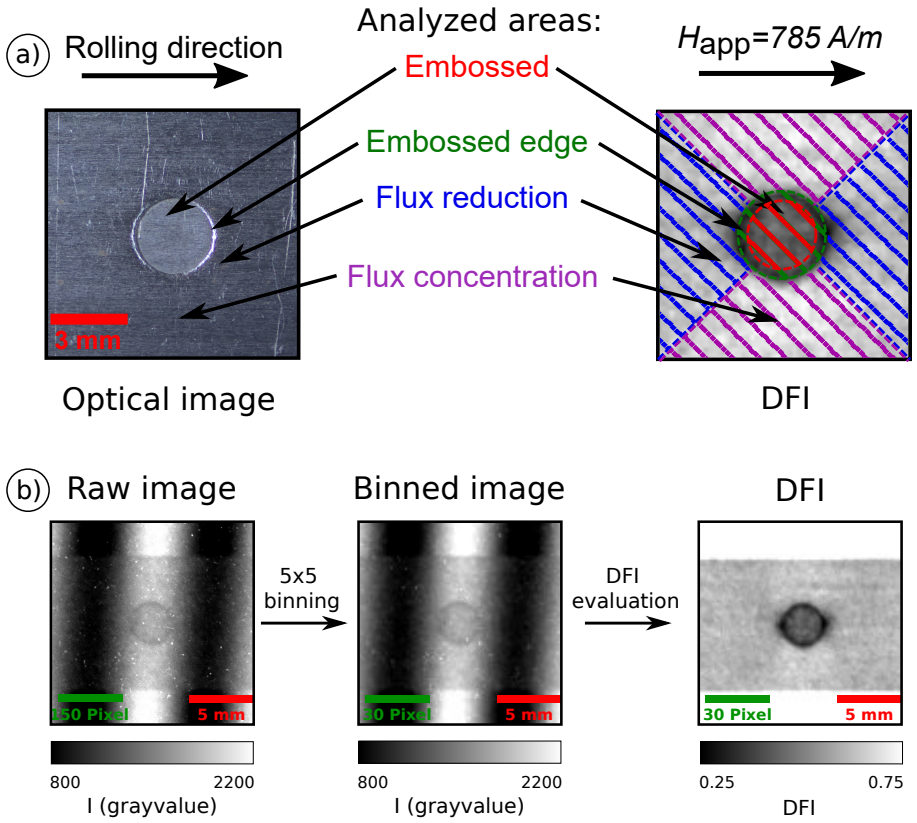

Figure 5.5.: a) Optical image (left) and DFI (right) of sample C. The DFI has been taken at an applied magnetic field of 785 A m^{-1}. The rolling direction of the sample and applied magnetic field H_{app} direction are parallel with respect to each other but perpendicular to the grating lines of the nGI-setup. The colored hatching indicates the different evaluated areas. b) Data processing from raw data to DFI used in Sec. 5.3. Before DFI evaluation, as shown in Fig. 3.3, a 5x5 pixel array is averaged to a single pixel (binning), increasing the signal-to-noise ratio, enabling the analysis of low DFI signals (see Sec. 3.2.3).

The normalized correlation function $\frac{G(\xi,D_{\mathrm{ROMD}},\sigma_{\mathrm{ROMD}})}{G(0,D_{\mathrm{ROMD}},\sigma_{\mathrm{ROMD}})}$ can be calculated from Eq. 2.35:

$$\frac{G(\xi,D,\sigma)}{G(0,D,\sigma)} = \Re\left(\left[1-\left(\frac{\xi}{\mathcal{N}(D,\sigma^2)}\right)^2\right]^{\frac{1}{2}}\left[1+\frac{1}{2}\left(\frac{\xi}{\mathcal{N}(D,\sigma^2)}\right)^2\right] + 2\left(\frac{\xi}{\mathcal{N}(D,\sigma^2)}\right)^2\left(1-\frac{\xi}{2\mathcal{N}(D,\sigma^2)}\right)^2 \ln\left[\frac{\frac{\xi}{\mathcal{N}(D,\sigma^2)}}{1+\left(1-\left(\frac{\xi}{\mathcal{N}(D,\sigma^2)}\right)^2\right)^{\frac{1}{2}}}\right]\right) \quad (5.2)$$

For the sake of readability we use the short hand notations D and σ instead of D_{ROMD} and σ_{ROMD}, respectively, in Eq. 5.2. $\mathcal{N}(D,\sigma^2)$ describes the normal distribution of the domain diameter around its expectation value D and the standard deviation σ.
Using a least squares approach, we fit Eq. 5.1 to the correlation length-dependent change of the DFI for every pixel. The fit parameters for Eq. 5.1 are the average domain diameter (D_{ROMD}), the relative variance of the domain diameter(σ_{ROMD}), and the dark field extinction coefficient of the DFI (Σ_{ROMD}). This approach of fitting the data is similar to the one presented in [123], where the size of magnetic domains in the bulk of polycrystalline Fe was determined using USANS.

Results

For a quantitative analysis of the change in a fitting parameter, we divide sample C into four areas, the flux reduction area (blue), the flux concentration area (magenta), the embossed edge area (green), and the embossed area (red). Fig. 5.5 shows the location of these areas in the sample. In addition, we consider sample R1 as a virgin area (black). In Fig. 5.6, we plot the average DFI value of every area (filled circles) and the

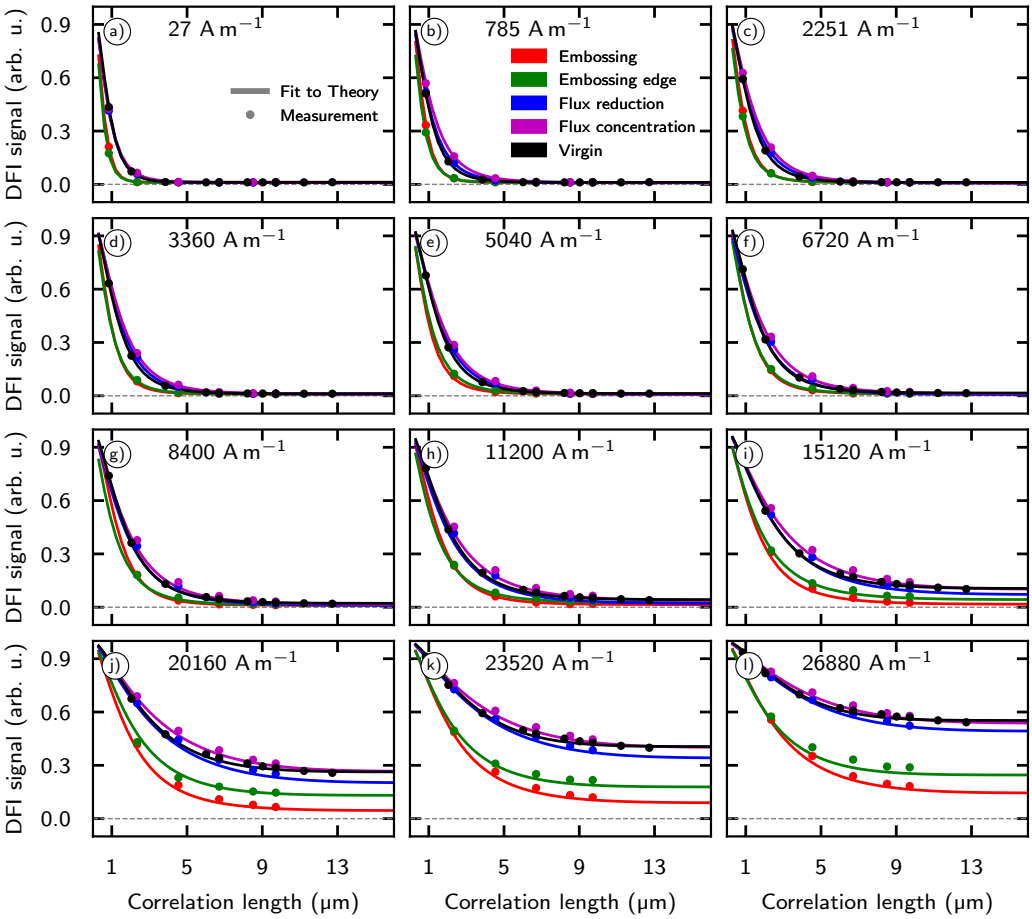

Figure 5.6.: Evaluated DFI data vs. correlation length ξ (filled circles) and corresponding theory fit according to Eq. 5.1 (solid lines) of the considered areas, embossed (red), embossed edge (green), flux concentration (magenta) and flux reduction (blue) shown for sample C in Fig. 5.5 and the virgin sample R1 (black).

corresponding fit of the correlation function (Eq. 5.1) (solid lines) vs. the correlation length for every applied H_{app}. The fit shows for all areas good agreement with the data points, with slightly increased deviations for $H_{\text{app}} \geq 23\,520\,\text{A m}^{-1}$. Regardless of the applied magnetic field, the DFI signal decreases towards higher correlation lengths,

indicating increased scattering. At $H_{app} < 8400\,A\,m^{-1}$, the DFI signal decays, for large correlation lengths, to a noise-defined constant value. Hence the evaluated Σ value in this regime may be larger, as the noise-defined constant value distorts the correlation function. This distortion leads to an incorrect evaluation of the correlation function. This effect is presented in detail in Sec. 3.2.3 in Fig. 3.7 and Fig. 3.8.
For all magnetic fields, the DFI in the flux concentration, flux reduction, and virgin areas show a similar decay toward the noise-defined constant value. For H_{app} between $27\,A\,m^{-1}$ and $11\,200\,A\,m^{-1}$, the DFI signal in the embossed edge area and the embossed area shows a similar faster decay toward the noise-defined constant value than observed for the other areas. At higher magnetic fields, the decay of the DFI signal in the embossed area is faster than for the embossed edge area. At magnetic fields above $11\,200\,A\,m^{-1}$, the DFI value at large correlation lengths increases from 0.01 to a maximum value of 0.5 for the flux concentration, flux reduction, and virgin area. In contrast, the DFI of the embossed and embossed edge area increases from 0.01 to 0.2 and 0.3, respectively.

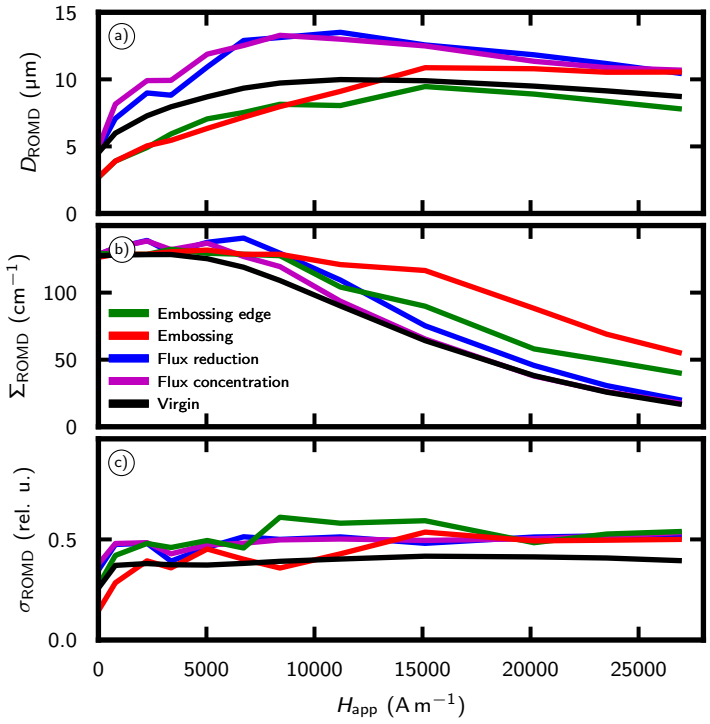

Figure 5.7.: Comparison of the mean fit parameters of the embossed (red), embossing edge (green), flux reduction (blue) and flux concentration (magenta) area of sample C with the virgin area (black) of the reference sample R1.

In Fig. 5.7, the change of the fit parameters D_{ROMD}, σ_{ROMD} and Σ_{ROMD} vs. the applied magnetic field is presented for the considered areas. The virgin, flux reduction, and flux concentration area show a mean domain diameter of $D_{\mathrm{ROMD}} = 4.6\,\mu\mathrm{m}$ at $H_{\mathrm{app}} = 27\,\mathrm{A\,m^{-1}}$. The virgin area has a maximum $D_{\mathrm{ROMD}} = 10\,\mu\mathrm{m}$ at $H_{\mathrm{app}} = 11\,200\,\mathrm{A\,m^{-1}}$, in contrast, D_{ROMD} of the flux reduction and flux concentration area reaches a maximum $\approx 13\,\mu\mathrm{m}$ also at $H_{\mathrm{app}} = 11\,200\,\mathrm{A\,m^{-1}}$. For $H_{\mathrm{app}} \leq 5040\,\mathrm{A\,m^{-1}}$ the guidance of the magnetic flux due to residual stress causes D_{ROMD} in the flux concentration area to be higher than in the flux reduction area.
D_{ROMD} in the embossed (embossed edge) area increases from $2.5\,\mu\mathrm{m}$ ($2.5\,\mu\mathrm{m}$) at $H_{\mathrm{app}} = 27\,\mathrm{A\,m^{-1}}$ to $10\,\mu\mathrm{m}$ ($9\,\mu\mathrm{m}$) at $H_{\mathrm{app}} = 15\,120\,\mathrm{A\,m^{-1}}$, respectively. At higher H_{app} D_{ROMD} is constant for the embossed area, while it decreases towards $8\,\mu\mathrm{m}$ at $H_{\mathrm{app}} = 26\,880\,\mathrm{A\,m^{-1}}$ for the embossed edge area.
For $H_{\mathrm{app}} < 5040\,\mathrm{A\,m^{-1}}$ Σ_{ROMD} is relatively constant at $120\,\mathrm{cm^{-1}}$, which is caused by the noise limit of the DFI (see, e.g., Sec. 3.2.3). At higher H_{app} Σ_{ROMD} starts to decrease for all areas. The three non-embossed areas decrease to $20\,\mathrm{cm^{-1}}$, while the embossed area decreases to $55\,\mathrm{cm^{-1}}$ and the embossing edge area to $45\,\mathrm{cm^{-1}}$. In contrast to the other parameters, σ_{ROMD} is approximately constant for all considered areas and H_{app}. The virgin sample R1 has a slightly lower σ_{ROMD} at 0.4, while sample C roughly has a σ_{ROMD} of 0.5 in all areas. In addition to the analysis of the different considered areas, we can also pixel-wise map D_{ROMD}, σ_{ROMD} and Σ_{ROMD}. Fig. 5.8 presents these maps for both samples and all H_{app}.

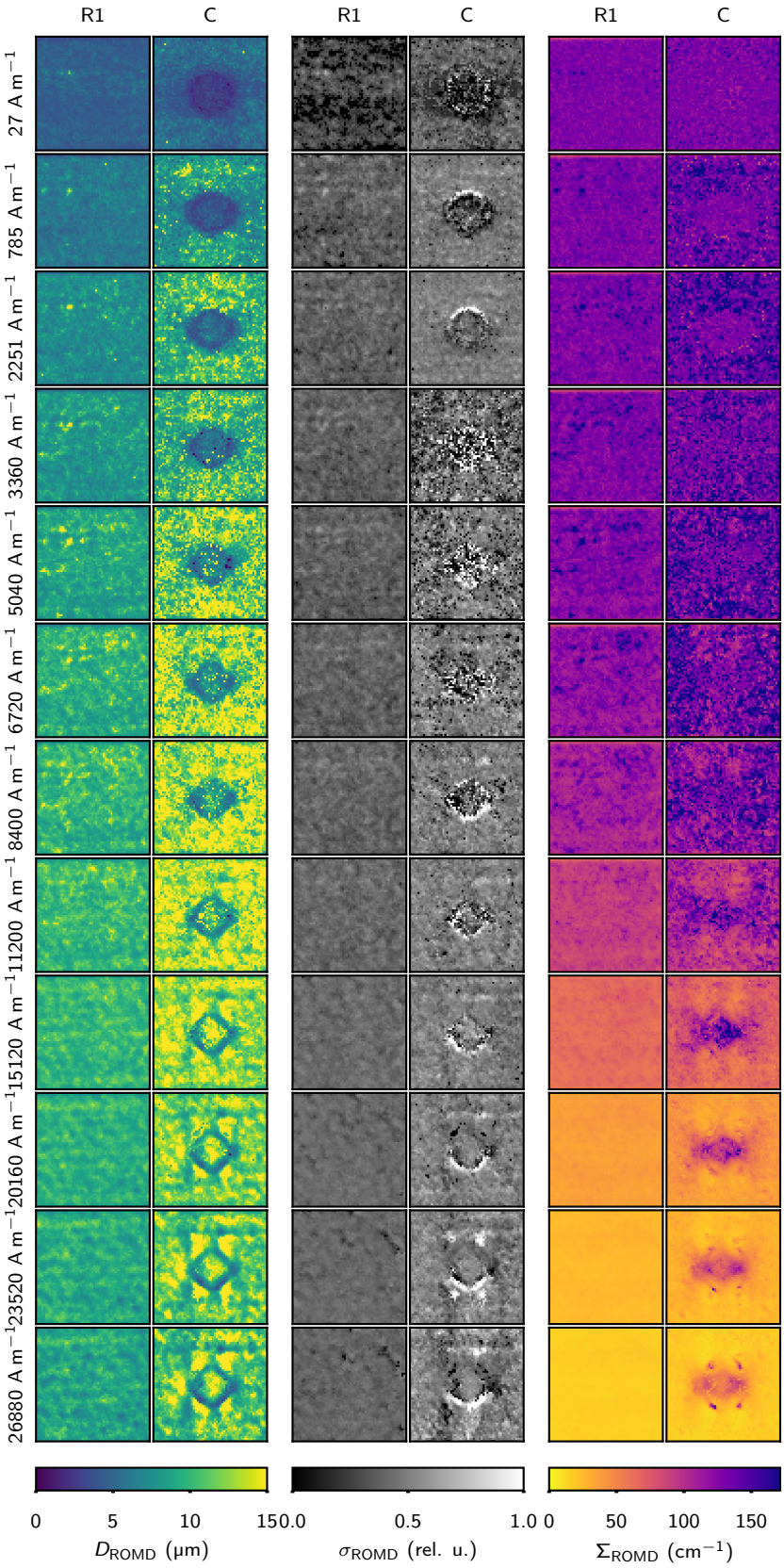

Figure 5.8.: Calculated D_{ROMD} (left column), σt_{ROMD} (middle column) and Σ_{ROMD} (right column) for samples R1 and C using Eq. 5.1 for increasing magnetic fields.

Comparing the D_{ROMD}-map of sample C with sample R1 the influence of the embossing is visible as a decrease in D_{ROMD} in the embossed area. D_{ROMD} increases for both C and R1 with increasing H_{app}, while Σ_{ROMD} decreases. While the influence of the embossing is not visible in Σ_{ROMD} for small H_{app}, the effect of embossing is visible when the magnetic field increases. In contrast, σ_{ROMD} is constant with respect to changes of H_{app}. We also observe, a significant amount of noise in D_{ROMD}, σ_{ROMD} and Σ_{ROMD} for sample C. D_{ROMD} of sample R1 shows some sort of structuring at $H_{\mathrm{app}} \geq 20\,160\,\mathrm{A\,m^{-1}}$.

Discussion

For $H_{\mathrm{app}} \leq 5040\,\mathrm{A\,m^{-1}}$ D_{ROMD} in the flux concentration area is increased compared to the flux reduction area. The domain diameter shows no difference between the two areas at higher applied magnetic fields. This result corresponds to the expectation that the residual stress induced by embossing causes magnetic flux to be concentrated in the flux concentration area, resulting in higher magnetic polarization at the same H_{app} and larger magnetic domains. At higher $H_{\mathrm{app}} > 5040\,\mathrm{A\,m^{-1}}$ the effectiveness of the embossing as a flux barrier decreases, hence D_{ROMD} of the two areas equalizes.
In comparison, the virgin area in sample R1 shows, regardless of H_{app}, a smaller D_{ROMD}, with a similar trend as the flux concentration and reduction area. The maximum D_{ROMD} for the virgin area is reached for $H_{\mathrm{app}} \approx 10\,000\,\mathrm{A\,m^{-1}}$. This difference may be due to differences in the two materials, resulting in different sizes of magnetic domains. Another reason may also be the decreased number of correlation lengths and ranges probed for sample C compared to R1. Due to a problem in the detector system, the data points at $\xi = 0.84\,\mu\mathrm{m}$ are missing for at $H_{\mathrm{app}} > 2332\,\mathrm{A\,m^{-1}}$, reducing the data quality. The missing information may also be the reason for the increased noise present in the evaluated data in Fig. 5.8 for sample C.
The increasing diameter of the magnetic domains D_{ROMD} at rising H_{app} can be seen as a growth of magnetic domains oriented favorably to the magnetization direction [118]. In a crystalline material, the magnetization direction of the magnetic domains is oriented parallel to its magnetic easy axes [124]. Assuming one of the easy axes is along the same direction as the applied magnetic field, the magnetic domain whose magnetization direction is the same as the applied magnetic field grows. In case of a mismatch of the easy axis with the magnetization axis, the domain whose magnetization orientation has the smallest mismatch will grow and, depending on the energy cost, also rotate towards the direction of the applied magnetic field [18]. Typically, at lower magnetic fields, domain growth is observed while domain rotation occurs at higher applied magnetic fields [8, 18, 124].
We also observe an apparent decrease in D_{ROMD} for $H_{\mathrm{app}} > 11\,200\,\mathrm{A\,m^{-1}}$. This

decrease may be an artifact of the limited accessed range of the correlation length and the increase in correlation length where the correlation function reaches saturation due to the increase in applied magnetic field.
The embossed and embossed edge areas show a decreased diameter of the magnetic domains compared to the virgin, flux reduction, and flux concentration areas. In this area, the residual stress changes the magneto elastic energy contribution, which leads to a decrease in the size of the magnetic domains [8, 18]. In addition, deformation and residual stress reduce the mean grain size of the electrical steel [105, 125]. This reduction of grain size increases the ratio of smaller closure domains on the edge of the grain relative to larger internal domains [8].
The decrease of Σ_{ROMD} at higher magnetic fields for all areas indicates that the magnetic domains' orientations align parallel to the applied magnetic field, reducing the difference in scattering length density in the observed samples.
σ_{ROMD} remains for all considered areas roughly constant when increasing H_{app}. The lower variance observed in the virgin sample may be due to different material properties. A comparison of the raw data and the fitted curves in Fig. 5.6 shows a generally good agreement, which indicates the suitability of the ROMD-model to fit the data. However, we note that the correlation function needs to be probed at a sufficiently high number of correlation lengths and over a wide range for better results.
We note that sample R1 in Fig. 5.8 shows for $H_{\mathrm{app}} \geq 15\,120\,\mathrm{A\,m^{-1}}$ some structure in the D_{ROMD}-map. As this structure remains relatively constant with increasing H_{app} and can also be found in the D_{Micro}-maps presented in 5.11, we are confident that this is not caused by random variation in the data or as an artifact of the ROMD-model. Some macroscopic structure in the material possibly causes this variation, which may be a remnant of the manufacturing process. A full explanation for this structure has yet to be made available.

5.3.4. Micromagnetic approach

Evaluation procedure

For the evaluation of the H_{app} dependent magnetic domain size using the micromagnetic spin-misalignment (Micro) model, we consider the same areas as for the ROMD-model. The areas are shown in Fig. 5.5 a). To increase the dynamic range of the DFI signal (see Sec. 3.2.3), a 5×5 binning was used for every raw image. The procedure is shown in Fig. 5.5 b). Then we used the standard DFI evaluation scheme of fitting the oscillation in every pixel as presented in Sec. 3.2.3. To model the change in the

DFI signal for every pixel during the scan of the correlation length (ξ), we use the following equation:

$$DFI(\xi, D_{\text{Micro}}, b_{\text{Micro}}, \Sigma_{\text{Micro}}) = \exp\left[\Sigma_{\text{Micro}} t \left(\frac{G(\xi, D_{\text{Micro}}, b_{\text{Micro}})}{G(0, D_{\text{Micro}}, b_{\text{Micro}})} - 1\right)\right] . \quad (5.3)$$

For the sake of readability, we used the short hand notation D and b instead of D_{Micro} and b_{Micro}, respectively, in the following equation. The normalized correlation function $\frac{G(\xi,D,b)}{G(0,D,b)}$ can be calculated from the equations presented in Sec. 2.2.2:

$$\begin{aligned}\frac{G(\xi,D,b)}{G(0,D,b)} &= \frac{\int \left(\frac{d\Sigma_{\text{M}}}{d\Omega}(q_x,D,b)\right) \frac{\sin(q_x\xi)}{q_x\xi} q_x^2 dq_x}{\int \left(\frac{d\Sigma_{\text{M}}}{d\Omega}(q_x,D,b)\right) q_x^2 dq_x} \\ &= \frac{\int P(\xi,D)S(\xi)\left(b\frac{p^2}{4}\left(2+\frac{1}{\sqrt{1+p}}\right)+\frac{\sqrt{1+p}-1}{2}\right)\frac{\sin(q_x\xi)}{q_x\xi} q_x^2 dq_x}{\int P(\xi,D)S(\xi)\left(b\frac{p^2}{4}\left(2+\frac{1}{\sqrt{1+p}}\right)+\frac{\sqrt{1+p}-1}{2}\right) q_x^2 dq_x}\end{aligned} \quad (5.4)$$

Here $P(\xi,D)$ is the form factor of spherical particles and $S(\xi)$ the structure factor as introduced in Sec. 2.2.2:

$$P(\xi,D) = 9\frac{j_1^2(\xi D/2)}{(\xi D/2)^2} \text{ and} \quad (5.5)$$

$p = p(q_x, H_{\text{app}})$ is the dimensionless function introduced in Eq. 2.26, containing information about the material parameters:

$$p(q_x, H_{\text{app}}) = \frac{M_s}{H_{\text{app}}\left(1 + \frac{2A}{\mu_0 M_s H_{\text{app}}} q_x^2\right)} \quad (5.6)$$

The fit parameters in Eq. 5.3 are the average domain diameter (D_{Micro}), b_{Micro} and the dark field extinction coefficient (Σ_{Micro}). Similar to [14], we set for simplicity $S(\xi) = 1$ as our data shows no strong impact of dense packing. We approximated the integrals in Eq. 5.4 by Riemann integration. The resulting expressions were fitted using a Levenberg-Marquardt least squares approach. This approach to fitting the data is similar to the one presented in [15]. For Eq. 5.6, we use the saturation magnetization $M_s = 1.75 \times 10^6\,\text{A}\,\text{m}^{-1}$ and the exchange stiffness $A = 1.5 \times 10^{-11}\,\text{J}\,\text{m}^{-1}$ as material parameters of the NGOES samples. μ_0 is the vacuum magnetic permeability.

Results

Similar to Sec. 5.3.3, we divide sample C into four areas, the flux reduction area (blue), the flux concentration area (magenta), the embossed edge area (green), and the embossed area (red). These areas are shown in Fig. 5.5. In addition, we consider sample R1 as a virgin area (black). In Fig. 5.9, the mean data value (filled circles) and the corresponding correlation function fits (solid lines) vs the correlation length are shown. The fits and data points show good agreement in general. However, at $H_{\text{app}} \geq 23\,520\,\text{A}\,\text{m}^{-1}$, the quality of the fit degrades slightly.

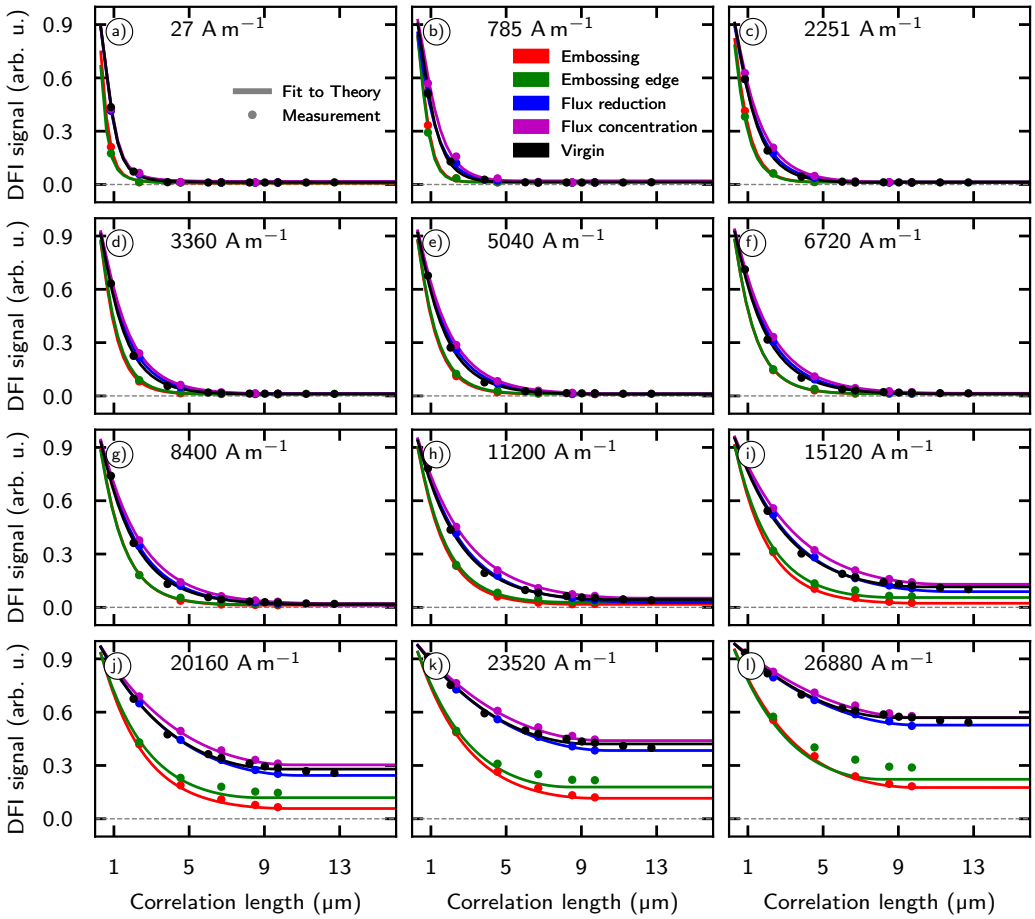

Figure 5.9.: Evaluated DFI data (filled circles) vs. correlation length ξ and theory fit according to Eq. 5.3 (solid lines) of the considered areas, embossed (red), embossed edge (green), flux concentration (magenta) and flux reduction (blue) shown for sample C in Fig. 5.5 and the virgin sample R1 (black).

In Fig. 5.10, we compare the change of the fit parameters a) D_{Micro}, b) Σ_{Micro} and c) b_{Micro} vs. H_{app} for the embossed (red), embossed edge (green), flux reduction (blue) and flux concentration (magenta) area of sample C with the virgin area (black) of sample R1. D_{Micro} for the virgin, flux concentration and flux reduction area is

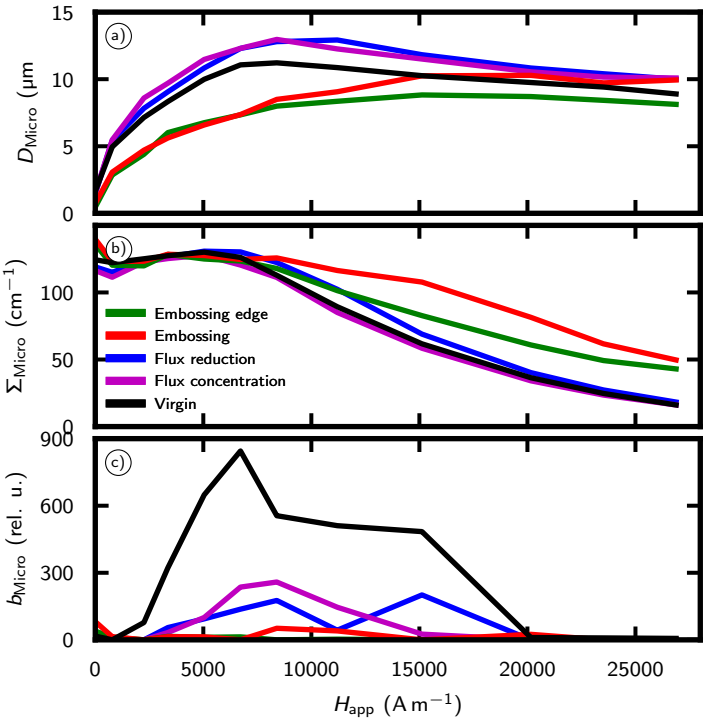

Figure 5.10.: Change of the fit parameters a) D_{Micro}, b) Σ_{Micro} and c) b_{Micro} vs. the applied magnetic field in the considered areas. The embossed (red), embossed edge (green), flux reduction (blue) and flux concentration (magenta) area of sample C are compared with the virgin area (black) of sample R1.

1.8 µm for $H_{\mathrm{app}} = 27\,\mathrm{A\,m^{-1}}$. The maximum D_{Micro} of the virgin area is $\approx 11\,\mu\mathrm{m}$ at $H_{\mathrm{app}} = 8400\,\mathrm{A\,m^{-1}}$. The flux concentration and reduction areas show a maximum diameter of $\approx 13\,\mu\mathrm{m}$ at $H_{\mathrm{app}} = 8400\,\mathrm{A\,m^{-1}}$ and $11\,200\,\mathrm{A\,m^{-1}}$, respectively. For $H_{\mathrm{app}} \leq 5040\,\mathrm{A\,m^{-1}}$ the guidance of the magnetic flux due to residual stress causes D_{Micro} in the flux concentration area to be higher than in the flux reduction area. Above $H_{\mathrm{app}} = 11\,200\,\mathrm{A\,m^{-1}}$ the diameter decreases. The embossed and embossed edge area show a D_{Micro} of 0.7 µm at $H_{\mathrm{app}} = 27\,\mathrm{A\,m^{-1}}$, which increases to its maximum of 10.4 µm and 8.4 µm, respectively, at $H_{\mathrm{app}} = 20\,160\,\mathrm{A\,m^{-1}}$. For higher H_{app}, the domain diameter for the embossed and embossed edge area is roughly constant.
For $H_{\mathrm{app}} < 5040\,\mathrm{A\,m^{-1}}$ Σ_{Micro} is relatively constant at $120\,\mathrm{cm^{-1}}$, which is likely an artifact of the noise limit of the DFI (see, e.g., Sec. 3.2.3). At higher H_{app} Σ_{ROMD}

starts to decrease for all areas. The three non-embossed areas decrease to $20\,\mathrm{cm}^{-1}$, while the embossed area decreases to $50\,\mathrm{cm}^{-1}$ and the embossing edge area to $40\,\mathrm{cm}^{-1}$. In contrast to the other parameters, the value of b_{Micro} varies widely between 7×10^{-9} and 820.

Similar to Sec. 5.3.3, we present the maps of the diameter D_{Micro}, DFI extinction coefficient Σ_{Micro} and the ratio b_{Micro} dependent on H_{app} for samples C and R1 in Fig. 5.11.

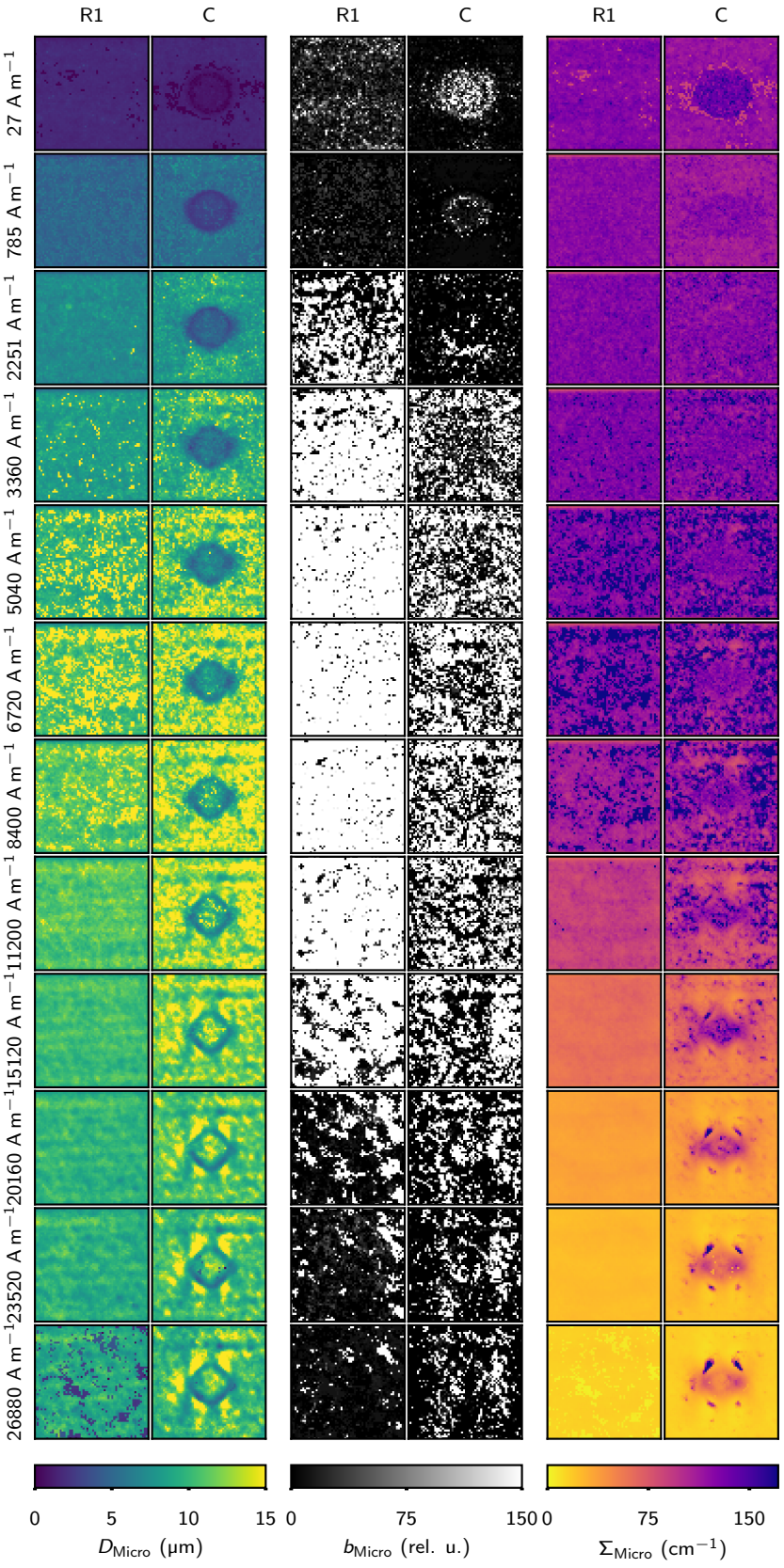

Figure 5.11.: Calculated D_{Micro} (left column), b_{Micro} (middle column) and Σ_{Micro} (right column) for samples C and R1 using Eq. 5.3 for increasing magnetic fields.

As in Fig. 5.8, we observe a strong influence of the embossing in the D_{Micro}-map. Again the embossed area shows a decrease in D_{Micro} compared to the surrounding area. For $H_{\text{app}} \leq 8400\,\text{A}\,\text{m}^{-1}$ the effect of the embossing is less signifcant in the Σ_{Micro}-map. We observe a signifcant change in the b_{Micro}-maps dependent on the applied magnetic field, with high b_{Micro} values for an applied magnetic field $2251\,\text{A}\,\text{m}^{-1} \leq H_{\text{app}} \geq 15\,120\,\text{A}\,\text{m}^{-1}$.

Discussion

D_{Micro} and Σ_{Micro} show similar trends and values as observed for the ROMD-model in Sec. 5.3.3. We again observe an increased D_{Micro} for $H_{\text{app}} \leq 5400\,\text{A}\,\text{m}^{-1}$ in the flux concentration area compared to the flux reduction area. As noted before, the magnetic flux deflection due to the induced residual stress causes this difference. At higher applied magnetic fields, this effect vanishes due to the reduced effect of the embossing. In contrast to the ROMD-model, the value of D_{Micro} in the virgin area is close to the flux reduction and concentration area values. As with the ROMD-model, the difference in value between the virgin area and the flux concentration and reduction area may be a result of variations in the material or be caused by the reduced number of measurement points used for sample C compared to sample R1.
The increase in D_{Micro} with increasing applied magnetic field again indicates a growth of the magnetic domains oriented favorably to the magnetization direction. The decrease of Σ_{Micro} at increasing H_{app} indicates the onset of domain rotation parallel to the applied magnetic field [8, 124]. For volumes with residual stress, the magnetoelastic energy contribution changes, which decreases the diameter of the magnetic domains. In addition, the magnetic permeability decreases [70, 113], leading to a decreased magnetization in this area at the same applied magnetic field compared to an area without residual stress.
The variation between D_{Micro} and D_{ROMD} may result from the different approaches in the two models. In the case of the ROMD-model, we assumed that we could view the distribution of magnetic domains as an ensemble of isolated spheres, for which we can fit the mean domain diameter D_{ROMD} as well as its variance σ_{ROMD}. For the micromagnetic model, we assumed that the diameter is the area of homogeneous magnetization with spin-misalignment fluctuations extending outside. The parameter b_{Micro} describes the extent of the spin-misalignment fluctuations and the power-law dependence of the correlation function [15, 32]. This dependence of the decay of the correlation on b_{Micro} may cause the difference in the fitted diameter.
The significant variance of b_{Micro} at different H_{app} may indicate that this model is not well suited to the USANS data. The slightly worse fit may be because while the theory works well within the SANS regime (nanometer), the length scales probed by

nGI are in the micrometer regime. We expected this theory to work reasonably well, as theories developed for SANS, i.e., scattering theory of two-phase system [88] generally also work for nGI [77]. One reason may be that the interactions considered in the spin misalignment approach (i.e., exchange length) are only on the nanometer scale, and the nGI does not detect them.
In contrast, the absolute value of Σ_{Micro} fits quite well to Σ_{ROMD}. This match fits our expectation as the DFI signal in the correlation length regime, where the correlation function reaches zero, defines the extinction coefficient. The extinction coefficient should be roughly the same regardless of the applied model. An exception is high H_{app}, as the correlation function has not fully decayed to zero, causing the uncertainty of Σ to rise.
However we need to note, that the fit parameters required extensive tuning for the least squares approach to work.

5.3.5. Conclusion

In the previous section, we have shown that we can extract information about the internal domain distribution of embossed and virgin NGOES using the correlation length-dependent change in the DFI signal. We have studied two approaches; one assumes randomly oriented magnetic domains with a specific domain size distribution (ROMD), and the other considers scattering based on spin misalignment within a micromagnetics approach (Micro). The ROMD-model considers no magnetic parameters except for the size of magnetic domains. In contrast, the Micro model includes the exchange stiffness constant, the domain size, and the saturation magnetization as magnetic material parameters.
Both models show good agreement between raw data points and the resulting fits. However, while the Micro model links to additional magnetic parameters, this also poses problems during the fit of the correlation function. Due to the limited range of correlation lengths, the density of the points in the range of correlation lengths, and the form of the correlation function, the fitting remains relatively unstable. It requires previous knowledge about magnetic parameters such as saturation magnetization and exchange stiffness constant. For homogeneous samples, these parameters can be accessed by, e.g., vibrating sample magnetometer measurements. In the case of inhomogeneous samples, such a procedure is challenging or even impossible to apply. In contrast, the ROMD-model allows extraction of the dependence of the local distribution of magnetic domains on H_{app} and the residual stress state. Normally the local domain distribution can only be visualized close to the surface. Hence we visualized the local domain distribution in the bulk of NGOES for the first time.
Previously, the distribution magnetic domains was mainly mapped on the surface of a

sample using various techniques, such as the MOKE or Bitter method. In the case of single crystals, the knowledge of the closure domains on the surface of the sample allows us to reconstruct the magnetic domains in the bulk of the sample. Considering the polycrystalline nature of NGOES, these procedures are not applicable. While USANS has been used previously to access the size of magnetic domains in FeSi, the sample thickness was limited to 50 µm to prevent multiple scattering [123]. Due to the nature of a USANS beamline, no spatial information about the domain distribution was gathered.
The presented data shows that quantitatively analyzing the distribution of magnetic domains in ferromagnets using DFI is possible and can be used to understand the complex interaction of residual stress with the magnetic flux. Introducing residual stress decreases the domain size at a specific H_{app} compared to a sample without residual stresses. Here, the magnetoelastic energy contribution to the total magnetic energy changes. Due to this, smaller magnetic domains are energetically favorable. In addition, the introduced residual stress reduces the magnetic permeability, decreasing the magnetization for an applied magnetic field and reducing the size of magnetic domains.
In the context of the research towards new electric drive topologies, this allows us to understand better how the complex interaction between residual stress and applied magnetic field changes the local distribution of magnetic domains and hence the magnetic properties. In our experiments, we looked at the embossed NGOES case without any applied external strain. However, in a rotating electric drive, centrifugal forces will be present. Therefore, in further experiments, the change of the distribution of magnetic domains in a stressed sample with applied external strain should be evaluated, which would allow us better to understand the magnetic properties of a rotating electric drive.

5.4. Anisotropic magnetic scattering

Due to its one-dimensional construction, an nGI-setup is only sensitive to scattering perpendicular to its grating lines. Hence, we conduct nGI-scans with different grating orientations to detect anisotropic scattering. In the following, we will use this technique to analyze the anisotropy in the magnetic scattering on NGOES at varying applied magnetic fields H_{app} and correlation lengths ξ.

5.4.1. Experimental Setup

To evaluate the anisotropy in scattering off of magnetic domains in NGOES, the orientation of the grating lines relative to the sample has been rotated from $\omega = -90°$ to $\omega = 50°$, where 0° corresponds to vertical grating lines in the nGI-setup. For every ω, H_{app} has been varied from 27 A m^{-1} to 27 800 A m^{-1}. For every H_{app}, we performed an nGI scan with ten steps over one grating period. We took three images at every step, each with an exposure time of 20 s. Hence, the total exposure time was 600 s for every DFI. This procedure has been performed at three correlation lengths $\xi = 0.84$ µm, 2.05 µm and 9.71 µm. This experiment used the virgin sample R1 to evaluate the anisotropic magnetic scattering innate to the electrical steel sheet. The magnetic field was applied parallel to the rolling direction of the sample and perpendicular to the grating lines at $\omega = 0°$.
In Fig. 5.12 a) the DFI of R1 for different ω at $\xi = 0.84$ µm with $H_{app} = 785$ A m^{-1} is shown exemplarily. We see an oscillation of the DFI signal with the maximum and minimum DFI signal at $\omega = 0°$ and $\omega = -90°$, respectively. In b), a photograph of the evaluated sample area (10 mm × 10 mm) is shown. In c) an example for the change in mean DFI signal vs. ω at $H_{app} = 785$ A m^{-1} is presented for the three considered correlation lengths $\xi = 0.84$ µm (blue), 2.05 µm (orange) and 9.71 µm (green). Please note the different scaling of the DFI signal in a) and c). Both $\xi = 0.84$ µm and 2.05 µm show a maximum at $\omega = 0°$, while $\xi = 9.71$ µm has its minimum at this ω value. We will discuss the reason for this discrepancy in the following section.
We used the mean value of the area shown in a) to evaluate the anisotropy. We use a bi-gaussian model (see Sec. 3.2.4) similar to the models presented in [67, 96, 126] to fit the data and extract information about the anisotropy. Here we use the isotropic extinction coefficient Σ_{iso} to model the isotropic scattering and the anisotropic extinction coefficient Σ_{an} to model the increase in scattering along one direction defined by the phase ϕ. For the readers convenience we reproduce the function (Eq. 3.20) used to fit the data points here:

$$DFI(\omega) = \exp\left(-t\left[\Sigma_{iso} + \Sigma_{an}\sin^2(\omega - \phi)\right]\right) \tag{5.7}$$

The model in question is detailed in Sec. 3.2.4.

5.4.2. Change of anisotropy

Fig. 5.13 shows the calculated a) Σ_{iso}, b) Σ_{an} and c) phase ϕ of the bi-gaussian model used to fit the anisotropy data. In d) the relative anisotropy Σ_{an}/Σ_{iso} is given. Σ_{iso} and Σ_{an} denote the isotropic and anisotropic part of the dark field extinction coefficient Σ.

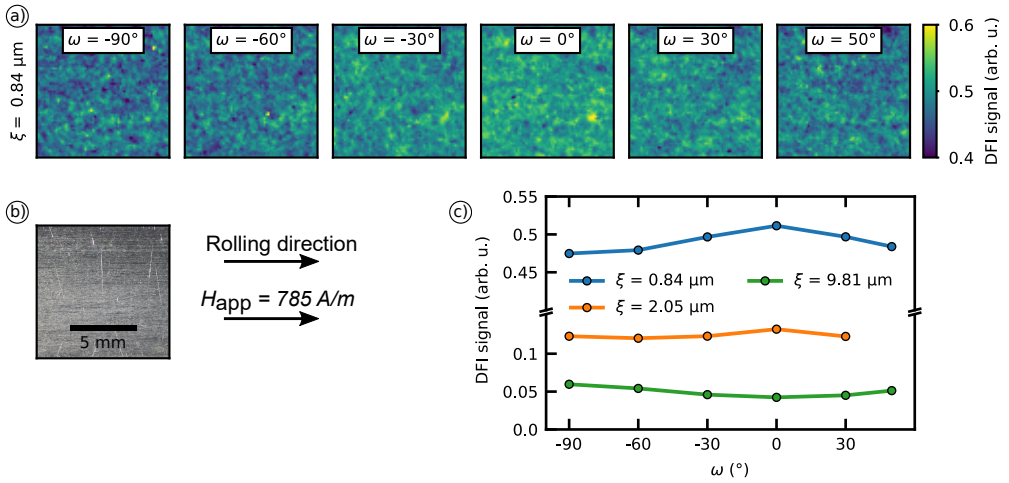

Figure 5.12.: a) DFI of R1 at the measured ω at $\xi = 0.84\,\mu m$ with $H_{app} = 785\,A\,m^{-1}$. b) Photograph of the sample. c) ω dependent change in mean DFI signal for the three considered correlation lengths at $H_{app} = 785\,A\,m^{-1}$. Please note the different scaling of the DFI signal in a) and c).

The phase denotes the angular orientation of Σ_{an}. $\phi = 0°$ denotes elongation of the microstructure along the rolling direction, with increased scattering along the vertical direction. Regardless of accessed correlation length Σ_{iso} decreases towards higher H_{app}. For $\xi = 0.84\,\mu m$ (blue) and $2.05\,\mu m$(*orange*)Σ_{an} similarly decreases towards higher H_{app}. For $\xi = 9.71\,\mu m$ (green) Σ_{an} shows a dip at $H_{app} = 6720\,A\,m^{-1}$ and $8400\,A\,m^{-1}$, but generally decreases towards higher H_{app}. For $\xi = 0.84\,\mu m$ and $2.05\,\mu m$ the phase remains close to 0°, regardless of H_{app}. In contrast ϕ for $\xi = 9.71\,\mu m$ is at $\approx 90°$ for $H_{app} \leqq 6720\,A\,m^{-1}$ and then switches to $\approx 0°$ at $H_{app} > 6720\,A\,m^{-1}$. For $\xi = 0.84\,\mu m$ the relative anisotropy Σ_{an}/Σ_{iso} shows a peak (0.29) at $H_{app} \approx 5000\,A\,m^{-1}$. For both lower and higher H_{app}, the relative anisotropy decreases towards ≈ 0.12. In contrast, for $\xi = 2.05\,\mu m$ the relative anisotropy has its maximum (0.25) at $27\,A\,m^{-1}$ and a small dip at $785\,A\,m^{-1}$. From $H_{app} = 2251\,A\,m^{-1}$ to $11\,200\,A\,m^{-1}$ the relative anisotropy is roughly constant at ≈ 0.13. Towards $H_{app} = 26\,880\,A\,m^{-1}$ the relative anisotropy increases to 0.22. The relative anisotropy of $\xi = 9.71\,\mu m$ shows a dip to 0.03 at $H_{app} = 6720\,A\,m^{-1}$ with an increase to 0.13 (0.1) at high (low) H_{app}, respectively.

5.4.3. Discussion

Except for $\xi = 9.71\,\mu m$ the anisotropy of the scattering shows increased scattering perpendicular to the rolling direction and applied magnetic field direction ($\phi = 0°$),

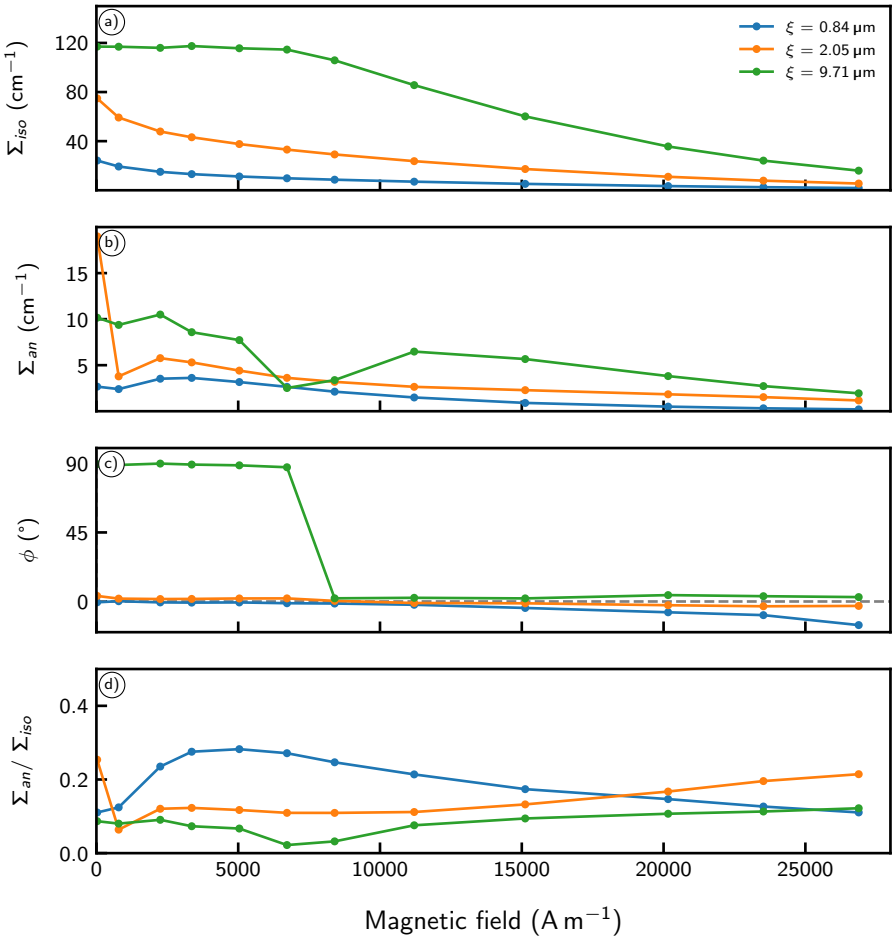

Figure 5.13.: Parameters of Eq. 5.7 describing the anisotropy in scattering off magnetic domains vs H_{app} at correlation lengths $\xi = 0.84\,\mu m$ (blue), $2.05\,\mu m$ (orange) and $9.71\,\mu m$ (green). a) and b) show the isotropic and anisotropic extinction coefficient Σ_{iso} and Σ_{an}, respectively. c) shows the angle of the semi-major axis of the bi-gaussian distribution relative to the grating orientation ϕ. An angle of 0° corresponds to σ_1 parallel to the x-axis. d) presents the ratio of anisotropic to isotropic extinction coefficient Σ_{an}/Σ_{iso}. The sharp change in ϕ for $\xi = 9.71\,\mu m$ at $H_{app} \approx 8400\,A\,m^{-1}$ is an artifact caused by a decrease of the DFI signal below the noise limit for $H_{app} < 8400\,A\,m^{-1}$.

regardless of H_{app}. Assuming that the ROMD-model used in Sec. 5.3.3 is correct, this indicates that the magnetic domains are, on average, elongated along the rolling direction of the material. The elongation likely results from the rolling process used to form the sample. This rolling process introduces stress into the material, which changes the magnetic easy axes of the material [8] and influences the distribution of

magnetic domains. Hence, the domain size recovered with the simplified model in Sec. 5.3.3 is only correct parallel to the rolling direction.
At $\xi = 0.84\,\mu m$, the relative anisotropy at $H_{app} < 15\,120\,A\,m^{-1}$ is increased compared to $\xi = 2.05\,\mu m$, indicating that smaller magnetic domains are more elongated than larger magnetic domains. At higher $H_{app} > 20\,000\,A\,m^{-1}$, this trend reverses, which may be due to the growth of magnetic domains, whereby smaller magnetic domains tend to decrease in number. The apparent rotation of the anisotropy for $\xi = 9.71\,\mu m$ and $H_{app} < 8400\,A\,m^{-1}$ is likely caused by the saturation of the scattering signal and the change in visibility caused by rotation of the gratings. As we have shown in Sec. 3.2.4, the reference visibility of an nGI-setup decreases when rotating the setup from $\omega = 0°$ to $\omega = -90°$. The reference visibility decreases due to the bandwidth of the NVS and the resulting spread in neutron velocities, and the influence of gravity on the neutrons, which results in an additional spread of the neutron beam. In case the sensitivity direction is horizontal ($\omega = 0°$), the vertical spread of neutrons due to gravity is not detected, but for $\omega = -90°$ this spread is detected lowering the reference visibility. An example of this is shown in Fig. 3.11, where the change in visibility depending on the setup orientation and the NVS bandwidth is demonstrated. Usually, a change in visibility does not cause problems, as the DFI is normalized to the reference visibility. However, as we have shown in Sec. 3.2.3, a lower limit of detectable visibility is caused by Poisson noise during the detection of neutrons. This lower limit is independent of the rotation of the nGI-setup; hence for lower reference visibility, the minimum DFI increases.

5.4.4. Conclusion

In the previously discussed experiment, we have shown that the assumption of perfectly isotropic scattering, which we have used in Sec. 5.3.3, does not sufficiently describe the scattering signal. The DFI signal indicates increased scattering perpendicular to the rolling and magnetization direction, which points toward an elongation of the magnetic domains along the rolling direction. The results also show that we need to scan the correlation length and the anisotropy for a complete analysis of the distribution of magnetic domains. For a better understanding of the exact influence of the rolling direction on the distribution of magnetic domains, the dependence of the orientation of the DFI signal on the angle between the rolling direction and the magnetization direction should be analyzed in greater detail.

5.5. Hysteretic behavior of the dark field contrast in electrical steel

While we have discussed the change of the distribtuion of magnetic domains caused by residual stress and applied magnetic field in a previous section, here we will discuss the influence of residual stress on the local hysteretic behavior of electrical steel. First, we will present the experimental parameters for these measurements. Afterward, we will discuss the influence of different embossing strategies on the magnetic hysteresis in a sample where the embossed area covers the whole width of the sample. In a second step, we will analyze the change of magnetic hysteresis in a partially embossed sample where magnetic flux barriers and concentration exist. We note that the hysteresis measured by nGI is not directly comparable to the magnetic hysteresis measured by standard methods such as VSM or SST. In an nGI measurement, the direction of the magnetic polarization B may not be identified as positive and negative polarization cause an increase of the DFI signal. Additionally, as noted before, the DFI tracks the change in distribution of magnetic domainse and not directly the magnetic polarization. While these two properties are connected, the connection is not trivial. Hence, comparing the acquired DFI signal to a standard magnetic hysteresis measurement is impossible. For comparison of the evaluated samples, we use a similar methodology to standard hysteresis measurements.

5.5.1. Connection between DFI and hysteresis

First, we want to remind the reader about the connection between the magnetic polarization of the material and the recorded DFI signal. As mentioned above, this connection is not trivial. An increase in the applied magnetic field H_{app} first leads to a growth in domains oriented favorably with H_{app}, i.e., domain wall movement. At high H_{app}, the domains rotate to align with the magnetic field. The size of the domains is further defined by the metallurgic properties, i.e., impurities and residual stress. These properties also pin the magnetic domain walls, leading to increased coercivity [124]. Assuming a constant neutron wavelength and nGI correlation length, an increase in domain size leads to a non-linear increase of the correlation function G and hence an increase in DFI signal (see Eq. 3.14).
Further complicating the relationship between polarization and DFI signal is that the linear extinction coefficient Σ of the DFI signal is not constant when the domain size changes. As a result of these complicated relationships, the extraction of physically meaningful quantities from the DFI hysteresis is complicated. However, the DFI

uniquely allows to visualize the differences in hysteresis in inhomogeneous materials. In Fig. 5.14, an approximate wing-shaped DFI hysteresis curve is sketched as measured with nGI and the corresponding parameters are given. Here, the remanence M_R^{DFI} is defined as the DFI signal at an applied magnetic field H_{app} of $0\,A\,m^{-1}$. We define the coercivity H_C^{DFI} as the applied magnetic field at the minimum DFI signal DFI_{min} in this hysteresis loop. An additional parameter we consider is the DFI value DFI_{max} reached the maximum H_{app}^{max}. Due to noise in the data, M_R^{DFI}, H_C^{DFI} and DFI_{min} were determined by fitting a parabola to the eight measurement points around the minima at positive and negative H_{app} and taking the mean of the absolute values. By analyzing the opening enclosed by the hysteresis curve, we can attempt to calculate a value for the local energy loss P^{DFI}, which corresponds in some way to the energy loss per cycle P/f calculated from a standard hysteresis loop [127]. In standard magnetic hysteresis measurements, an increase in area corresponds to an increase in energy loss.

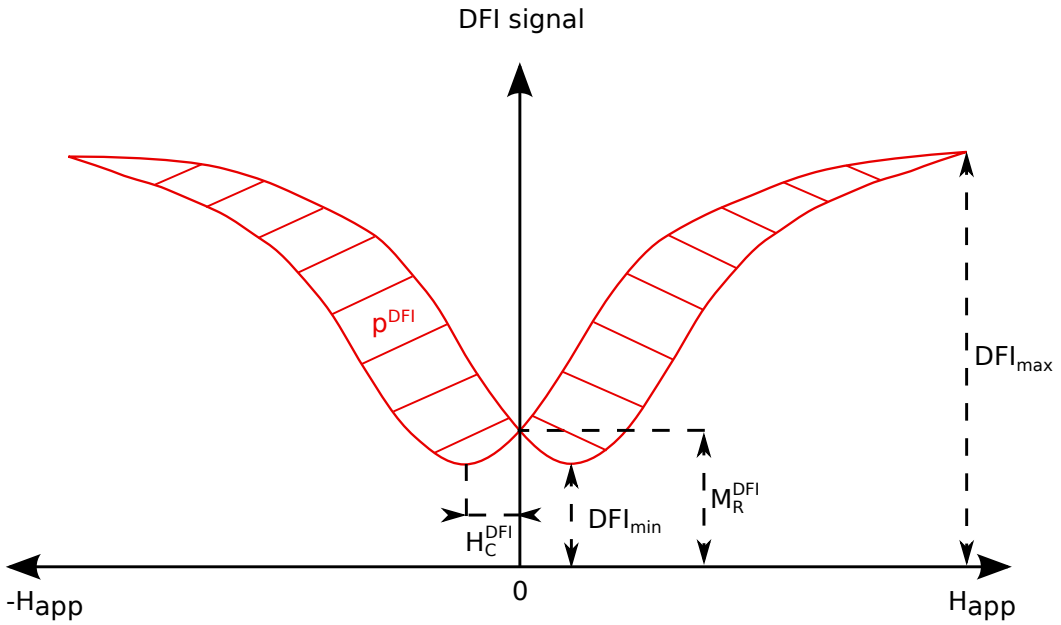

Figure 5.14.: Sketch of a DFI hysteresis curve with its defining parameters, remanence M_R^{DFI}, coercivity H_C^{DFI}, minimum DFI DFI_{min}, maximum DFI DFI_{max} and energy loss P^{DFI}, marked.

5.5.2. Experimental setup

For the analysis of the magnetic hysteresis in embossed electrical steel sheets, we performed nGI measurements at the PSI beamline BOA using a symmetric TLI-nGI setup with the polychromatic spectrum available at BOA [13]. The open beam visibility

was 50 %. We demagnetized the sample before the measurement in the magnetic yoke used for the measurements. During the measurement H_{app} was cycled from 2750 A m^{-1} to −2750 A m^{-1} and back to 2750 A m^{-1} in non-equidistant steps with an increased step density around 0 A m^{-1} to measure M_R^{DFI} and H_C^{DFI}. For every applied magnetic field (H_{app}), we performed an nGI scan consisting of 10 steps with three images per step, each with an exposure time of 20 s. Hence, every DFI has a total exposure time of 600 s.

We analyzed four different samples made from electrical steel type M330-35A. The size ($L \times W \times T$) of the samples was 60 mm × 40 mm × 0.35 mm. The rolling direction is parallel to the long side of the samples. One non-embossed reference sample (R2), one homogeneously embossed sample across the width of sample (F), one sample with a staggered embossing pattern across the width of sample (G), and one sample homogeneously embossed across 50 % of the sample width (H). The embossing consisted of multiple pyramidal indentations made with an applied force of 100 N. General sample parameters are provided in Sec. 4.4. A sketch of the sequential embossing process is shown in Fig. 4.9 c). In Fig. 5.15, the embossing patterns of the four considered samples R2, F, G, and H are shown.

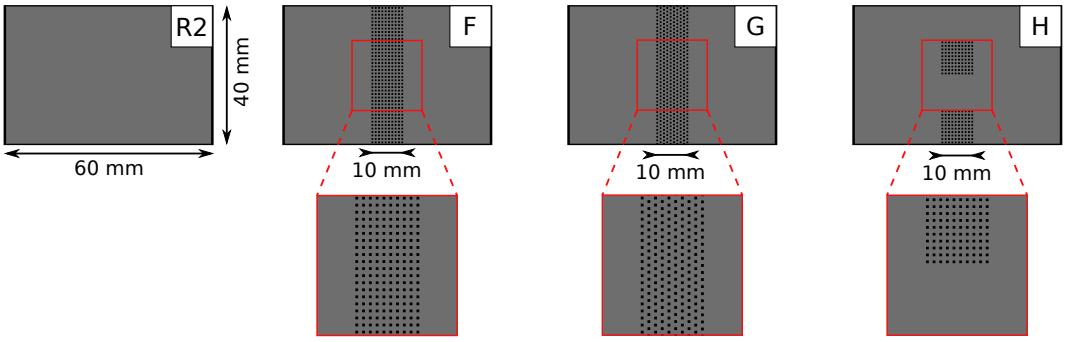

Figure 5.15.: Sketch of the embossing patterns of the four samples considered in Sec. 5.5. A sketch of the embossing process employed for samples F-H is shown in Fig. 4.9 c). General sample parameters are presented in Sec. 4.4.

5.5.3. Magnetic hysteresis in quasi-static magnetic fields

Fig. 5.16 shows the DFI at 49 A m^{-1} of a) the reference sample, b) the homogeneous, c) the staggered embossing pattern and d) the sample with a flux barrier used to analyze the influence of embossing induced residual stress on the DFI hysteresis curve. For the three embossed samples (F-H), the DFI signal decreases significantly in the embossed areas compared to the non-embossed area. In the case of samples F and G, the DFI signal decreases to 0.28, while the signal in sample H decreases to 0.24.

In sample H, we also observe an increase in the DFI signal between the embossed flux barriers. Fig. 5.16 e) shows the DFI signal hysteresis of different areas marked in the DFI in a)- d). As noted before, the DFI signal maps USANS in a sample, which relates non-linearly to the absolute value of the polarization. Similarly, a polarization of zero results in a sample parameter dependent (thickness, grain size, and residual stress) non-zero DFI value. Hence the hysteresis curves shown in Fig. 5.16 e) take on a distinct wing shape, where the DFI signal shows significant change at low absolute H_{app} values and less change at higher absolute H_{app} values. The "wing" shape changes slightly depending on the residual stress state in and around the considered area. The hysteresis loop starts at $H_{\mathrm{app}} = 2750\,\mathrm{A\,m^{-1}}$. Arrows indicate the direction of the hysteresis curve. Please note that the direction of positive and negative H_{app} has been chosen arbitrarily but is consistent between the samples.

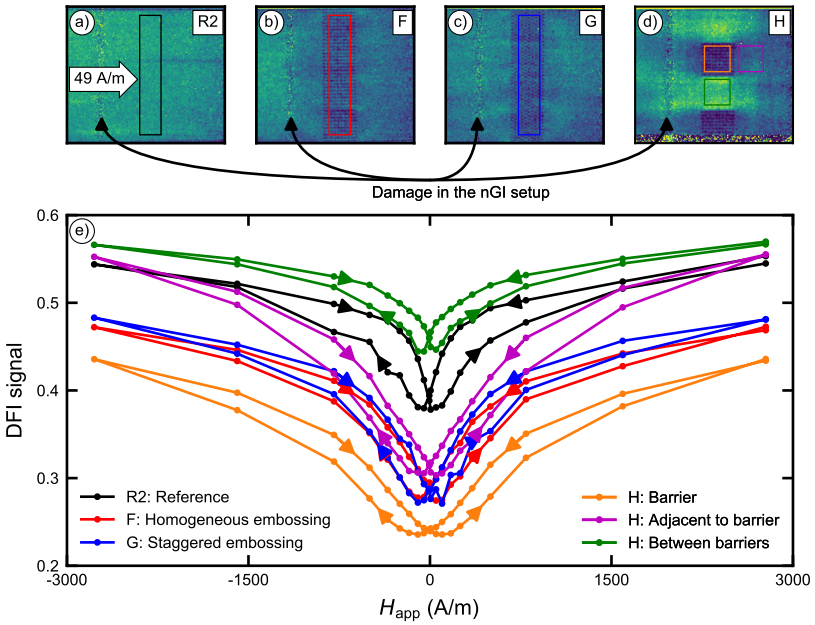

Figure 5.16.: a)-d) DFI signal of the reference sample R2 as well as the embossed samples F-H at $H_{app} = 49\,\mathrm{A\,m^{-1}}$. The black arrows point to an area with a defect in a grating of the nGI-setup. This damage leads to the distorted signal. e) Magnetic hysteretic behavior of the DFI signal of the marked areas in a)- d). Due to induced residual stress, the DFI signal of the two embossed samples F (red) and G (blue), is constantly lower than the reference sample (black), indicating smaller magnetic domains. There is no significant change in signal between the different embossing strategies in samples F and G. The barriers in sample H (orange) have a similar stress state as the embossed areas in samples F and G. However, the possibility of the magnetic flux to avoid the embossed area significantly reduces the DFI signal in this area but increases the signal between the flux barriers (green). In the area adjacent to the embossing (magenta), the signal varies between the full-width embossing at low H_{app} and the reference at high H_{app}.

For a better comparison, the parameters defined in Fig. 5.15 are collected in table 5.2. For all considered areas, the hysteresis is, as expected, axially symmetric around $H_{app} = 0\,\mathrm{A\,m^{-1}}$. Hence, positive and negative H_{app} are interchangeable unless specifically noted. The residual stress in the two samples, F and G, increases the coercivity as well as decreases the overall DFI signal, i.e., lower M_R^{DFI}, DFI_{max} and DFI_{min} compared to the reference sample R2. Additionally, the ratio $\frac{DFI_{max}}{DFI_{min}}$ increases from 1.4 in the reference sample to 1.68 (1.73) in the homogeneous (staggered) embossed area of sample F (G), respectively. H_C^{DFI} increases to $98\,\mathrm{A\,m^{-1}}$ ($98\,\mathrm{A\,m^{-1}}$) in the homogeneous (staggered) embossed area in the samples F (G) from $79\,\mathrm{A\,m^{-1}}$ in the reference R2. As the difference in DFI signal between the homogeneous (red) and the staggered

Sample name	M_R^{DFI} **(arb. u.)**	H_C^{DFI} **(A m^{-1}**	DFI_{max}**(arb. u.)**	DFI_{min}**(arb. u.)**	P^{DFI}**(arb. u.)**
Reference	0.391	79	0.54	0.384	104.5
Homogeneous	0.287	98	0.47	0.279	99.2
Staggered	0.285	99	0.48	0.277	99.7
Barrier	0.24	109	0.43	0.235	99.1
Between barriers	0.458	81	0.57	0.453	57.2
Adjacent barrier	0.313	98	0.55	0.305	128.5

Table 5.2.: Remanence M_R^{DFI},coercivity H_C^{DFI}, DFI_{max} and DFI_{min} of the areas marked in Fig.5.16.

(blue) embossing is minimal, the influence of the embossing pattern, in this case, is minimal.

In contrast, the barrier (orange) in the sample (H) d) shows a smaller DFI signal at the same magnetic flux than the fully embossed samples (F and G). Hence, $M_R^{DFI} = 0.24$ is slightly lower than the corresponding values for the homogeneous $M_R^{DFI} = 0.29$ and the staggered $M_R^{DFI} = 0.28$ embossing. Similarly, DFI_{max} and DFI_{min} of the barrier are lower than the corresponding values in the embossing. The $\frac{DFI_{max}}{DFI_{min}}$ ratio is 1.82, slightly higher than for the embossing. Here H_C^{DFI} increases to 109 A m^{-1}

The area between the barriers (green) in sample H, indicated in Fig. 5.16, shows an increased DFI signal compared to the reference. At $H_{app} = 49$ A m^{-1} the difference is 0.12, which decreases to 0.07 at $H_{app} = 2750$ A m^{-1}. Here $M_R^{DFI} = 0.46$ is higher than in the reference sample, while $H_C^{DFI} = 50$ A m^{-1} does not change compared to the reference R2. The $\frac{DFI_{max}}{DFI_{min}}$ ratio is reduced to 1.26. In contrast to the embossed areas H_C^{DFI} remains nearly constant compared to the reference at 81 A m^{-1}

The area adjacent to the embossing in sample H (magenta) shows a decreased DFI signal at $H_{app} < 2750$ A m^{-1} compared to the reference, while at $H_{app} = 2750$ A m^{-1} the DFI signal of the adjacent area is at the same level or slightly above the reference $DFI_{max} = 0.55$. Together with a $DFI_{min} = 0.3$, this results in a ratio of 1.8, which is the largest of all analyzed areas. Similarly, M_R^{DFI} and H_C^{DFI} are between the values found for the reference and the embossed areas. M_R^{DFI} (H_C^{DFI}) is reduced (increased) to 0.31 (98 A m^{-1}), respectively.

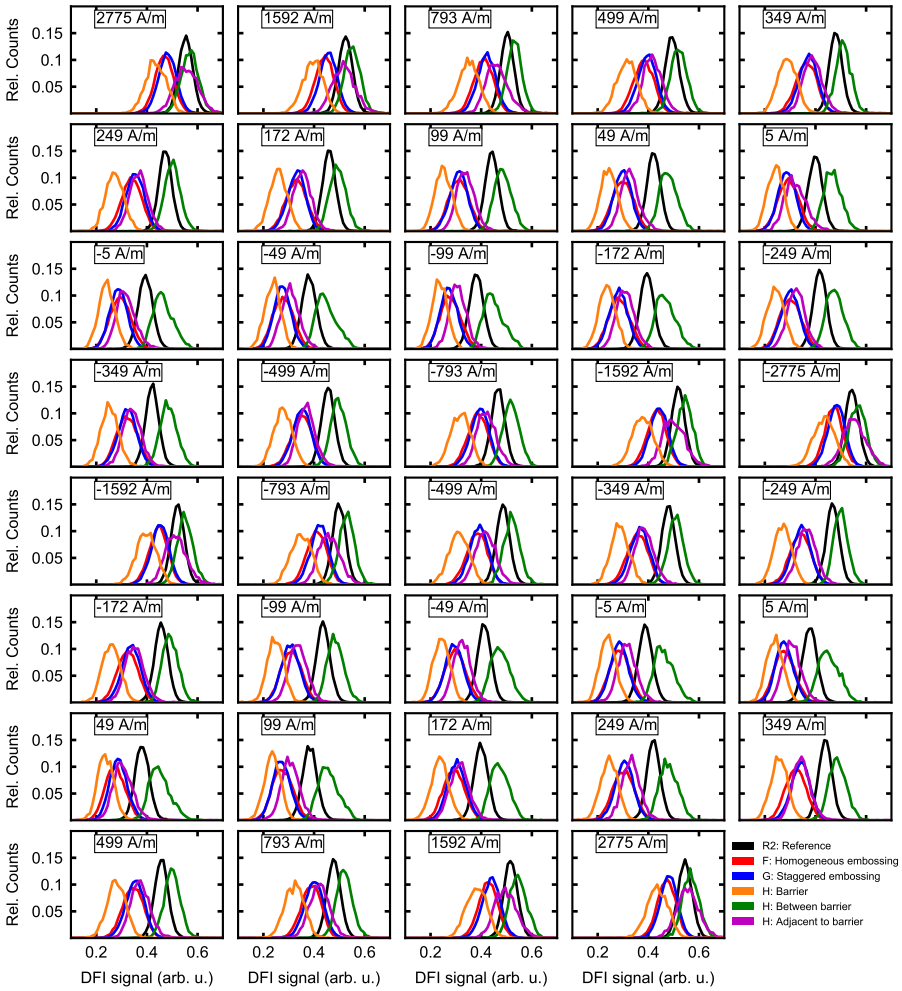

Figure 5.17.: Histograms of the DFI signal of the homogeneous (red), staggered (blue) embossed barrier (orange), between barriers (green), adjacent to a barrier (magenta) and reference (black) areas in ES samples at applied magnetic fields H_{app} used in the hysteresis scan presented in Fig. 5.16. As expected, the histogram of the homogeneous, staggered embossed and barrier area shifts toward lower DFI signals than the reference sample. The barrier area shows the lowest DFI signals and little histogram overlap with the reference, indicating a better magnetic flux deflection than in the homogeneous and staggered embossed area. In addition, the histograms of the embossed samples are broadened compared to the reference but do not show a dual peak, which we would expect if the influence of the embossing points is restricted to the deformed area.

As the DFI in Fig. 5.16 a)-d) indicates an inhomogeneous distribution of DFI signal in the embossed area; we will use the histogram of the evaluated areas for further analysis. The histograms for the different applied H_{app} are presented in Fig. 5.17. The colors of the histograms correspond to the colors used to mark the areas in Fig. 5.16 a)-d). All histograms were scaled to the areas of the regions indicated. The histograms are ordered from top left to bottom right, following the hysteresis measurement, starting at $H_{\text{app}} = 2750\,\text{A}\,\text{m}^{-1}$.

Regardless of H_{app} and considered area, the histogram of each area shows a single peak. The position of this peak corresponds to the mean DFI signal plotted in Fig. 5.16 e). At high H_{app}, the peaks of all areas tend to overlap while separating at H_{app} close to zero, indicating a decreased impact of residual stress at high H_{app}. We also note that for all H_{app}, the full width at half maximum (FWHM) of the histogram of the reference is smaller than the FWHM of the histograms of the other areas. Fig. 5.18 presents, a) the overlap of the area below the histogram with the reference during the hysteresis and b) the FWHM of the histograms. The FWHM of the histogram corresponds to the homogeneity of the signal in the area, related to the homogeneity of the magnetic flux distribution in the area. The overlap of the non-reference histograms with the reference histogram indicates the difference in size of magnetic domains for the considered areas, which correlates with the polarization in this area.

As expected, the overlap is small for the homogeneously (staggered) embossed area in sample F (G), rising from roughly 10 % at $H_{\text{app}} = 0\,\text{A}\,\text{m}^{-1}$ to 25 % (31 %) at $H_{\text{app}} = 2750\,\text{A}\,\text{m}^{-1}$. The rise of overlap is not linear but has a significant jump at roughly $500\,\text{A}\,\text{m}^{-1}$ and remains relatively constant afterward. In contrast, the overlap of the barrier (orange) starts at 2 % at $H_{\text{app}} = 0\,\text{A}\,\text{m}^{-1}$ and rises quite linearly to 11 % at $H_{\text{app}} = 2750\,\text{A}\,\text{m}^{-1}$, indicating less magnetic flux in the barrier than in the homogeneous and staggered embossing.

The overlap of the area adjacent to the embossing in sample H (magenta) shows its minimum value of 12 % around a value of $H_{\text{app}} = 250\,\text{A}\,\text{m}^{-1}$. Towards $H_{\text{app}} = 0\,\text{A}\,\text{m}^{-1}$ the overlap increases to 25 %. Towards $H_{\text{app}} = 2750\,\text{A}\,\text{m}^{-1}$ the overlap rises asymptotically towards an overlap of 76 %.

Unlike the other areas, the overlap in the area between the two barriers in sample H (green) shows a significant dependence on the previous magnetization state of the sample. In case H_{app} is decreased from a high value, the overlap will first slightly decrease from 70 % at $H_{\text{app}} = 2750\,\text{A}\,\text{m}^{-1}$ to 60 % at $H_{\text{app}} \approx 300\,\text{A}\,\text{m}^{-1}$ and then rapidly decrease towards 26 % around $H_{\text{app}} = 0\,\text{A}\,\text{m}^{-1}$. Increasing H_{app} to $-2750\,\text{A}\,\text{m}^{-1}$ causes a relatively linear rise of overlap back to 70 %. In Fig. 5.18 b), the dependence of the FWHM of the histograms on H_{app} is plotted. As expected, the FWHM of the reference (black) is the smallest and remains constant at roughly 0.062. While for most previously applied analysis methods, the homogeneous (red) and staggered (blue)

embossing showed little difference, this is not the case when analyzing the FWHM of the histogram. Here the staggered embossing has a relatively constant FWHM of around 0.082, while the homogeneous embossing has a distinct maximum of 0.1 around $H_{app} = 0\,A\,m^{-1}$ and decreasing towards 8.5 at $H_{app} = 2750\,A\,m^{-1}$. The barrier (orange) shows a minimum of the FWHM of 0.08 at $H_{app} = 0\,A\,m^{-1}$ with increasing FWHM towards 0.105 at $H_{app} = 2750\,A\,m^{-1}$.

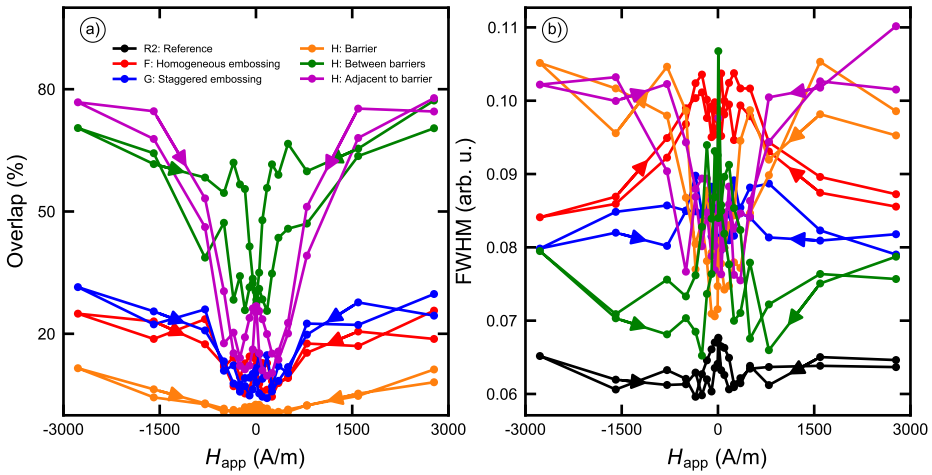

Figure 5.18.: Analysis of a) the overlap of the histograms between an area in an embossed sample with the reference sample and b) the FWHM of the histograms shown in Fig. 5.17. a) shows a strong dependence of the overlap on the previous magnetization state for the area between barriers (green), which is not seen in the other histograms. As expected, the overlap of the embossed areas (red, blue, orange) with the reference is minimal. In the case of the homogeneous and staggered embossed area, there is a jump of overlap around $H_{app} = 500\,A\,m^{-1}$. The area adjacent to the barrier (magenta) also shows little overlap below $H_{app} = 500\,A\,m^{-1}$ but rises rapidly at higher H_{app}. The histogram overlap of the area between the barriers and the reference shows a stronger dependence on the previous magnetization state than the other areas. Here reducing H_{app} from high values leads to a higher overlap than if H_{app} increases from lower values. This trend is shown in Fig. 5.18 a).

Discussion

In the DFI hysteresis measurements shown in Fig. 5.16, the influence of the embossing on the magnetic properties of the sample at different H_{app} are seen. The DFI signal decreases in the embossed area for all three embossed samples, indicating increased scattering, effectively pointing towards decreased magnetic flux and magnetization in this area. Comparing the embossed areas of the fully embossed samples with the

barrier area in the flux barrier sample shows that even though both areas have roughly the same residual stress state, the DFI signal and hence the magnetization is lower in the flux barrier sample. The most probable cause for this difference is the possibility of the magnetic flux deviating towards the non-embossed areas in the flux barrier sample, decreasing the energy in the system. In contrast, in the fully embossed sample, the flux has to go through the embossing (or the surrounding air), causing an increase in magnetization and hence an increase in the DFI signal. The deviation of the magnetic flux towards the non-embossed areas in the flux barrier sample leads to a decrease in scattering in this area, indicating an increase in domain size, effectively showing the possibility of guiding the magnetic flux using multiple small embossing points.
While the hysteresis curves of the different areas show different trends, it is hard to quantify the changed physical constants. As noted before, the hysteresis captured by the DFI signal is not connected linearly with the magnetic polarization usually considered in hysteresis measurements. While it is possible to map the DFI signal to a magnetic polarization by measuring both the DFI signal and the polarization at the same H_{app}, as has been shown by Weiss et al. in [30], this is primarily applicable for perfectly homogeneous (non-embossed) samples. Here the global polarization measurements can be matched to the local DFI signal. While it would be possible to perform this matching process for a fully embossed sample, this method breaks down when considering partially embossed samples, as their underlying magnetic and material properties are not constant over the whole sample. The problems with acquiring local information from global measurements again demonstrate the value of using nGI to map the DFI signal of the sample as it visualizes the influence of inhomogeneous distributed residual stress on the local magnetic polarization.
The embossed areas in samples F-H and the area adjacent to the barrier in sample H show an increase in H_C^{DFI}, indicating that the material has become slightly magnetically harder in these areas. This is expected for the embossed areas, as residual stress may pin magnetic domain walls, increasing the energy necessary for reversal of magnetization [127, 128]. In contrast, the area in sample H adjacent to the embossing has no increase in residual stress. While the coercivity is also dependent on the maximum polarization B of the material, the data suggests that the maximum polarization in the reference and the area adjacent to the embossing are very similar. Hence, we have shown that we track the deviation of magnetic flux due to energy minimization using the DFI signal regardless of the residual stress state. While this effect is significant at low H_{app}, towards high H_{app}, the effect vanishes as the flux barriers are less efficient. As expected, the area between the barriers shows no change in H_C^{DFI}.
The singular peak of the histograms presented in Fig. 5.17 in the embossed areas is slightly unexpected. Visually inspecting the scattering images in 5.16 a)-d), one expects a double peak structure of the histogram. Hence, the magnetic flux in areas between

two indentations of an embossing area is also significantly reduced. We published similar results [111], where we showed that in the case of multiple small indentations comprising an embossed line perpendicular to H_{app}, the indentations themselves show primarily compressive residual stress, while the area between indentations shows tensile residual stress. While the magnitude of these two stress types was very similar, we have shown that similar magnitudes of compressive stress decrease the magnetic permeability more than tensile stress.
The overlap of the histograms of the considered areas with the reference area is shown in Fig. 5.18 a), which measures the effectiveness of the guidance of the magnetic flux. The barrier shows a maximum overlap of 11 % with the reference, indicating the significantly reduced magnetic flux in this area. Interestingly, the homogeneous and staggered areas show a maximum overlap of 25 % and 31 %, respectively. Again, showing that embossing the full width of the sample forces the magnetic flux through the embossed area.
As noted before, the connection between polarization and the DFI signal is non-linear; hence calculating the area of the hysteresis loop described by the DFI signal and trying to estimate the energy loss per cycle results in inconclusive results. The data suggest an increase in energy loss in the reference sample (see Table 5.2) compared to the embossed samples. In contrast, the increase in H_C^{DFI} suggests increased losses in the embossed areas. To successfully extract meaningful information about the local energy losses, we need to reduce the number of non-linear links between the polarization and the measured signal. We have shown in Secs. 5.3 and 5.4 that we can extract information about both the size and the orientation of the magnetic domains using nGI. Hence, performing correlation and anisotropy scans for every probed point of the hysteresis would allow the recovery of the hysteresis of the size of the magnetic domains. As this property is more closely linked to magnetic polarization, extracting more information about the local magnetic hysteresis may be possible. However, such a scanning procedure is quite time-consuming, and a single hysteresis scan would likely take up to a week to perform. For homogeneous materials, another option may be to match the DFI signal and polarization as described in [30]. As explained before, this approach breaks down in inhomogeneous samples.

Conclusion

In this section, we have analyzed the possibility of measuring the local hysteresis of (embossed) electrical steel sheets and extracting physical parameters from the measurements. We were able to recover the local coercivity H_C^{DFI} and remanence M_R^{DFI} from the hysteresis curve. As imaging integrates along the beam axis, this allows to analyze the local magnetic properties in the bulk of a sample. In contrast, recovery of

the energy loss P^{DFI} has proven difficult and likely requires extensive measurement time to gather enough data for a somewhat successful attempt. Matching the DFI signal to the magnetic polarization is only feasible for homogeneous samples or requires significant knowledge about the local magnetic properties, which is difficult to acquire for the bulk of an inhomogeneous sample.
We have further been able to show that the DFI signal of an NGOES sheet is not only dependent on the local residual stress and applied magnetic field but also on the available magnetic flux path. We could visualize the deviation of magnetic flux in a non-embossed area caused by an area adjacent to the residual due to the minimization of energy in the system. A further observation is that the magnetic flux is still significantly deflected from these areas despite significant gaps between the small indentations in the embossing area.
In our measurements, we have analyzed the quasi-static hysteresis. For future measurements, the hysteresis at different frequencies and the resulting differences in DFI signal would be interesting to measure. Furthermore, a variation of embossing point density and embossing force as parameters for enhancing the flux barriers and reducing the deformation of the electrical steel would be interesting.

6 Conclusion and Outlook

The ongoing fight against climate change is a dominating subject in many research fields. In particular, transportation is a significant contributor to the consumption of fossil fuels and the accompanying emission of greenhouse gases. According to the German Environment Agency (Umweltbundesamt), the transportation sector in Germany used, in 2021, 653 TWh of primary energy of which 605 TWh were provided by fossil fuels, i.e., gasoline and diesel. In comparison, the total primary energy usage in Germany was 2407 TWh. Hence switching to battery electric vehicles (BEVs) is one option to significantly reduce the amount of fossil fuel consumed. However, the gravimetric and volumetric energy density of batteries is rather low compared to gasoline, which makes the maximum range without recharging an electric car a major weakness. This problem requires batteries with higher energy densities or more efficient electric vehicles.

In this thesis, we have looked at the latter problem by studying methods to increase the efficiency of the electric drives used in BEV. Electric drives convert electric energy into rotational energy by the interaction of the magnetic field in the drive with the magnetic field generated by the applied electric current. In BEVs typical electrical drive types are synchronous reluctance machines (SynRM) and permanent magnet synchronous machines (PMSM). For an optimum operation of such electric drives, the magnetic flux inside the magnetic core of the drive has to be guided to reduce stray magnetic flux and create a magnetic anisotropy. Conventionally, this guidance is achieved by removing material from the magnetic core. The magnetic core comprises stacked non-grain-oriented electrical steel (NGOES) sheets, a soft magnetic material. The areas removed from the NGOES sheets are called cutouts and reduce the mechanical strength and hence maximum rotational speed of the drive, which is tied to its power density and efficiency.

As part of an interdisciplinary project, we have studied the basic principles of replacing the conventional cutouts to guide the magnetic flux in the magnetic core. As a replacement for cutouts, we use embossing, a local forming process, to introduce residual stress in the material. The interaction between residual stress and magnetic permeability is described by inverse magnetostriction, also called the Villari effect. Residual stress causes a decrease in local magnetic permeability, which displaces the magnetic flux from these regions and concentrates it in other regions. Understanding the displacement of the magnetic flux concerning the introduced embossing is key in enabling the development and simulation of the magnetic core of drives using embossing to guide the magnetic flux.

Neutron grating interferometry (nGI), an advanced neutron imaging technique, can uniquely map the displacement of magnetic flux in the bulk of electrical steel. The size of magnetic domains changes depending on the local magnetization state of the electrical steel, which is determined by the local magnetic flux. The distribution of magnetic domains creates an inhomogeneity in the micrometer regime of the magnetic scattering length density. Variations in the magnetic and nuclear scattering length density cause ultra-small-angle scattering of neutrons (USANS) which nGI detects. Hence, the change in the distribution of magnetic domains and, therefore, the influence of embossing on the magnetic flux can be tracked.

An nGI-setup generates an interference pattern with a micrometer period by introducing a phase-shifting line grating into the neutron beam. USANS degrades this interference pattern. A requirement for interference is spatial coherence. Hence, an absorbing line (source) grating generates coherent neutron beamlets. Often neutron imaging detectors cannot resolve the interference pattern directly. One option is to introduce an additional absorption line (analyzer) grating, with the same period as the interference pattern, into the neutron beam. This grating partially blocks the interference pattern. Moving one of the gratings results in an intensity oscillation in every detector pixel. This intensity oscillation can then be used to map the USANS caused by a sample, as the visibility of the oscillation (ratio of amplitude vs. offset) is reduced by scattering. The visibility is normalized to the reference visibility without a sample to recover the influence of the sample. The resulting map is called the dark field image (DFI).

The line profile of the gratings is also the reason for the single dimensionality of nGI, as only scattering perpendicular to the line profile affects the generated interference pattern. This effect is also called slit-smearing. Therefore, to measure anisotropic scattering, the angle between the sample and gratings has to be varied.

Quantitative analysis of the scattering signal and, therefore, analysis of the size of the scatterer requires probing the characteristic correlation function of the magnetic domains at different correlation lengths. The correlation length is a setup-specific parameter defining the sensitivity to a specific scattering angle of the neutrons. This parameter can be tuned by varying the placement of the sample with respect to the gratings or by adjusting the incoming neutron wavelength. With increasing correlation length, the correlation function decreases, with the trend of this decrease containing information about the size of the scatterer.

By applying nGI to NGOES with different residual stress states and applied magnetic fields, we verified the suitability of nGI as a means to detect the effect of residual stress on the distribution of magnetic domains. We further showed that residual stress introduced by embossing is the primary cause of the change in magnetic domains, not the pure deformation of the material.

A critical influence on the energy loss in the magnetic core of an electric drive is

the presence of inadvertent residual stress caused by inadequate localization of the introduced residual stress. Here, we showed that a sharp deformation is preferred over a gradual process. However, a single sharp deformation also results in a global deformation of the electrical steel. This deformation causes additional loss in an electric drive as gaps when stacking NGOES in the magnetic core also increase losses. Therefore, we found multiple small embossing points as an optimum for redirecting the magnetic flux and reducing global deformation.

These qualitative results can already be used to validate material and magnetic simulations of electrical steel necessary to optimize electric drives. However, a quantitative analysis of the distribution and orientation of magnetic domains will allow us to refine the simulations. Accordingly, by probing the correlation function of the magnetic domains at different correlation lengths, we extracted spatially resolved quantitative information about the distribution of magnetic domains. We compared two approaches: i) assuming a simple model of isolated spheres and ii) a model based on the scattering by misaligning the spins. While both models show good agreement between raw data and theory, the model based on isolated spheres shows slightly better agreement. This model contains no information about the underlying magnetic interactions of the material and only considers the average diameter of the magnetic domains and its variance. Still, we were able to map the change in the diameter of the magnetic domains vs. the applied magnetic field and the residual stress. Hence allowing for the first time to visualize the local change of the magnetic domains.

In contrast to the model based on isolated spheres, the model based on misaligned spins considers more magnetic properties, such as the exchange stiffness constant or the range of spin-misalignment perturbations. This link to more parameters proved challenging during the fitting process. The exponential decay of the correlation function has no characteristic features, such as minima or maxima helping to define the optimum parameters. In combination with the increased number of parameters, the fit becomes relatively unstable.

We assumed spherical magnetic domains for the quantitative analysis to stabilize the fit. However, analysis of the anisotropy of the scattering shows that, on average, the magnetic domains are slightly elongated towards the rolling direction of the electrical steel and the magnetization direction.

The quality of NGOES is typically defined by analyzing the global magnetic hysteresis of the material using single-sheet-testers or Epstein frames. Similar to these global measurements, we analyzed the local change of the magnetic hysteresis with residual stress induced by embossing. From this, we extract the local coercivity and remanence from the bulk of the sample. Directly extracting the magnetic polarization from the DFI signal is not trivial and requires extensive knowledge about the magnetic properties, which are difficult to access for inhomogeneous samples.

The successful analysis of the results presented above required an improvement of the nGI-setup and a deep understanding of the limitations present during measurements. As a result, we completely rebuilt the nGI-setup used at ANTARES. We significantly increased the performance of the nGI-setup by adapting its geometry and changing the manufacturing method of the source and analyzer gratings. The new nGI-setup allows unprecedented performance by increasing the visibility of the intensity oscillation near its theoretical limit. In addition, we also increased the range of accessible correlation lengths. Both of these adaptations were vital for successfully quantifying the magnetic domain size in NGOES.

Understanding the various artifacts appearing in the evaluated data further required an analysis of the limitations inherent to nGI. Particularly for the quantitative measurements, which we have performed, this knowledge is key. As outlined, the signal measured during an nGI-scan is an intensity oscillation. This oscillation typically takes the form of a (co)sine curve. Scattering decreases the visibility of the oscillation. Strongly scattering samples and high correlation lengths may lead to a suppression of the visibility towards zero.

However, the Poisson distribution inherently governs the detection process of neutrons, i.e., there are always variations in the measured intensity even if there is no change in the incoming neutron flux. The standard deviation of the variation depends on the number of neutrons counted. This inherent variation in the measured intensity causes the appearance of a minimum visibility, regardless of scattering, during the evaluation of the intensity oscillation. Combined with the reference visibility, we can define a minimum accessible DFI value. Together with previous results, this allows for the first time to define a neutron count-dependent dynamic DFI range in which quantitative measurements are possible. The knowledge about the dynamic range allowed us to optimize the analysis of the distribution of magnetic domains. It will allow us to precisely plan the required measurement time and neutron fluence for samples, enabling to optimize the use of limited beamtime.

As a primary result of this thesis, we have shown that nGI is a uniquely capable technique that can help develop new electric drives, complementing standard measurement methods. For the first time, nGI has been used to directly gather spatially resolved information about the distribution and orientation of magnetic domains in the bulk of a sample. Quantitative measurements with increased statistics and data point density will allow the extraction of more precise information in the future. Combining anisotropy measurements with scans of the correlation length on embossed samples will allow us to track the change in the size and shape of magnetic domains and the resulting magnetic flux under applied magnetic fields.

A secondary result of this work was the signifcant improvement of nGI as a technique and the increased understanding of the contribution of noise to measurements. We

must emphasize that the approach shown is not limited to NGOES and its use in electric drives but is viable for most ferromagnetic materials. Hence, nGI is a valuable addition when analyzing the magnetic properties of inhomogeneous polycrystalline ferromagnetic samples.

List of publications

1. **High-resolution Bragg-edge neutron radiography detects grain morphology in PBF-LB/M IN718**
   Serrano-Munoz I., Pfretzschner B., Kromm A., Nadammal N., Kardjilov N., Markötter H., Neuwirth T., Schulz M., Griesche A.
   Materialia 30, 101827 (2023)

2. **Signal Retrieval from Non-Sinusoidal Intensity Modulations in X-ray and Neutron Interferometry Using Piecewise-Defined Polynomial Function**
   Pinzek, S., Gustschin, A., Neuwirth, T., Backs, A., Schulz, M., Herzen, J., Pfeiffer, F.
   J. Imaging 7, 209 (2021)

3. **Analysis of Cylindrically and Spherically Embossed Flux Barriers in Non-oriented Electrical Steel.**
   Gilch, I., Vogt, S., Neuwirth, T., Schauerte, B., Hameyer, K., Schulz, M., Gustschin, A. Volk, W., Weiss, H. A.
   In: Daehn, G., Cao, J., Kinsey, B., Tekkaya, E., Vivek, A., Yoshida, Y. (eds) Forming the Future. The Minerals, Metals & Materials Series. Springer, Cham (2021)

4. **An investigation on the suitability of modern nondestructive testing methods for the inspection of specimens manufactured by laser powder bed fusion**
   Kolb, C.G., Zier, K., Grager, JC., Bachmann, A., Neuwirth, T., Schmid, S., Haag, M., Axtner, M., Bayerlein. F., Grosse, C.U., Zaeh, M.F.
   SN Appl. Sci. 3, 713 (2021)

5. **Alternative Magnetflussführung in Elektromotoren**
   Schauerte, B., Gilch, I., Neuwirth, T., Sebold. S., Leuning, N., Schulz, M., Volk, W., Hameyer, K.
   Forsch Ingenieurwes 85, 827-836 (2021)

6. **Impact of residual stress evoked by pyramidal embossing on the magnetic material properties of non-oriented electrical steel**
   Gilch, I., Neuwirth, T., Schauerte, B. Leuning, N., Sebold. S., Hameyer, K., Schulz, M., Volk, W.
   Arch Appl Mech 91, 35133526 (2021)

7. **Comparison of Thermal Neutron and Hard X-ray Dark-Field Tomography**
   Gustschin, A., Neuwirth, T., Backs, A., Viermetz, M., Gustschin, N., Schulz, M., Pfeiffer, F.
   J. Imaging 7, 1 (2021)

8. **Light Yield Response of Neutron Scintillation Screens to Sudden Flux Changes**
   Neuwirth, T., Walfort, B., Sebold, S., Schulz, M.
   J. Imaging 6, 134 (2020)

9. **The influence of residual stress on flux-barriers of non-oriented electrical steel**
   Schauerte, B., Leuning, N., Vogt, S., Moll, I., Weiss, H.A., Neuwirth, T., Schulz, M., Volk, W., Hameyer, K.
   Journal of Magnetism and Magnetic Materials 504, 166659 (2020)

10. **A high visibility Talbot-Lau neutron grating interferometer to investigate stress-induced magnetic degradation in electrical steel**
    Neuwirth, T., Backs, A., Gustschin, A., Vogt, S., Pfeiffer, F., Böni, P., Schulz, M.
    Sci Rep 10, 1764 (2020)

11. **Origin of Pseudo-Variation in High Resolution Neutron Grating Interferometry**
    Neuwirth, T., Schulz, M., Böni P,
    Materials Research Proceedings 15, 129-135 (2020)

12. **Evaluation of the interdependency of mechanical cutting and magnetic anisotropy on the magnetic properties of FeSi electrical steel**
    Leuning, N., Steentjes, S., Weiss, H. A., Volk, W., Schulz, M., Neuwirth, T., Hameyer, K.
    Organ 7, 19 (2019)

13. **Extent of embossing-related residual stress on the magnetic properties evaluated using neutron grating interferometry and single sheet test**
    Vogt, S., Neuwirth, T., Schauerte, B. Weiss, H.A., Falger, P.M., Gustschin, A., Schulz, M., Hameyer, K., Volk, W.
    Prod Eng Res Devel 13, 211217 (2019)

14. **Neutron grating interferometry investigation of punching-related local magnetic property deteriorations in electrical steels**

Weiss, H. A., Steentjes, S., Tröber, P., Leuning, N., Neuwirth, T., Schulz, M., Hameyer, K., Golle, R., Volk, W.
Journal of Magnetism and Magnetic Materials 474, 643-653 (2019)

15. **Rapid electrolyte wetting of lithium-ion batteries containing laser structured electrodes: in situ visualization by neutron radiography**
Habedank, J.B., Günter, F.J., Billot, N. Gilles, R., Neuwirth, T., Reinhart, G., Zaeh, M.F.
Int J Adv Manuf Technol 102, 27692778 (2019)

16. **Fabrication of gadolinium particle-based absorption gratings for neutron grating interferometry**
Gustschin, A., Neuwirth, T., Backs, A., Schulz, M., Pfeiffer, F.
Review of Scientific Instruments 89, 103702 (2018)

17. **Introduction to electrochemical impedance spectroscopy as a measurement method for the wetting degree of lithium-ion cells**
Günter, F. J., Habedank, J. B., Schreiner, D., Neuwirth, T., Gilles, R., Reinhart, G.
J. Electrochem. Soc., 165 (14), A3249 (2018)

Acknowledgment / Danksagung

Die Doktorarbeit wäre ohne die Unterstützung vieler Personen gar nicht möglich gewesen. Einen großen Dank an alle, die diese Arbeit überhaupt erst möglich gemacht haben. An dieser Stelle möchte ich mich bei einigen noch besonders bedanken.

Prof. Peter Böni

Lieber Peter, vielen Dank für die Möglichkeit diese interessante Forschungsarbeit durchzuführen. Ich bin dir unglaublich dankbar, dass du mir die letzten Jahre alle Freiräume gelassen hast, selbst zu forschen, und trotzdem mir immer die Tür für Diskussionen offen gehalten hast. Vielen Dank für dieses Vertrauen.

Michael Schulz

Lieber Michi, vielen Dank, dass du mich die ganzen Jahre unterstützt hast. Es waren ja nicht nur die Jahre während der Doktorarbeit, sondern auch schon vorher während des Studiums. Du hast mich ja erst so richtig an Neutronenbildgebung und nGI herangeführt. Insbesondere ein großer Dank für deine ständige Bereitschaft über Messzeiten, Messergebnisse und Probleme zu diskutieren. Ein besonderer Dank auch für die Korrektur der Arbeit. Die Zusammenarbeit mit dir hat mir unglaublich viel Spaß gemacht.

Simon Sebold

Lieber Simon, vielen Dank für die Zusammenarbeit, die Hilfe und die vielen Diskussionen über Elektrobleche und nGI. Die Diskussionen mit dir haben mir immer sehr geholfen die doch manchmal frustrierenden Ergebnisse zu verstehen. Danke auch für die ganzen nicht-wissenschaftlichen Diskussionen, die wir als Bürokollegen geführt haben. Das hat den Arbeitsalltag immer aufgelockert. Danke für das Messen der Hysteresedaten am PSI.

Alex Backs

Liebe Alex, vielen Dank an dich für die vielen Diskussionen über Magnetismus, die wir während einer gemütlichen Tasse Tee geführt haben. Das hat mir unbglaublich geholfen, meine Ergebnisse besser zu verstehen. Ein großer Dank für den Vorschlag zur Modellierung der magnetischen Domänen, auch wenn ich das Modell jetzt nicht Elmar-Modell wie von dir vorgeschlagen genannt habe.

Ines Gilch, Benedikt Schauerte & Simon Vogt

Vielen Dank für die Zusammenarbeit am SPP 2013 Projekt der DFG. Ihr habt mir einiges über die mechanischen und globalen magnetischen Eigenschaften von Elektroblech beigebracht. Unsere Telcos zum Projekt waren fast immer ein sehr vergnüglicher Einblick in andere Wissenschaftsgebiete.

Imaging-Gruppe + MEDAPP

Vielen Dank an das gesamte Team bei ANTARES, NECTAR und MEDAPP für die immer vorhandene Unterstützung von euch allen, ihr habt viel dazu beigetragen, dass die Arbeit an der Doktorarbeit viel Spaß gemacht hat und ich mich nie allein gefühlt habe. Danke für die Hilfe bei den verschiedensten technischen und physikalischen Problemen, die witzigen Diskussionen, Tipps und Lebensweisheiten die ihr mir alle mitgegeben habt.

(Kaffee) Mate-Runde

Danke an euch alle für die entspannten, lustigen und lehrreichen Diskussionen während der Mittagspause. Außerdem danke für die Lebensweisheiten und die Hilfe bei so manchen Problemen. Danke für das fleissige wegfuttern meines mitgebrachten Kuchens.

FRM II

Danke auch an alle Kollegen des FRM II die indirekt zu meiner Arbeit beigetragen haben. Ein Dank an die Werkstätten für die (manchmal kurzfristige) Fertigung von Probenhaltern, Teilen für das nGI und anderen Kleinteilen. Hoffentlich hört die jetzt schon lange andauernde Neutronenflaute auch bald wieder auf.

Meine Familie

Vielen Dank an euch alle, dass ihr mir immer mit Rat und Tat zur Seite gestanden seid und ihr mich immer bei meinem doch längeren Weg bis hier unterstützt habt.

This work was supported by the Deutsche Forschungsgemeinschaft (DFG) in the DFG priority program "SPP2013 Focused Local Stress Imprint in Electrical Steel as Means of Improving the Energy Efficiency"—HA 4395/22-1; SCHU 3227/2-1; VO 1487/31-1.

A Appendix

Differential neutron flux in ANTARES

Estimation of the noise in the neutron imaging detector requires a precise knowledge about the incoming differential neutron flux. One way to acquire this information is by performing Time of Flight measurements of the spectrum of the neutron flux. In the past an absolute measurement of the differential neutron flux was performed by Lorenz et al. [129]. However, these measurements were performed before the relocation of the ANTARES instrument from beamport SR4b to SR4a [87] and hence a different collimation system and incoming neutron spectrum. Unfortunately, information required to recalculate the spectrum for the upgraded ANTARES instrument is not included in the paper. Due to the continuing reactor shutdown and the damage and subsequent removal of the cold source [130], it is also not possible to measure the neutron spectrum available during the measurements in this thesis. Hence, an alternative method of calculating the differential neutron spectrum is used. The relative differential spectrum of ANTARES at SR4a was measured in [95] (See Fig. 4.2 b)). By dividing the total neutron flux acquired by gold foil measurements [94] by the integral of the spectrum, we get a correction factor for the relative spectrum. The resulting differential neutron flux is presented for L/D = 250 (black) and 500 (red) in Fig. A.1 a). L/D = 250 corresponds to a collimator diameter $D_C = 36.68\,\text{mm}$ and a $L_{CS} = 9170\,\text{mm}$, which was used for the measurements presented in this thesis. In Fig. A.1 b) the neutron flux per selected wavelength after the neutron velocity selector is presented. At $\lambda = 3\,\text{Å}$ the bandwidth of the selector changes from $\frac{\Delta\lambda}{\lambda} = 20\,\%$ ($\lambda \leq 3\,\text{Å}$) to $\frac{\Delta\lambda}{\lambda} = 10\,\%$ ($\lambda \geq 3\,\text{Å}$). For this thesis, the measurements at ANTARES were performed at $\lambda = 4\,\text{Å}$, with a neutron flux of $1 \times 10^7\,\text{s}^{-1}\,\text{cm}^{-2}$.

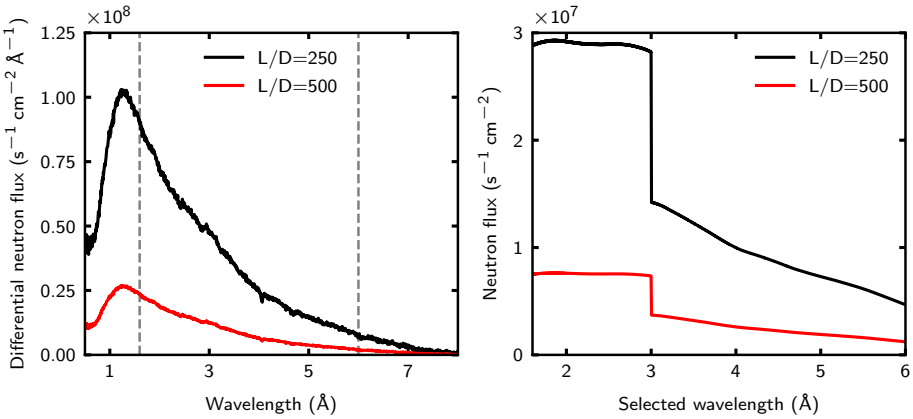

Figure A.1.: a) Differential neutron flux for the collimation ratios L/D = 250 (black) and 500 (red). The dashed gray lines indicate the wavelength range accessible by the neutron velocity selector at ANTARES. b) Neutron flux for L/D = 250 (black) and 500 (red) after the selector. The jump at 3 Å is caused by the two different operation regimes of the selector. For $\lambda \leq 3$ Å the selector has a bandwidth $\frac{\Delta\lambda}{\lambda} = 20\,\%$ and for $\lambda \geq 3$ Å a bandwidth $\frac{\Delta\lambda}{\lambda} = 10\,\%$.

Bibliography

[1] P. B. Reddy, A. M. El-Refaie, S. Galioto, and J. P. Alexander, Design of synchronous reluctance motor utilizing dual-phase material for traction applications, IEEE Transactions on Industry Applications **53**, 1948 (2017).

[2] D. Gerada, A. Mebarki, N. L. Brown, C. Gerada, A. Cavagnino, and A. Boglietti, High-speed electrical machines: Technologies, trends, and developments, IEEE transactions on industrial electronics **61**, 2946 (2013).

[3] R. M. Bozorth, *Ferromagnetism* (1993).

[4] C. Babetto, G. Bacco, and N. Bianchi, Synchronous reluctance machine optimization for high-speed applications, IEEE Transactions on Energy Conversion **33**, 1266 (2018).

[5] F. Chai, Y. Li, P. Liang, and Y. Pei, Calculation of the maximum mechanical stress on the rotor of interior permanent-magnet synchronous motors, IEEE Transactions on Industrial Electronics **63**, 3420 (2016).

[6] H. Naumoski, A. Maucher, and U. Herr, Investigation of the influence of global stresses and strains on the magnetic properties of electrical steels with varying alloying content and grain size, in *2015 5th International Electric Drives Production Conference (EDPC)* (IEEE, 2015) pp. 1–8.

[7] S. Tumanski, *Handbook of magnetic measurements* (CRC press, 2016).

[8] A. Hubert and R. Schäfer, *Magnetic domains: the analysis of magnetic microstructures* (Springer Science & Business Media, 2008).

[9] F. Bitter, On inhomogeneities in the magnetization of ferromagnetic materials, Physical review **38**, 1903 (1931).

[10] J. Kerr, XLIII. On rotation of the plane of polarization by reflection from the pole of a magnet, The London, Edinburgh, and Dublin Philosophical Magazine and Journal of Science **3**, 321 (1877).

[11] T. Reimann, S. Muehlbauer, M. Schulz, B. Betz, A. Kaestner, V. Pipich, P. Böni, and C. Grünzweig, Visualizing the morphology of vortex lattice domains in a bulk type-II superconductor, Nature communications **6**, 1 (2015).

[12] C. G. Kolb, K. Zier, J.-C. Grager, A. Bachmann, T. Neuwirth, S. Schmid, M. Haag, M. Axtner, F. Bayerlein, C. U. Grosse, *et al.*, An investigation on the suitability of modern nondestructive testing methods for the inspection of specimens manufactured by laser powder bed fusion, SN Applied Sciences **3**, 1 (2021).

[13] M. Bacak, J. Valsecchi, J. Čapek, E. Polatidis, A. Kaestner, A. Arabi-Hashemi, I. Kruk, C. Leinenbach, A. Long, A. Tremsin, *et al.*, Neutron dark-field imaging applied to porosity and deformation-induced phase transitions in additively manufactured steels, Materials & Design **195**, 109009 (2020).

[14] A. Michels, Magnetic small-angle neutron scattering of bulk ferromagnets, Journal of Physics: Condensed Matter **26**, 383201 (2014).

[15] D. Mettus and A. Michels, Small-angle neutron scattering correlation functions of bulk magnetic materials, Journal of Applied Crystallography **48**, 1437 (2015).

[16] L. Landau and E. Lifshitz, On the theory of the dispersion of magnetic permeability in ferromagnetic bodies, in *Perspectives in Theoretical Physics* (Elsevier, 1992) pp. 51–65.

[17] W. Döring, Mikromagnetismus, in *Ferromagnetism/Ferromagnetismus* (Springer, 1966) pp. 341–437.

[18] H. Kronmuller, H. Kronmüller, and M. Fähnle, *Micromagnetism and the microstructure of ferromagnetic solids* (Cambridge university press, 2003).

[19] C. Herring and C. Kittel, On the theory of spin waves in ferromagnetic media, Physical Review **81**, 869 (1951).

[20] C. Kittel, Physical theory of ferromagnetic domains, Reviews of modern Physics **21**, 541 (1949).

[21] M. Brooks and D. Goodings, Spin-wave theory of the magnetocrystalline anisotropy in gadolinium metal, Journal of Physics C: Solid State Physics **1**, 1279 (1968).

[22] M. Colarieti-Tosti, S. Simak, R. Ahuja, L. Nordström, O. Eriksson, D. Åberg, S. Edvardsson, and M. S. Brooks, Origin of magnetic anisotropy of Gd metal, Physical review letters **91**, 157201 (2003).

[23] W. F. Brown, *Magnetoelastic interactions*, Vol. 9 (Springer, 1966).

[24] E. Schlömann, Properties of magnetic materials with a nonuniform saturation magnetization. II. Longitudinal susceptibility, Journal of Applied Physics **38**, 5035 (1967).

[25] K. L. Metlov and A. Michels, Third-order effect in magnetic small-angle neutron scattering by a spatially inhomogeneous medium, Physical Review B **91**, 054404 (2015).

[26] J. Weissmüller, A. Michels, J. Barker, A. Wiedenmann, U. Erb, and R. Shull, Analysis of the small-angle neutron scattering of nanocrystalline ferromagnets using a micromagnetics model, Physical Review B **63**, 214414 (2001).

[27] A. Aharoni *et al.*, *Introduction to the Theory of Ferromagnetism*, Vol. 109 (Clarendon Press, 2000).

[28] D. S. Sivia, *Elementary scattering theory: for X-ray and neutron users* (Oxford University Press, 2011).

[29] G. L. Squires, *Introduction to the theory of thermal neutron scattering* (Courier Corporation, 1996).

[30] H. Weiss, S. Steentjes, P. Tröber, N. Leuning, T. Neuwirth, M. Schulz, K. Hameyer, R. Golle, and W. Volk, Neutron grating interferometry investigation of punching-related local magnetic property deteriorations in electrical steels, Journal of Magnetism and Magnetic Materials **474**, 643 (2019).

[31] T. Krouglov, I. M. De Schepper, W. G. Bouwman, and M. T. Rekveldt, Real-space interpretation of spin-echo small-angle neutron scattering, Journal of applied crystallography **36**, 117 (2003).

[32] D. Honecker and A. Michels, Theory of magnetic small-angle neutron scattering of two-phase ferromagnets, Physical Review B **87**, 224426 (2013).

[33] A. Michels, S. Erokhin, D. Berkov, and N. Gorn, Micromagnetic simulation of magnetic small-angle neutron scattering from two-phase nanocomposites, Journal of magnetism and magnetic materials **350**, 55 (2014).

[34] J. S. Pedersen, Analysis of small-angle scattering data from colloids and polymer solutions: modeling and least-squares fitting, Advances in colloid and interface science **70**, 171 (1997).

[35] A. Michels, R. Viswanath, J. Barker, R. Birringer, and J. Weissmüller, Range of magnetic correlations in nanocrystalline soft magnets, Physical review letters **91**, 267204 (2003).

[36] J. Weissmüller, A. Michels, D. Michels, A. Wiedenmann, C. Krill III, H. Sauer, and R. Birringer, Spin structure of nanocrystalline terbium, Physical Review B **69**, 054402 (2004).

[37] A. Michels, Correlation functions of the spin misalignment in magnetic small-angle neutron scattering, Physical Review B **82**, 024433 (2010).

[38] H. Z. Bilheux, R. McGreevy, and I. S. Anderson, *Neutron Imaging and Applications: A Reference for the Imaging Community* (Springer, 2009).

[39] V. F. Sears, Neutron scattering lengths and cross sections, Neutron news **3**, 26 (1992).

[40] M. Strobl, N. Kardjilov, A. Hilger, E. Jericha, G. Badurek, and I. Manke, Imaging with polarized neutrons, Physica B: Condensed Matter **404**, 2611 (2009).

[41] M. Strobl, C. Pappas, A. Hilger, S. Wellert, N. Kardjilov, S. Seidel, and I. Manke, Polarized neutron imaging: A spin-echo approach, Physica B: Condensed Matter **406**, 2415 (2011).

[42] P. Jorba, M. Schulz, D. S. Hussey, M. Abir, M. Seifert, V. Tsurkan, A. Loidl, C. Pfleiderer, and B. Khaykovich, High-resolution neutron depolarization microscopy of the ferromagnetic transitions in Ni3Al and HgCr2Se4 under pressure, Journal of magnetism and magnetic materials **475**, 176 (2019).

[43] M. Schulz, A. Neubauer, P. Böni, and C. Pfleiderer, Neutron depolarization imaging of the hydrostatic pressure dependence of inhomogeneous ferromagnets, Applied Physics Letters **108** (2016).

[44] N. Kardjilov, I. Manke, A. Hilger, M. Strobl, and J. Banhart, Neutron imaging in materials science, Materials Today **14**, 248 (2011).

[45] R. Woracek, D. Penumadu, N. Kardjilov, A. Hilger, M. Boin, J. Banhart, and I. Manke, Neutron Bragg edge tomography for phase mapping, Physics Procedia **69**, 227 (2015).

[46] R. Woracek, D. Penumadu, N. Kardjilov, A. Hilger, M. Strobl, R. Wimpory, I. Manke, and J. Banhart, Neutron Bragg-edge-imaging for strain mapping under in situ tensile loading, Journal of Applied Physics **109** (2011).

[47] R. Woracek, D. Penumadu, N. Kardjilov, A. Hilger, M. Boin, J. Banhart, and I. Manke, 3D Mapping of Crystallographic Phase Distribution using Energy-Selective Neutron Tomography, Advanced Materials **26**, 4069 (2014).

[48] C. Grünzweig, *Visualization of a fired two-stroke chain saw engine running at idle speed by dynamic neutron radiography*, Tech. Rep. (SAE Technical Paper, 2010).

[49] E. Dabah, B. Pfretzschner, T. Schaupp, N. Kardjilov, I. Manke, M. Boin, R. Woracek, and A. Griesche, Time-resolved Bragg-edge neutron radiography for observing martensitic phase transformation from austenitized super martensitic steel, Journal of Materials Science **52**, 3490 (2017).

[50] B. Schillinger, J. Brunner, and E. Calzada, A study of oil lubrication in a rotating engine using stroboscopic neutron imaging, Physica B: Condensed Matter **385**, 921 (2006).

[51] S. Scheler, S. Knappke, M. Schulz, and A. Zuern, Needle clogging of protein solutions in prefilled syringes: A two-stage process with various determinants, European Journal of Pharmaceutics and Biopharmaceutics **176**, 188 (2022).

[52] D. Mannes, E. Lehmann, A. Masalles, K. Schmidt-Ott, K. Schaeppi, F. Schmid, S. Peetermans, K. Hunger, *et al.*, The study of cultural heritage relevant objects by means of neutron imaging techniques, Insight-Non-Destructive Testing and Condition Monitoring **56**, 137 (2014).

[53] F. Salvemini and F. Grazzi, The glory of ancient weapons and armors: neutron imaging and diffraction methods in modern archaeology, Neutron Methods for Archaeology and Cultural Heritage , 67 (2017).

[54] K. Ryzewski, S. Herringer, H. Bilheux, L. Walker, B. Sheldon, S. Voisin, J.-C. Bilheux, and V. Finocchiaro, Neutron imaging of archaeological bronzes at the Oak Ridge national laboratory, Physics Procedia **43**, 343 (2013).

[55] R. F. Ziesche, T. Arlt, D. P. Finegan, T. M. Heenan, A. Tengattini, D. Baum, N. Kardjilov, H. Markötter, I. Manke, W. Kockelmann, *et al.*, 4D imaging of lithium-batteries using correlative neutron and X-ray tomography with a virtual unrolling technique, Nature communications **11**, 1 (2020).

[56] S. Robuschi, A. Tengattini, J. Dijkstra, I. Fernandez, and K. Lundgren, A closer look at corrosion of steel reinforcement bars in concrete using 3D neutron and X-ray computed tomography, Cement and Concrete Research **144**, 106439 (2021).

[57] D. S. Hussey, H. Wen, H. Wu, T. R. Gentile, W. Chen, D. L. Jacobson, J. M. LaManna, and B. Khaykovich, Demonstration of Focusing Wolter Mirrors for Neutron Phase and Magnetic Imaging, Journal of Imaging **4**, 50 (2018).

[58] P. Trtik, J. Hovind, C. Grünzweig, A. Bollhalder, V. Thominet, C. David, A. Kaestner, and E. H. Lehmann, Improving the spatial resolution of neutron imaging at paul scherrer institut–the neutron microscope project, Physics Procedia **69**, 169 (2015).

[59] D. S. Hussey, J. M. LaManna, E. Baltic, and D. L. Jacobson, Neutron imaging detector with 2 μm spatial resolution based on event reconstruction of neutron capture in gadolinium oxysulfide scintillators, Nuclear Instruments and Methods in Physics Research Section A: Accelerators, Spectrometers, Detectors and Associated Equipment **866**, 9 (2017).

[60] S. Williams, A. Hilger, N. Kardjilov, I. Manke, M. Strobl, P. Douissard, T. Martin, H. Riesemeier, and J. Banhart, Detection system for microimaging with neutrons, Journal of instrumentation **7**, P02014 (2012).

[61] J. Crha, J. Vila-Comamala, E. Lehmann, C. David, and P. Trtik, Light yield enhancement of 157-gadolinium oxysulfide scintillator screens for the high-resolution neutron imaging, MethodsX **6**, 107 (2019).

[62] F. Pfeiffer, C. Grünzweig, O. Bunk, G. Frei, E. Lehmann, and C. David, Neutron phase imaging and tomography, Physical review letters **96**, 215505 (2006).

[63] M. Strobl, C. Grünzweig, A. Hilger, I. Manke, N. Kardjilov, C. David, and F. Pfeiffer, Neutron dark-field tomography, Physical review letters **101**, 123902 (2008).

[64] C. Grünzweig, *Neutron grating interferometry for imaging magnetic structures in bulk ferromagnetic materials*, Ph.D. thesis, Diss., Naturwissenschaften, Eidgenössische Technische Hochschule ETH Zürich, Nr. 18612, 2009 (2009).

[65] T. Neuwirth, A. Backs, A. Gustschin, S. Vogt, F. Pfeiffer, P. Böni, and M. Schulz, A high visibility Talbot-Lau neutron grating interferometer to investigate stress-induced magnetic degradation in electrical steel, Scientific reports **10**, 1 (2020).

[66] R. P. Harti, M. Strobl, B. Betz, K. Jefimovs, M. Kagias, and C. Grünzweig, Sub-pixel correlation length neutron imaging: Spatially resolved scattering information of microstructures on a macroscopic scale, Scientific Reports **7**, 1 (2017).

[67] T. Reimann, S. Mühlbauer, M. Horisberger, B. Betz, P. Böni, and M. Schulz, The new neutron grating interferometer at the ANTARES beamline: design, principles and applications, Journal of Applied Crystallography **49**, 1488 (2016).

[68] D. A. Pushin, D. Sarenac, D. S. Hussey, H. Miao, M. Arif, D. G. Cory, M. G. Huber, D. L. Jacobson, J. M. LaManna, J. D. Parker, *et al.*, Far-field interference of a neutron white beam and the applications to noninvasive phase-contrast imaging, Physical Review A **95**, 043637 (2017).

[69] D. Sarenac, D. A. Pushin, M. G. Huber, D. S. Hussey, H. Miao, M. Arif, D. G. Cory, A. D. Cronin, B. Heacock, D. L. Jacobson, *et al.*, Three phase-grating moiré neutron interferometer for large interferometer area applications, Physical review letters **120**, 113201 (2018).

[70] S. Vogt, T. Neuwirth, B. Schauerte, H. A. Weiss, P. M. Falger, A. Gustschin, M. Schulz, K. Hameyer, and W. Volk, Extent of embossing-related residual stress on the magnetic properties evaluated using neutron grating interferometry and single sheet test, Production Engineering **13**, 211 (2019).

[71] J. Valsecchi, R. P. Harti, M. Raventós, M. D. Siegwart, M. Morgano, P. Boillat, M. Strobl, P. Hautle, L. Holitzner, U. Filges, *et al.*, Visualization and quantification of inhomogeneous and anisotropic magnetic fields by polarized neutron grating interferometry, Nature Communications **10**, 3788 (2019).

[72] T. Reimann, M. Schulz, D. F. Mildner, M. Bleuel, A. Brûlet, R. P. Harti, G. Benka, A. Bauer, P. Böni, and S. Mühlbauer, Domain formation in the type-II/1 superconductor niobium: Interplay of pinning, geometry, and attractive vortex-vortex interaction, Physical Review B **96**, 144506 (2017).

[73] T. Reimann, M. Schulz, C. Grünzweig, A. Kaestner, A. Bauer, P. Böni, and S. Mühlbauer, Neutron Dark-Field Imaging of the Domain Distribution in the Intermediate State of Lead, Journal of Low Temperature Physics **182**, 107 (2016).

[74] A. Backs, T. Reimann, M. Schulz, V. Pipich, S. Mühlbauer, and P. Böni, Domain formation in the type-II/1 superconductor niobium, Verhandlungen der Deutschen Physikalischen Gesellschaft (2018).

[75] A. Backs, M. Schulz, V. Pipich, M. Kleinhans, P. Böni, and S. Mühlbauer, Universal behavior of the intermediate mixed state domain formation in superconducting niobium, Physical Review B **100**, 064503 (2019).

[76] M. Strobl, General solution for quantitative dark-field contrast imaging with grating interferometers, Scientific reports **4**, 7243 (2014).

[77] B. Betz, R. Harti, M. Strobl, J. Hovind, A. Kaestner, E. Lehmann, H. Van Swygenhoven, and C. Grünzweig, Quantification of the sensitivity range in neutron dark-field imaging, Review of Scientific Instruments **86**, 123704 (2015).

[78] P. Rauscher, B. Betz, J. Hauptmann, A. Wetzig, E. Beyer, and C. Grünzweig, The influence of laser scribing on magnetic domain formation in grain oriented electrical steel visualized by directional neutron dark-field imaging, Scientific reports **6**, 1 (2016).

[79] M. Strobl, B. Betz, R. Harti, A. Hilger, N. Kardjilov, I. Manke, and C. Gruenzweig, Wavelength-dispersive dark-field contrast: micrometre structure resolution in neutron imaging with gratings, Journal of Applied Crystallography **49**, 569 (2016).

[80] T. Donath, M. Chabior, F. Pfeiffer, O. Bunk, E. Reznikova, J. Mohr, E. Hempel, S. Popescu, M. Hoheisel, M. Schuster, J. Baumann, and C. David, Inverse geometry for grating-based x-ray phase-contrast imaging, Journal of Applied Physics **106**, 054703 (2009).

[81] T. Neuwirth, P. Boeni, and M. Schulz, Origin of Pseudo-Variation in High Resolution Neutron Grating Interferometry, WCNR-11 **15**, 129 (2020).

[82] F. Pfeiffer, T. Weitkamp, O. Bunk, and C. David, Phase retrieval and differential phase-contrast imaging with low-brilliance X-ray sources, Nature physics **2**, 258 (2006).

[83] F. Pfeiffer, M. Bech, O. Bunk, P. Kraft, E. F. Eikenberry, C. Brönnimann, C. Grünzweig, and C. David, Hard-X-ray dark-field imaging using a grating interferometer, Nature materials **7**, 134 (2008).

[84] S. Marathe, L. Assoufid, X. Xiao, K. Ham, W. W. Johnson, and L. G. Butler, Improved algorithm for processing grating-based phase contrast interferometry image sets, Review of Scientific Instruments **85**, 013704 (2014).

[85] J. Dittmann, A. Balles, and S. Zabler, Optimization based evaluation of grating interferometric phase stepping series and analysis of mechanical setup instabilities, Journal of Imaging **4**, 77 (2018).

[86] J. t. Schelten and W. Schmatz, Multiple-scattering treatment for small-angle scattering problems, Journal of Applied Crystallography **13**, 385 (1980).

[87] E. Calzada, F. Gruenauer, M. Mühlbauer, B. Schillinger, and M. Schulz, New design for the ANTARES-II facility for neutron imaging at FRM II, Nuclear Instruments and Methods in Physics Research Section A: Accelerators, Spectrometers, Detectors and Associated Equipment **605**, 50 (2009).

[88] J. Šaroun, Evaluation of double-crystal SANS data influenced by multiple scattering, Journal of applied crystallography **33**, 824 (2000).

[89] R. Harti, M. Strobl, M. Morgano, J. Valsecchi, and C. Grünzweig, Statistical uncertainty in the dark-field and transmission signal of grating interferometry, Review of Scientific Instruments **88**, 103704 (2017).

[90] O. Instruments, Specifications Andor Neo 5.5 sCMOS, `https://andor.oxinst.com/assets/uploads/products/andor/documents/andor-neo-scmos-specifications.pdf` (), accessed: 20-December-2022.

[91] O. Instruments, Specifications Andor ikon-L 936 CCD, `https://andor.oxinst.com/assets/uploads/products/andor/documents/andor-ikon-l-936-specifications.pdf` (), accessed: 20-December-2022.

[92] Y. Yehuda-Zada, K. Pritchard, J. B. Ziegler, C. Cooksey, K. Siebein, M. Jackson, C. Hurlbut, Y. Kadmon, Y. Cohen, R. Ibberson, *et al.*, Optimization of 6LiF: ZnS (Ag) scintillator light yield using GEANT4, Nuclear Instruments and Methods in Physics Research Section A: Accelerators, Spectrometers, Detectors and Associated Equipment **892**, 59 (2018).

[93] F. M. Piegsa, A. Kaestner, A. Antognini, A. Eggenberger, K. Kirch, and G. Wichmann, Statistical uncertainty in quantitative neutron radiography, The European Physical Journal Applied Physics **78**, 10702 (2017).

[94] M. Schulz and B. Schillinger, ANTARES: Cold neutron radiography and tomography facility, Journal of large-scale research facilities JLSRF **1**, A17 (2015).

[95] A. Tremsin, V. Dangendorf, K. Tittelmeier, B. Schillinger, M. Schulz, M. Lerche, and W. Feller, Time-resolved neutron imaging at ANTARES cold neutron beamline, Journal of Instrumentation **10**, P07008 (2015).

[96] V. Revol, C. Kottler, R. Kaufmann, A. Neels, and A. Dommann, Orientation-selective X-ray dark field imaging of ordered systems, Journal of Applied Physics **112**, 114903 (2012).

[97] M. Chabior, *Contributions to the characterization of grating-based x-ray phase-contrast imaging*, Ph.D. thesis, Diss., Technische UniversitÃ¤t Dresden, 2011 (2011).

[98] A. Gustschin, T. Neuwirth, A. Backs, M. Schulz, and F. Pfeiffer, Fabrication of gadolinium particle-based absorption gratings for neutron grating interferometry, Review of Scientific Instruments **89**, 103702 (2018).

[99] A. Hipp, M. Willner, J. Herzen, S. Auweter, M. Chabior, J. Meiser, K. Achterhold, J. Mohr, and F. Pfeiffer, Energy-resolved visibility analysis of grating interferometers operated at polychromatic X-ray sources, Optics express **22**, 30394 (2014).

[100] R. P. Harti, C. Kottler, J. Valsecchi, K. Jefimovs, M. Kagias, M. Strobl, and C. Grünzweig, Visibility simulation of realistic grating interferometers including grating geometries and energy spectra, Optics Express **25**, 1019 (2017).

[101] M. Chabior, T. Donath, C. David, M. Schuster, C. Schroer, and F. Pfeiffer, Signal-to-noise ratio in x ray dark-field imaging using a grating interferometer, Journal of Applied Physics **110**, 053105 (2011).

[102] H. F. Talbot, LXXVI. Facts relating to optical science. No. IV, The London, Edinburgh, and Dublin Philosophical Magazine and Journal of Science **9**, 401 (1836).

[103] J.-P. Guigay, S. Zabler, P. Cloetens, C. David, R. Mokso, and M. Schlenker, The partial Talbot effect and its use in measuring the coherence of synchrotron X-rays, Journal of synchrotron radiation **11**, 476 (2004).

[104] M. Morgano, S. Peetermans, E. Lehmann, T. Panzner, and U. Filges, Neutron imaging options at the BOA beamline at Paul Scherrer Institut, Nuclear Instruments and Methods in Physics Research Section A: Accelerators, Spectrometers, Detectors and Associated Equipment **754**, 46 (2014).

[105] H. A. Weiss, P. Tröber, R. Golle, S. Steentjes, N. Leuning, S. Elfgen, K. Hameyer, and W. Volk, Impact of punching parameter variations on magnetic properties of nongrain-oriented electrical steel, IEEE Transactions on Industry Applications **54**, 5869 (2018).

[106] R. Siebert, A. Wetzig, E. Beyer, B. Betz, C. Grünzweig, and E. Lehmann, Localized investigation of magnetic bulk property deterioration of electrical steel: Analysing magnetic property drop thorough mechanical and laser cutting of

electrical steel laminations using neutron grating interferometry, in *2013 3rd International Electric Drives Production Conference (EDPC)* (IEEE, 2013) pp. 1–5.

[107] S. W. Lee, K.-Y. Kim, O. Y. Kwon, N. Kardjilov, M. Dawson, A. Hilger, and I. Manke, Observation of magnetic domains in insulation-coated electrical steels by neutron dark-field imaging, Applied physics express **3**, 106602 (2010).

[108] R. Siebert, J. Schneider, and E. Beyer, Laser cutting and mechanical cutting of electrical steels and its effect on the magnetic properties, IEEE Transactions on Magnetics **50**, 1 (2014).

[109] R. P. Harti, M. Strobl, R. Schäfer, N. Kardjilov, A. S. Tremsin, and C. Grünzweig, Dynamic volume magnetic domain wall imaging in grain oriented electrical steel at power frequencies with accumulative high-frame rate neutron dark-field imaging, Scientific reports **8**, 15754 (2018).

[110] B. Betz, P. Rauscher, R. Siebert, R. Schaefer, A. Kaestner, H. Van Swygenhoven, E. Lehmann, and C. Grünzweig, Visualization of bulk magnetic properties by neutron grating interferometry, Physics Procedia **69**, 399 (2015).

[111] I. Gilch, T. Neuwirth, B. Schauerte, N. Leuning, S. Sebold, K. Hameyer, M. Schulz, and W. Volk, Impact of residual stress evoked by pyramidal embossing on the magnetic material properties of non-oriented electrical steel, Archive of Applied Mechanics **91**, 3513 (2021).

[112] I. Gilch, S. Vogt, T. Neuwirth, B. Schauerte, K. Hameyer, M. Schulz, A. Gustschin, W. Volk, and H. A. Weiss, Analysis of cylindrically and spherically embossed flux barriers in non-oriented electrical steel, in *Forming the Future: Proceedings of the 13th International Conference on the Technology of Plasticity* (Springer, 2021) pp. 2303–2318.

[113] B. Schauerte, N. Leuning, S. Vogt, I. Moll, H. Weiss, T. Neuwirth, M. Schulz, W. Volk, and K. Hameyer, The influence of residual stress on flux-barriers of non-oriented electrical steel, Journal of Magnetism and Magnetic Materials **504**, 166659 (2020).

[114] B. Schauerte, I. Gilch, T. Neuwirth, S. Sebold, N. Leuning, M. Schulz, W. Volk, and K. Hameyer, Alternative Magnetflussführung in Elektromotoren, Forschung im Ingenieurwesen **85**, 827 (2021).

[115] C. C. Lo, E. Kinser, and D. C. Jiles, Modeling the interrelating effects of plastic deformation and stress on magnetic properties of materials, Journal of Applied Physics **93**, 6626 (2003).

[116] V. Goel, P. Anderson, J. Hall, F. Robinson, and S. Bohm, Electroless Co–P-Carbon Nanotube composite coating to enhance magnetic properties of grain-oriented electrical steel, Journal of Magnetism and Magnetic Materials **407**, 42 (2016).

[117] O. Perevertov, J. Thielsch, and R. Schäfer, Effect of applied tensile stress on the hysteresis curve and magnetic domain structure of grain-oriented transverse Fe-3% Si steel, Journal of Magnetism and Magnetic Materials **385**, 358 (2015).

[118] B. Betz, P. Rauscher, R. Harti, R. Schäfer, H. Van Swygenhoven, A. Kaestner, J. Hovind, E. Lehmann, and C. Grünzweig, In-situ visualization of stressdependent bulk magnetic domain formation by neutron grating interferometry, Applied Physics Letters **108** (2016).

[119] C. Grünzweig, C. David, O. Bunk, M. Dierolf, G. Frei, G. Kühne, R. Schäfer, S. Pofahl, H. Rønnow, and F. Pfeiffer, Bulk magnetic domain structures visualized by neutron dark-field imaging, Applied Physics Letters **93**, 112504 (2008).

[120] I. Manke, N. Kardjilov, R. Schäfer, A. Hilger, M. Strobl, M. Dawson, C. Grünzweig, G. Behr, M. Hentschel, C. David, *et al.*, Three-dimensional imaging of magnetic domains, Nature communications **1**, 125 (2010).

[121] N. Kardjilov, I. Manke, R. Woracek, A. Hilger, and J. Banhart, Advances in neutron imaging, Materials Today **21**, 652 (2018).

[122] I. Dhiman, R. Ziesche, L. Riik, I. Manke, A. Hilger, B. Radhakrishnan, T. Burress, W. Treimer, and N. Kardjilov, Visualization of magnetic domain structure in FeSi based high permeability steel plates by neutron imaging, Materials Letters **259**, 126816 (2020).

[123] V. Wagner and D. Bellmann, Bulk domain sizes determined by complementary scattering methods in polycrystalline Fe, Physica B: Condensed Matter **397**, 27 (2007).

[124] S. Blundell, *Magnetism in Condensed Matter* (OUP Oxford, 2001).

[125] P. Vourna, A. Ktena, and E. Hristoforou, Residual stress analysis in nonoriented electrical steel sheets by Barkhausen noise measurements, IEEE transactions on magnetics **50**, 1 (2014).

[126] T. H. Jensen, M. Bech, I. Zanette, T. Weitkamp, C. David, H. Deyhle, S. Rutishauser, E. Reznikova, J. Mohr, R. Feidenhans, *et al.*, Directional x-ray dark-field imaging of strongly ordered systems, Physical Review B **82**, 214103 (2010).

[127] E. du Trémolet de Lacheisserie, D. Gignoux, and M. Schlenker, *Magnetism: II-Materials and Applications* (Springer US, 2012).

[128] D. Miyagi, K. Miki, M. Nakano, and N. Takahashi, Influence of compressive stress on magnetic properties of laminated electrical steel sheets, IEEE Transactions on Magnetics **46**, 318 (2010).

[129] K. Lorenz, E. Calzada, M. Mühlbauer, B. Schillinger, M. Schulz, and K. Zeitlhack, The new multi-filter at ANTARES: TOF measurements and first applications, in *Proceedings of the Eighth World Conference on Neutron Radiography, Gaithersburg, MD, USA* (2006).

[130] A. Pichlmaier, Z. Revay, A. Röhrmoser, B. Schillinger, M. Schulz, C. Stieghorst, T. Neuwirth, F. Jeschke, A. Backs, A. Wirtz, *et al.*, CARBON-14, COLD SOURCE, CYCLE OF FUEL AND THE CORONA PANDEMIC-FRM II OPERATOR'S CHALLENGES IN THE YEARS 2020/21, in *The European Research Reactor Conference*, IMPULSE-2021-00351 (PGAA, 2021).